Aus der Klinik für Diagnostische und Interventionelle Radiologie der Universität Heidelberg

Ärztlicher Direktor: Prof. Dr. med. Hans-Ulrich Kauczor

Quantification of perfusion abnormalities using dynamic contrast-enhanced magnetic resonance imaging in muco-obstructive lung diseases

Inauguraldissertation

zur Erlangung des Doctor scientiarum humanarum (Dr. sc. hum.)

an der

Medizinischen Fakultät Heidelberg

der

Ruprecht-Karls-Universität

vorgelegt von

MARILISA KONIETZKE

(geborene Schiwek)

aus

Ulm

2022

Dekan: Prof. Dr. med. Hans-Georg Kräusslich

Doktorvater: Prof. Dr. med. Hans-Ulrich Kauczor

TABLE OF CONTENTS

ABBREVIATIONS

3D	Three Dimensions or Three-Dimensional
a.u.	Arbitrary Units
AIF	Arterial Input Function
BMI	Body Mass Index
C(t)	Concentration Time Course in the Lung Parenchyma
C(t) map	Concentration Time Course Map
$C(t)^{noisy}$	Noisy Concentration Time Course
CA	Contrast Agent
$C_a(t)$	Concentration Time Course at the Arterial Input
CF	Cystic Fibrosis
CFTR	Cystic Fibrosis Transmembrane Conductance Regulator
CNR	Contrast-to-Noise Ratio
COPD	Chronic Obstructive Pulmonary Disease
Cor	Coronal Plane/Orientation
CT	Computed Tomography
DCE-MRI	Dynamic Contrast-Enhanced Magnetic Resonance Imaging
DTPA	Diethylenetriaminepentaacetic Acid
ENaC	Epithelial Sodium Channel
FD	Fourier Decomposition
FEV1%predicted	Forced Expiratory Volume in 1 Second Percent Predicted
FEV1/FVC	Ratio Between Forced Expiratory Volume in 1 Second and Forced Vital Capacity
FLASH	Fast Low Angle Shot

FoV	Field of View
fSAD	Functional Small Airway Disease
Gd	Gadolinium
Gd-BT-DO3A	Gadobutrol
GRE	Gradient-Echo
HPV	Hypoxic Pulmonary Vasoconstriction
IRF	Impulse Response Function
IRF map	Impulse Response Function Map
IRF^{noisy}	Noisy Impulse Response Function
IRF$_{max}$ map	Impulse Response Function Map at the Time Point of Maximum Contrast Enhancement
LCC	L-Curve Criterion
LoA	Limits of Agreement
MID	Minimal Important Difference
MIP	Maximum Intensity Projection
MRI	Magnetic Resonance Imaging
MTT	Mean Transit Time
NCC	Normalised Cross-Correlation
PBF	Pulmonary Blood Flow
PBF^{noisy}	Noisy Pulmonary Blood Flow
PBV	Pulmonary Blood Volume
PFT	Pulmonary Function Testing
PRM	Parametric Response Mapping
QDP	Perfusion Defects in Percent
R(t)	Residue Function

R1(=1/T1)	Longitudinal Relaxation Rate
rANOVA	Repeated Measures Analysis of Variance
rBV	Regional Pulmonary Blood Volume
RF	Radiofrequency or High-Frequency
ROI	Region of Interest
S(t)	Signal Intensity Time Course
S_0	Baseline Signal
SD	Standard Deviation
SFTR	Standard Form Tikhonov Regularisation
SNR	Signal-to-Noise Ratio
$S_{rel}(t)$	Relative Signal Change Time Course
ST	Slice Thickness
SVD	Singular Value Decomposition
T1	Longitudinal Relaxation Time or Spin-Lattice Relaxation
T2*	Transverse Relaxation Time or Spin-Spin Relaxation
TE	Echo Time
TR	Repetition Time
Tra	Transverse Plane/Orientation
tSVD	Truncated Singular Value Decomposition
TWIST	Time-Resolved Angiography with Interleaved Stochastic Trajectories
V/Q mismatch	Ventilation/Perfusion Mismatch
V/Q ratio	Ventilation/Perfusion Ratio
VIBE	Volume-Interpolated Breath-Hold Examination
Voxel	Volume Element

1   INTRODUCTION

Cystic fibrosis (CF) and **chronic obstructive pulmonary disease (COPD)** are muco-obstructive lung diseases with pathological alterations of the respiratory tract, resulting in cough, sputum production, and shortness of breath for the patient (Boucher 2019). These symptoms are caused by airflow limitations, inflammation, and infections, which is especially critical in the small airways where the mucus cannot be cleared by cough. Furthermore, in patients with lung emphysema the tissue degradation leads to lung vessel remodelling and obliteration (Voelkel et al. 2011). Occurring pathological alterations are often heterogeneously distributed across the lungs in CF and COPD, which means that some parts of the lungs can be severely affected while other parts of the lungs show little or no alterations. Although both diseases have different aetiologies and progression, they constitute a high burden for the patient and can lead to death.

CF is a lethal genetic disease caused by a mutation of the gene that encodes the cystic fibrosis transmembrane conductance regulator (CFTR) protein with an autosomal recessive inheritance (Riordan et al. 1989). Several hypotheses about the consequences of CFTR dysfunction exist, which all point to mucus hyper-concentration and decreased mucociliary clearance (O'Sullivan and Freedman 2009). The resulting muco-obstructive alterations of the lungs are the main course of morbidity and mortality in CF, but other organs are also affected by the disease. CF is classified as a rare disease, with a predicted life expectancy of only 46 years for patients born between 2015 and 2019, without CFTR modulator therapies included in the prediction (Cystic Fibrosis Foundation 2019).

COPD is the third leading cause of death worldwide and a prevalent chronic disease of middle and older age (Lozano et al. 2013). COPD is usually caused by considerable exposure to

noxious particles or gases, like tobacco smoke or air pollution, leading to inflammation with increased mucus production, decreased mucociliary clearance and tissue degradation in the lungs. Airflow limitation can often severely limit the patient's quality of life, but mortality in COPD patients is also driven by concomitant chronic diseases, such as cardiovascular comorbidities.

Pulmonary Function Testing (PFT) is the most frequently used procedure in pulmonology, evaluating several parameters of lung volume and airflow velocity to assess a patient´s lung function. Spirometry and full body plethysmography are the most important and the most common types of PFT and available at most hospitals. PFT is required for the diagnosis of COPD assessing the degree of airflow limitations (Vogelmeier et al. 2017). Furthermore, in CF and COPD, PFT is used as a non-invasive assessment for therapeutic decisions, prognosis, and disease monitoring. In clinical studies aiming to investigate new medicinal products for the treatment of CF or COPD, PFT is used for patient selection/characterisation and as an efficacy endpoint (CHMP 2012a; CMPH 2009). Although PFT is an important procedure in pulmonology, it has major limitations (CHMP 2012b). For example, PFT provides only global values for the entire lung, and some of the PFT parameters take large/medium airways more into account than small airways, rendering it difficult to assess the heterogeneously distributed pathological alterations of muco-obstructive lung diseases.

In contrast, **medical imaging**, enables the regional assessment of structural and functional abnormalities. Morphological imaging can provide information about pathological changes in the lung tissue structure, e.g. bronchiectasis or lung density changes. Functional imaging of the lungs can help to examine pathological abnormalities in the ventilation and perfusion of the lungs, which can be regionally altered in CF and COPD up to complete regional deterioration.

Functional imaging is complementary to morphological imaging and offers the opportunity to evaluate the physiology of an organ or the pathophysiology of a disease in more detail. Furthermore, it is hypothesised that functional lung imaging can detect pathologies earlier in the disease course than morphological imaging (Alford et al. 2010).

Functional imaging of pulmonary ventilation and perfusion can be performed using different imaging modalities, including computed tomography (CT), magnetic resonance imaging (MRI), and scintigraphy. However, CT and scintigraphy examinations expose patients to ionising radiation, which limits the use of both procedures for monitoring purposes, especially in children with CF. In contrast, MRI does not require ionising radiation and can therefore be widely used in a clinical context. However, MRI in the lungs has several challenges and limitations, which are described in section 1.3.6. The potential of MRI in the lungs lies primarily in functional imaging.

The assessment of pulmonary perfusion using MRI is possible with and without contrast agent (CA) application. **Dynamic contrast-enhanced MRI (DCE-MRI)** is the most common method for functional lung MRI. In DCE-MRI, a gadolinium-based CA is injected intravenously as bolus, and time-resolved MRI is used to track the first passage of the CA through the lungs to derive information about the regional haemodynamics of the lungs (Fink et al. 2005c). This process is called bolus tracking.

Morphological and functional abnormalities on image data can be assessed visually by a radiologist, automatically by computer algorithms, or by a combination of both with different degrees of refinement. The following classifications are often used in medical imaging: **qualitative** (present or not present), **semi-quantitative** (in the form of categories, e.g. category

1 = less than 50% of the lungs affected and category 2 = more than 50% of the lungs affected), and **quantitative** (in the form of continuous values, e.g. the exact percentage of the extent of an abnormality).

In previous clinical studies, a semi-quantitative, morpho-functional MRI scoring system, including a sub-score for assessing pulmonary perfusion abnormalities (= **MRI perfusion score**) was established. This visual score has already been validated by comparisons with CT, multiple breath washout, and PFT parameters. Furthermore, its reproducibility was examined, and the score was successfully used as a response-to-treatment parameter in CF (Eichinger et al. 2012; Michael Puderbach et al. 2007; Sileo et al. 2014; Stahl et al. 2017; Wielpütz et al. 2014; Wielpütz et al. 2018).

Especially quantitative assessments are often computerised. **Computer-aided quantitative assessments of pulmonary perfusion** limit human interaction, are time efficient, and potentially produce more objective results compared to visual score, e.g. no inter- and intra-reader variabilities. In clinical studies, pulmonary blood flow (PBF) and pulmonary blood volume (PBV) based on the indicator dilution theory were used to assess pulmonary perfusion from DCE-MRI data (Hatabu et al. 1999b; Hueper et al. 2015; Ohno et al. 2004). The clinical meaningfulness of PBF and PBV was evaluated in previous studies against CT parameters, PFT parameters, and therapy response (Hueper et al. 2015; B. J. Jobst et al. 2015; Kaireit et al. 2019; Ley-Zaporozhan et al. 2007; Vogel-Claussen et al. 2019). However, one problem with quantifying PBF and PBV from DCE-MRI data is the high variability of the parameters. DCE-MRI data of the lungs are adversely affected by low contrast-to-noise ratio (CNR), non-linearity of the CA-signal relationship and pronounced MR imaging artefacts, which impair the reproducibility and robustness of PBF and PBV (Ley-Zaporozhan et al. 2011; Neeb et al.

2009; Puderbach et al. 2008; Ter-Karapetyan et al. 2018). Quantifying the extent of abnormalities, using unsupervised clustering algorithms would introduce an intrinsic normalisation and could help to reduce the variability of pulmonary perfusion quantification from DCE-MRI data. In previous studies, the extent of ventilation and/or perfusion defects appeared to be sensitive markers for disease severity based on the observed correlations with PFT parameters, multiple breath washout parameters, and morphological changes (Capaldi et al. 2018; Couch et al. 2019; Kaireit et al. 2019; Mathew et al. 2011; Woodhouse et al. 2005).

Especially quantitative parameters can be used as **biomarkers**, with various objectives and questions being possible. The term biomarker is used in medicine for a characteristic that can be used as an indicator for normal biological processes, pathogenic processes, or biological responses to an intervention, including therapeutic interventions. Biomarkers can be classified into the following categories, depending on their application/properties:

- Susceptibility/risk biomarker: A biomarker to identify patients with the potential for developing a disease.

- Diagnostic biomarker: A biomarker to detect or confirm the presence of a disease.

- Monitoring biomarker: A biomarker measured repeatedly to assess disease status.

- Prognostic biomarker: A biomarker to identify patients with a likelihood of a clinical event, disease recurrence or disease progression.

- Predictive biomarker: A biomarker to identify patients with the potential to experience a favourable or unfavourable effect to a medical product.

- Pharmacodynamic/response biomarker: A biomarker to show that a biological response has occurred to a medical product.

- Safety biomarker: A biomarker to measure adverse events to a medical product.

(BEST (Biomarkers, EndpointS, and other Tools) Resource - NCBI Bookshelf 2016).

In addition, biomarkers can be categorised based on their data source. For example, imaging biomarkers are measured using medical imaging data or molecular biomarkers are measured using biological samples, e.g. plasma, serum, cerebrospinal fluid, biopsy. Consequently, the pulmonary perfusion parameters measured using DCE-MRI data in this work are imaging-based biomarkers.

Sufficient **method validation** is particularly important for computerised assessments, to verify that the biomarker is suitable for its intended use. Validation of an imaging biomarker includes technical validation (e.g. precision and accuracy) and clinical validation (e.g. relationship with disease status/clinical endpoint) (Alberich-Bayarri et al. 2020). An important point of technical validation of an imaging biomarker is the determination of its precision, including the assessment of its reproducibility. Clinical validation focuses on evaluating the potential of the imaging biomarker for diagnosis, monitoring disease progression, or determining response to treatment (Alberich-Bayarri et al. 2020). Therefore, clinical validation of an imaging biomarker in muco-obstructive lung diseases should include comparisons with clinical parameters such as PFT.

The aim of this work was to develop, implement, evaluate, and validate novel imaging biomarkers for the computer-aided quantitative analysis of pulmonary perfusion using DCE-MRI data. Pulmonary perfusion parameters were evaluated to improve the understanding of the pathophysiology of muco-obstructive lung diseases and for potential use as biomarkers in clinical studies investigating new treatments for CF and COPD. The following sections of the introduction describe the relevant clinical background and the technical basics of the MRI

sequences used, including their known limitations. The section concludes with the objectives of this work.

1.1 Respiratory system

A network of organs and structures used for breathing, air conduction, and gas exchange forms the respiratory system. The main components are the lungs with their surrounding pleura, the vascular system, the airway system, the diaphragm, and the respiratory muscles. In the lung parenchyma, which is ventilated with air by the airway system and perfused with blood via the vascular system, the gas exchange of oxygen and carbon dioxide between air and blood occurs.

The lung is divided into a left and a right lung, occupying most of the intrathoracic space. The mediastinum, a connective tissue space containing the heart, major blood vessels, the trachea with the stem bronchi, the oesophagus, and the thymus gland, fills the space between both lungs. The left and right lungs are subdivided into lobes by fissures, which are double folds of the pleura. In human anatomy, the right lung is classically divided into an upper, middle, and lower lobe, while the left lung has only one upper and one lower lobe (Figure 1A). In medical imaging, the lingula of the left lung is sometimes considered the equivalent of the right middle lobe, enabling better side-to-side comparability.

The airway system is differentiated into upper and lower airways. The upper airways consist of the nasal cavity, the pharynx, and the larynx, whit the main functions of transporting and conditioning the breathing air. The lower airways begin with the trachea, which splits up into the right and left stem bronchi, which enter the lungs at the pulmonary hilum. The human airways have a dichotomous branching pattern where each branch adds another generation to the airway tree, commonly resulting in about 23 airway generations (1st = trachea,

2nd-4th = bronchi, 5th-15th = bronchioles, 16th = terminal bronchioles, 17th-19th = respiratory bronchioles, 20th-22nd = alveolar ductuli and 23rd = alveolar sacs) (Figure 1 A, B, C). The lower airways can be divided into the conducting and the respiratory zone, with the transition zone being the terminal bronchioles. The conducting zone of the lower airways has the same functions as the upper airways, while the respiratory zone is involved in the gas exchange. In scientific and medical practice, airways with a diameter smaller than 2mm are defined as **small airways,** usually corresponding to airways below the 8th generation (Weibel and Gomez 1962). Small airways are considered to play a special role in the development and progression of various chronic lung diseases (Hogg et al. 2004; McDonough et al. 2011; Tiddens et al. 2010).
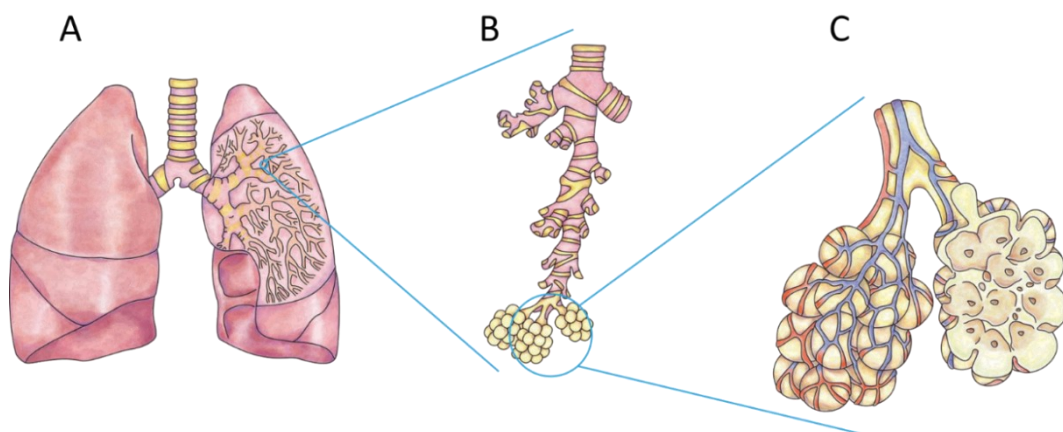
Figure 1: Illustration of the human lung with A) the trachea and the airway tree of the left lung visible. The lung lobes are separated by fissures, which are illustrated by dark blue lines. B) Terminal bronchioles, alveolar ducts and sacs of the airway tree. C) The primary lobules showing alveolar ducts and sacs covered by the pulmonary capillary network (blue: pulmonary arteries = oxygen-poor blood; red: pulmonary veins = oxygen-rich blood) [https://upload.wikimedia.org/wikipedia/commons/5/58/202008_lung_detailed.svg; DataBase Center for Life Science (DBCLS), CC BY 4.0 <https://creativecommons.org/licenses/by/4.0>, via Wikimedia Commons].

The vascular system allows for systemic and pulmonary circulation. The pulmonary circulation transports deoxygenated blood from the right atrium/ventricle of the heart through the pulmonary arteries to the pulmonary capillary bed, where gas exchange takes place. From there, the oxygenated blood is transported through the pulmonary veins into the left

atrium/ventricle, where the systemic circulation begins. The stroke volume, heart rate, and thus cardiac output (stroke volume heart rate) of the right and left heart are equal.

Gas exchange occurs in the lung parenchyma. The lung parenchyma comprises a network of small vessels surrounding the alveoli, forming the pulmonary capillary bed and the so-called respiratory surface area, which consists of about 300 million alveoli with a surface of approximately 100 to 140 square meters (Figure 1). The exchange of carbon dioxide and oxygen between the alveolar air and the capillaries takes place through a thin membrane, the blood-gas-barrier, which influences the gas exchange by its surface area and thickness. Gas exchange is controlled by partial gas pressure gradients between the capillary and alveolar compartments. The net diffusion of oxygen into the capillary blood is positive because the oxygen gas pressure in pulmonary arterial blood is much lower than in the alveoli. Conversely, the carbon dioxide pressure in the pulmonary arterial blood is much higher, leading to the elimination of carbon dioxide from the capillary blood. The gas pressures are homeostatically controlled, and changes in gas pressures affect the breathing sequence.

Gas exchange in the lungs is optimised by matching ventilation and perfusion, which can be assessed using **the ventilation/perfusion ratio (V/Q ratio)**. The V/Q ratio is defined as the ratio of air to blood volume reaching the alveoli per minute, with an ideal ratio of 1.0. The actual V/Q ratio for the whole lung is approximately 0.8 due to different oxygenation levels and volumes of air and blood entering the lungs per minute. The V/Q ratio is also not homogenous throughout the lungs and is altered by gravity and body position. The pathological inequality of ventilation and perfusion is described by the ventilation/perfusion mismatch (V/Q mismatch).

1.2   Clinical background

1.2.1   Muco-obstructive lung diseases

Muco-obstructive lung diseases comprises a spectrum of diseases whose clinical presentation includes cough, sputum production, and episodic exacerbations. Pathological features of muco-obstructive diseases include diffuse mucus obstruction, airway-wall ectasia, chronic inflammation, and bacterial infections. CF and COPD can be both classified as **muco-obstructive lung diseases** since both diseases are associated with the typical muco-obstructive features (Boucher 2019).

CF is a rare autosomal recessive disease, affecting the respiratory tract, the digestive system, sweat glands, and the reproductive tract. CF is caused by mutations in the *CFTR* protein-encoding gene, which is expressed in epithelial and blood cells. The CFTR protein works as an anion channel that facilitates the passage of chloride and bicarbonate through the cell membrane to the airway lumen in the respiratory tract. Mutations in the CFTR gene in humans result in the absence or impaired function of the channel, leading to reduced and highly viscous airway surface fluid that impairs mucociliary clearance and results in excessive mucus production. Consequences include mucus plugging, airway wall thickening, progressive dysfunctional airway dilatation (bronchiectasis) and emphysematous tissue destruction (Mets et al. 2015; Wielpütz et al. 2013). Patients with CF suffer from sterile inflammation, but also from recurrent and chronically persisting pulmonary infections, which cause clinical symptoms such as chronic productive cough and shortness of breath. Currently, several *CFTR* mutation classes are known, creating a heterogeneous disease pattern with differences in disease severity and progression. The primary cause of death in CF is respiratory disease (Cystic Fibrosis Foundation Patient Registry 2019). The first signs of the disease may appear in the first weeks

of life with detectable abnormalities of lung ventilation and perfusion, but also air-trapping in later stages (Hoo et al. 2012; Mall 2016; Stahl et al. 2014; Wielpütz et al. 2014).

COPD is triggered by an immune response of the lungs when inhaling toxic particles and gases, such as tobacco smoke or polluted air. The immune response causes chronic inflammation in the smaller airways, leading to remodelling/narrowing and mucus production, which in turn can cause hyperinflation. These pathological changes in small airways are often summarised as functional small airway disease (fSAD). fSAD is thought to occur prior to the emphysematous destruction of the lung parenchyma leading to severe air trapping due to loss of elastic recoil pressure (Aarli et al. 2015; Hogg et al. 1968; Hogg et al. 2004; Thomas et al. 2013). Therefore, fSAD might serve as potentially reversible precursor lesion to irreversible emphysema (Galbán et al. 2012; McDonough et al. 2011). Airflow limitations and recurrent pulmonary infections characterise the clinical presentation of COPD, while fSAD is considered the main reason for airflow limitations (Brabandt et al. 1983; Hogg et al. 1968; Macklem and Mead 1967). A frequent clinical feature in advanced COPD is pulmonary hypertension, which is caused by pulmonary arterial remodelling, with a high predominance in smaller arteries (Wrobel et al. 2013). The resulting high blood pressure in pulmonary arteries is the main cause of right ventricular failure (cor pulmonale). Different COPD phenotypes were defined by using PFT and/or radiologic assessments, as COPD is a heterogeneous disease that differs in severity and progression (Han et al. 2010; Subramanian et al. 2016). It is known that smoking can impair CFTR protein activity, which represents pathophysiological commonalities between CF and COPD (Dransfield et al. 2013; Knowles et al. 1981).

1.2.2　　Pulmonary perfusion abnormalities

Pulmonary perfusion abnormalities, such as delay, reduction or complete omission, manifest in muco-obstructive lung diseases in response to airflow limitation, inflammation, or emphysematous destruction of the lung parenchyma.

Airflow limitation results in regional alveolar hypoxia, triggering the mechanism of the hypoxic pulmonary vasoconstriction (HPV), also known as the Euler-Liljestrand mechanism (Euler and Liljestrand 1946). The HPV leads to a constriction of intrapulmonary arteries, diverting blood from poorly to better-ventilated lung areas. Altered pulmonary perfusion due to HPV is not only observed in the context of disease, but also in physiological processes required to optimise gas exchange during a change in body position or under physical stress. The HPV matches perfusion and ventilation, increasing the gas exchange efficiency and, by this, the V/Q ratio of the lungs. In the presence of **inflammation**, the alveoli are often flooded with debris, leading to regional hypoxia. Thus, the lung's normal response to HPV should be reduced regional perfusion. However, using imaging it could be demonstrated that the HPV can be blocked regionally in the presence of inflammation (Barbera et al. 1990; Gust et al. 1998; Hoffman et al. 2006). It has been hypothesised that if the inherent mechanisms fail to block HPV in the presence of inflammation, the inflammatory response may not be self-limiting through the normal cascade of events and repair mechanisms. This would in turn lead to chronic inflammation and emphysema (Alford et al. 2010; Hoffman et al. 2006; Ishizawa et al. 2004; Peinado et al. 2006). The **emphysematous destruction** in combination with remodelling of the pulmonary microvascular structures increase pulmonary arterial pressure and the vascular resistance in patients with chronic lung diseases (Hogg and Timens 2009).

Pulmonary perfusion abnormalities have the potential to play an increasingly important role in routine clinical monitoring of the health status of patients with muco-obstructive lung diseases. Furthermore, pulmonary perfusion abnormalities may fulfil the prerequisites to be used as **prognostic or response-to-treatment biomarker**. In this context, it was hypothesised, that perfusion abnormalities can be detected earlier by functional imaging than structural changes by morphological imaging, such as CT, as it is assumed that the spatial resolution of CT does not allow the detection of early structural abnormalities (Alford et al. 2010). Changes in pulmonary perfusion may also serve as response-to-treatment biomarker, since pulmonary perfusion abnormalities are a partially reversible component of muco-obstructive lung diseases, especially in lung regions where tissue degradation has not yet manifested (Hueper et al. 2015; Vogel-Claussen et al. 2019; Wielpütz et al. 2014).

1.3 Basics of MRI

The following sections introduce the basics of the MRI sequences used in this work, with a special focus on DCE-MRI. A comprehensive description of the basics and theory of MRI can be found elsewhere (Brown et al. 2014; Reiser and Semmler 1992; Vlaardingerbroek and Boer 2013). In the following, only **classical** MRI physics is descried without details of quantum mechanics.

1.3.1 Nuclear spin and nuclear magnetisation

The nuclear magnetic moment $\vec{\mu}$ is the basis of MRI. All atomic nuclei with an odd number of protons or neutrons have a net nuclear spin. The nuclear magnetic moment $\vec{\mu}$ is produced by the nuclear spin $\vec{I}$, which is a basic property of elementary particles and thus cannot be changed. The gyromagnetic ratio γ is a characteristic constant of the atomic nucleus and describes the

proportionality factor between the nuclear spin of a particle and the associated magnetic moment.

In this work, only **proton MRI** is considered, in which the magnetic properties of hydrogen atom nuclei (protons) are exploited. Hydrogen nuclei consist of only one proton and have the largest gyromagnetic ratio γ. In the following, the term "proton density" only includes the fraction of tissue protons that contribute to the MRI signal within a volume, i.e., the water and methylene protons of the mobile fatty acids. Protons incorporated into cell membranes, proteins or other relatively immobile macromolecular structures do not normally contribute to the signal. Proton MRI is particularly suitable for medical imaging because the human body consists of approximately 60% water. In principle, MRI is possible with all atomic nuclei with a net magnetic moment, but different technical components are required for image acquisition, e.g. adapted radiofrequency coils. For example, pulmonary fluorine-19-, hyperpolarised helium- or hyperpolarised xenon- gas can be used for functional lung MRI (Capaldi et al. 2018; Kaireit et al. 2018; Mathew et al. 2011; Schreiber et al. 2001).

In a **static homogeneous magnetic field,** the protons receive the additional potential energy E. The Zeeman effect describes the maximum energy difference ΔE that protons can have in this field

$$\Delta E = \hbar \cdot \gamma \cdot B_0 = \hbar \cdot \omega_L \qquad\qquad 1$$

where $\hbar$ is Planck's constant and B_0 the field strength of the external static magnetic field.

For protons, the maximum energy difference produced by the static magnetic field corresponds to the difference between parallel and anti-parallel alignment. The quantity of magnetic

moments in thermal equilibrium taking a certain orientation is governed by Boltzmann statistics. Due to the large number of spins, forming a spin ensemble, and since more protons align parallel (energetically favourable state) than anti-parallel (energetically less favourable state), a measurable magnetisation forms in the direction of the static magnetic field B_0. The measurable macroscopic nuclear magnetisation is described by the magnetisation $\vec{M}$. It is defined as the vector sum of the nuclear magnetic moments in the sample related to the volume V of the sample. However, the energy difference between these two orientations is very small for protons. In a magnetic field with a magnetic flux density of 1 Tesla (T) and at body temperature, the difference in relation to the total number of spins is only about 0.000007. To create such a strong magnetic field, which also needs to be as homogeneous as possible, the MRI scanner is equipped with a superconducting solenoid. This static homogeneous magnetic field is called B_0 and the direction of B_0 is by convention labelled as z with a x,y-plane perpendicular to it, according to a cartesian coordinate system.

1.3.2   Resonance excitation

Due to the nuclear spin, the magnetic moment $\vec{\mu}$, and thus also the macroscopic magnetisation $\vec{M}$ precesses around the direction of the B_0 field with the **Larmor frequency** ω_L. The Larmor frequency ω_L is proportional to the strength of the B_0 magnetic field Eq. 1. Using MRI, only the portion of the magnetisation $\vec{M}$, which is rotated into the x,y-plane (or flipped in other words), can be measured. The part of magnetisation $\vec{M}$ parallel to the axis of the static B_0 field is called longitudinal magnetisation M_z and the part of the magnetisation in the x,y-plane transverse magnetisation M_{xy}.

In the equilibrium state, the magnetisation $\vec{M}$ is predominantly aligned in the z-direction (M_{xy} = 0, M_z = M_0). The flipping of the magnetisation $\vec{M}$ away from the direction of the B_0 magnetic field is performed through high-frequency/radio-frequency (RF) pulses of a rotating magnetic high-frequency field B_1, whose frequency corresponds to the Larmor frequency. This process is called **resonance excitation**, because only if the high-frequency magnetic field B_1 has the same frequency as the spins (Larmor frequency), the spins can be excited in the energetically less favourable state (anti-parallel to B_0), i.e. only nuclei, which fulfil the resonance condition are excited. The high-frequency B_1 field is perpendicular to the B_0 field, and the RF pulses used for the excitation of spins are emitted by transmitting coils. The RF pulse leads to a phase synchronisation (phase coherence) of the magnetic moments $\vec{\mu}$, forming a macroscopic transverse magnetisation M_{xy}. The magnetisation in the x,y-plane M_{xy} still precesses around the B_0-direction, which thus appears as a rotating magnetic field. The rotating magnetic field induces voltage in resonant coils, which enables the measurement in the first place. For this purpose, receiving coils are used in MRI that are placed near the parts of the body to be examined. How far the magnetisation $\vec{M}$ is flipped by the excitation is indicated by the flip angle α. The flip angle describes the excitation time and the strength of the high-frequency field B_1.

1.3.3   Relaxation

By applying RF pulses of the high-frequency field B_1, the nuclear spin ensemble absorbs energy, followed by **a relaxation of the magnetisation**, when the spin ensemble returns to the equilibrium state (M_{xy} = 0, M_z = M_0). The relaxation of the magnetisation can be divided into a longitudinal part in the *z*-direction and a transverse part in the x,y-plane.

The relaxation of the longitudinal magnetisation M_z is called **T1 relaxation (or spin-lattice relaxation)** and is a measure for the release of energy to the environment. The relaxation process can be described by an exponential function with the time constant T1. The flipped magnetisation in the x,y-plane returns exponentially to its initial maximum valued M_0 parallel to B_0, i.e. $M_z=M_0$., as the spins return to the energetically favourable state parallel to B_0. Consequently, the T1 relaxation is responsible for the rebuild of the magnetisation M_z. The magnetisation M_z available for excitation determines the signal for a measurement. Therefore, the faster the T1 relaxation, the more magnetisation is available for excitation.

The relaxation of the transverse magnetisation M_{xy} called **T2* relaxation (or spin-spin relaxation)** arises from the loss of phase coherence of the spins in the x,y-plane after the excitation by an RF pulse. Directly after flipping the magnetisation in the x,y- plane, the magnetic moments are phase coherent. Shortly afterwards, however, some spins precess faster, others more slowly around the direction of the B_0 field, resulting in a loss of the phase coherence. The dephasing of the spins in the x,y-plane is caused by spin-spin interactions and magnetic field inhomogeneities. As a result, the spins diverge until evenly distributed in the x,y-plane. Since oppositely aligned magnetisation cancels each other out, the measurable signal decays exponentially. The resulting signal decay is called T2* relaxation, where T2* is the time constant of the decay.

1.3.4   Spatial encoding and k-space

MRI is a tomographic imaging procedure with the ability of a spatial encoding in three directions (x- ,y-, z-directions), i.e. the internal spatial structures of an object can be determined and depicted in three-dimensions (3D). For this purpose, the object is divided into small cuboidal volume elements (acronym: "volume element", voxel). For the image reconstruction,

the exact information about the respective point of origin for each voxel is required. The spatial information is obtained through additional magnetic gradient fields emitted by gradient coils in the three spatial directions, allowing the frequency or the phase angle to be set differently in each voxel. The field strength of these gradient fields varies along the respective location coordinate (location-dependent superimposition of B_0). The gradient fields have only a z component (point in the same direction as B_0) and are switched on and off during the measurement with variable amplitudes. In frequency encoding, the signal is sampled in equidistant time steps during the signal acquisition phase. The precession Larmor frequency changes along the frequency encoding gradient, giving the spin packages individual, location-dependent frequencies. In contrast, phase encoding gradients are applied before the signal is sampled. The strength of the gradient is changed with each excitation. While the gradient field is on, spins located at different locations precess at different frequencies, resulting in a phase difference between the voxels.

With frequency encoding, the location of spins along the encoding direction can be captured with a single excitation. With phase encoding, the excitation must be repeated N times. **In 3D** imaging methods, the entire volume of the nuclei is excited by an RF pulse and the location information is obtained by **one frequency-encoding gradient and two phase-encoding gradients**. To record a matrix of MR signals with NxNxM data points, the pulse sequence must be repeated N x M times. (N=number of repetitions of the first phase encoding gradient and M=number of repetitions of the second phase encoding gradient). The spatial resolution is determined by the strength of the gradients: in frequency encoding the strength while the gradient is on, in phase encoding the maximum strength of the gradient.

However, the measured raw data set of MR signals, the **hologram**, is not yet a usable 3D image. The mathematical data space in which the complex values of the measured hologram are saved is called **k-space**. The measured MR signal observes the spin precession over time and not the frequencies directly. Therefore, every data point in the k-space contains also spatial frequency and phase information. The measured MR signals in the k-space are processed with 3D Fourier transformations to reconstruct a 3D image. In most clinical applications, only the absolute value is used, and the local phase is discarded after Fourier transformation, since only the weighted proton density ρ is considered. The centre of the k-space (low spatial frequencies) contains information about the contrast/rough shapes of the image and the periphery of the k-space (high spatial frequencies) contains information about the details or edges of the image. The sampling of the k-space can be performed with different sampling schemes, whereby the path through k-space, is called trajectory. The most common trajectory is the cartesian sampling scheme, which fills the k-space line by line.

Different pulse sequences and techniques exist, which, for example, aim to generate different image contrasts, e.g. T1-or T2*-weighted images, to accelerate the acquisition, and/or to reduce image artefacts. An MRI pulse sequence consists of a particular series of RF pulses and magnetic field gradients that provide a complete image. The repetition time (TR) and the echo time (TE) are basic pulse sequence parameters. TR describes the time between two RF-pulses. TE describes the time between the RF pulse and the time at which the centre of the k-space is acquired. The MR signal intensity is determined by the proton density ρ, the used sequence (incl. sequence parameter like TR and TE), and the relaxation times of the different tissue types (but the pulse sequence determines the weighting, i.e. the contribution of the relaxation times to the signal).

1.3.5   Gradient-echo sequences

The MRI pulse sequences utilised in this work are **gradient-echo (GRE) sequences**. GRE sequences utilise small flip angles <30° in order to flip only a fraction of the longitudinal magnetisation M_z into the x,y-plane. A gradient echo is defined as the signal generated by a gradient inversion. As depicted in Figure 2, first the transverse magnetisation M_{xy}, i.e. the signal, is generated by an RF excitation. Second, the signal is manipulated by a dephasing gradient causing an accelerated loss of the phase relationship of the spins to each other, i.e. accelerated dephasing of the transverse magnetisation M_{xy}. Third the echo is generated by a rephasing gradient (readout gradient) that rebuilds the phase relationship, i.e. rebuilding of the transverse magnetisation M_{xy}. The rephasing gradient reverses the phase shifts induced by the dephasing gradient and re-establishes the MR signal as an echo. During the dephasing gradient a whole k-space line can be sampled with sufficient signal. The k-space centre is located at the centre of the echo.
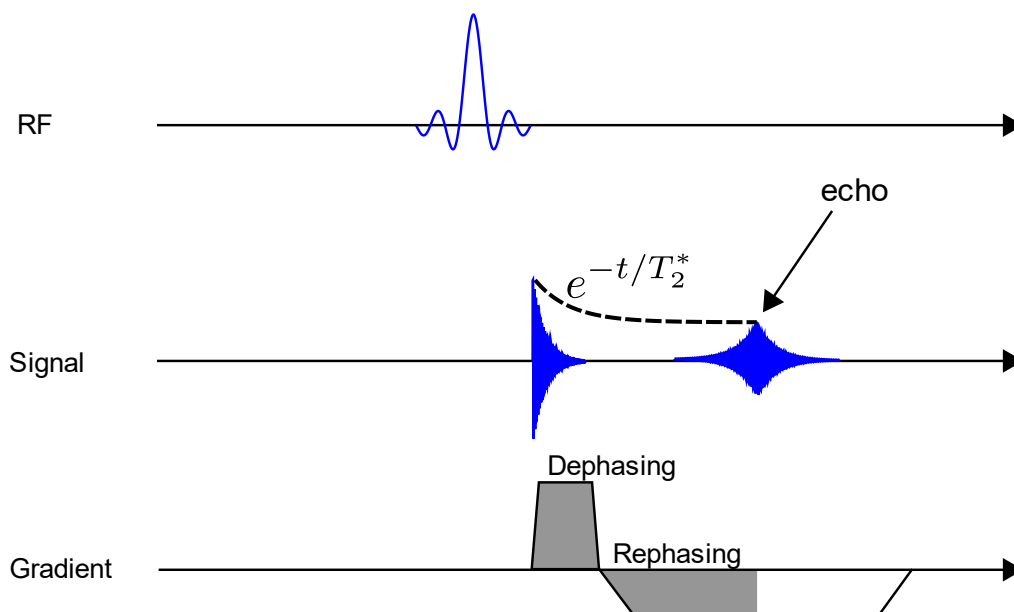
Figure 2: Diagram depicting the generation of a gradient echo using a dephasing and a rephasing gradient.
[https://upload.wikimedia.org/wikipedia/commons/3/3e/Gradient_echo_MRI.svg;
IngFrancesco, translation by Mikael Häggström, CC BY-SA 2.5 <https://creativecommons.org/licenses/by-sa/2.5>, via Wikimedia Commons]

The sequences used in this work are based on the so-called **Fast Low Angle SHot (FLASH) sequence** (Haase et al. 1986), which is a spoiled GRE sequence. In a GRE sequence, spoiling destroys the transverse magnetisation M_{xy} after each signal acquisition, i.e. before each RF-pulse. As a result, no transverse steady-state is established which allows the sequence to be used for the acquisition of T1-weighted images. In this sequence, the T1 relaxation between the excitation pulses builds up exactly as much magnetisation as was redirected by the excitation from the *z*-direction into the x,y-plane to establish a constant longitudinal equilibrium, i.e. a longitudinal steady state magnetisation occurs in which excitation and relaxation are in equilibrium. This can be achieved, when TR is chosen much shorter than usual T1 relaxation times and when the longitudinal magnetisation M_z is only slightly reduced by using small flip angles (<30°). The constant longitudinal equilibrium magnetisation is maintained over any length of measurement time, which enable time resolved acquisitions with a high temporal resolution. In addition, very high-resolution three-dimensional images can be taken in a short measuring time.

The signal S from a spoiled-GRE sequence in the equilibrium is determined by TR, TE and the flip angle α as well as by the three intrinsic tissue parameters T1, T2* and proton density ρ:

$$S = \rho \cdot \frac{\sin \alpha \cdot (1 - e^{\frac{-TR}{T1}})}{1 - \cos \alpha \cdot e^{\frac{-TR}{T1}}} \cdot e^{\frac{-TE}{T2*}} \qquad\qquad 2$$

The strength of the T1-weighting, i.e. how much the MR signal depends on the different T1 relaxation times of tissues, can be chosen with a suitable setting of the flip angle α and TR. The larger the flip angle α and shorter TR, the stronger the T1-weighting. The minimum TR is

mainly restricted by the possible strength of the gradients and gradient switching times incl. "dead time". The echo time TE determines the T2* weighting of the signal in a GRE image. For a strong T1-weighted image with a minimal possible T2* weighting, TE must be chosen as short as possible. In a strong T1-weighted image, the contrast and brightness of the image are predominately determined by the T1 properties of tissue.

The optimum flip angle, which produces the maximum signal, is the so-called **"Ernst angle"** α_{Ernst}

$$\alpha_{Ernst} = \arccos e^{\frac{-TR}{T1}} \qquad\qquad 3$$

However, the flip angle α can be chosen bigger than the optimal signal in order to increase the contrast. The **image acquisition in spoiled GRE sequences can be accelerated** by techniques like parallel-imaging or asymmetric echo. Parallel imaging techniques, such as GRAPPA, reduce spatial encoding steps, as the known placement and sensitivies of multiple receiver coils are utilised to complete the spatial allocation of the MR signal (Griswold et al. 2002). With an asymmetric echo, the dephasing is only incompletely performed, because a shorter dephasing gradient is used. As a result, the k-space is sampled only partially, but the k-space centre can be reached earlier, i.e. TE is shorter. An incomplete sampling of the k-space can be done because a Fourier transformation of a real function is symmetrical and thus the missing parts of the k-space can be calculated from the measured parts of the k-space.

1.3.6 Implications of lung characteristics on MRI

In lung MRI, the water in the lungs provides the primary MR signal, which is present in the lung parenchyma (blood and surrounding tissue). However, a large part of the lung volume

consists of air, which results in a low proton density and thus low signal-to-noise ratio (SNR). Consequently, the balance in lung MRI between resolution, SNR, and acquisition time is more difficult than in many other organs due to the low SNR. The longitudinal and the transverse relaxation depend strongly on the thermal mobility of molecules (physical state) and their surroundings. The average T1 of lung parenchyma in healthy lungs is approximately 1200ms, which mainly depends on the blood fraction and their environment (Jakob et al. 2001). The lungs are comprised of many interfaces of different compartments to perform their primary task of gas exchange, as described in section 1.1. Since air and tissue have different susceptibilities, local field gradients arise at these interfaces, which lead to a T2* shortening. This means that protons near these interfaces precess with strongly varying Larmor frequencies and thus quickly lose their phase coherence. As a result, T2* of the lung parenchyma is extremely short with approximately 1-2ms at 1.5T scanners (Hatabu et al. 1999a) and susceptibility artefacts occur in the surroundings of air-tissue interfaces. Therefore, fast scan techniques, such as GRE, with short TE are preferable for lung MRI. However, even with a short TE, the SNR in the lung is low, particularly relative to the surrounding tissue. The latter is problematic as artifacts affecting the lungs may contain signal components from outside the lungs, which can be strong relative to the lung signal itself.

Respiratory motion during inspiration and expiration must be considered for the acquisition of MR images. The two sequences used in this work were configured for an acquisition in breath-hold. If the breath-hold is performed incorrectly, artefacts are produced, and compartments are shifted between voxels. Unfortunately, the CA application and thus the acquisition of a DCE-MRI sequence cannot be easily repeated, which is why an incorrectly executed breath-hold can lead to the exclusion of the examination from further analyses or images have to be corrected for respiratory motion.

1.3.7   MRI pulse sequence utilised for lung segmentation

The segmentation of the lungs, which is necessary for the computer-aided automated quantification of pulmonary perfusion (cf. section 1.4.4), was performed in this work using MR images acquired with an **ultra-fast GRE sequence**. The utilised MR pulse sequence was optimised to deliver the best possible spatial resolution and SNR in one single breath-hold of several seconds. For this purpose, 3D images were acquired with a relatively short TE and a flip angle α, which delivers the optimal signal in the lung parenchyma. In addition, several techniques were employed to accelerate the acquisition (single breath-hold) while still achieving the required spatial resolution. For example, padding the acquired k-space with zeros before the data are transformed into image space results in an image interpolated to a higher resolution. This process is called zero-filling and makes use of the information contained in the phase of the complex raw data that is lost after the image reconstruction.

1.3.8   Gadolinium-based contrast agent

MRI CA are used in medical imaging to increase the sensitivity and specificity of a test and to determine the perfusion of an organ. In this work, a CA containing extracellular paramagnetic gadolinium (Gd) chelates was used to assess pulmonary perfusion. Paramagnetic atoms contain unpaired electrons and thus have a net electronic spin, with the magnetic field induced by electron spins being much stronger than that of proton spins. Gd can be used as its electron spin relaxation time matches reasonably well the Larmor frequency of protons in water or fat molecules at field strengths around 1T. Due to its toxicity, Gd must be attached to a chelate molecule in order to be used as a CA in humans. For example, diethylenetriaminepentaacetic acid (DTPA) is highly stable and can be used to bond Gd (forming Gd-DPTA). The paramagnetic interaction between gadolinium chelate-containing CA and a proton is stronger by a factor of ~500 000 than the interactions between two protons.

The precession of the hydrogen atoms in the tissue and thus also the signal intensity of the MR image is influenced by the strong interactions between the CA and the protons. The particles of the paramagnetic CA act as T1 relaxation centres. These relaxation centres cause temporally rapidly fluctuating fields, which, in turn, lead to an acceleration of the T1 relaxation and thus to a signal increase in T1-weighted images where CA is locally present.

In the lungs, the extracellular CA resides within the pulmonary vascular bed, as the system is assumed to be a closed system without extravasation of the CA in healthy tissue regions during the first pass of the CA, i.e**. no leakage** of the intravenously injected CA from the normal intravascular compartment into surrounding tissues. The local signal increase caused by the CA improves the measurement conditions inside the lungs as it leads to an increase in SNR/CNR.

The relaxation rate R1 (1/T1) is directly linearly proportional to the concentration of the CA, but the signal intensity change is not linearly proportional to the concentration of the CA. However, **at low CA concentrations, the signal intensity is approximately linearly proportional to the CA concentration, but not at high CA concentrations**. Therefore, the dose of the intravenously injected CA must be carefully chosen if signal changes are to be quantified. Too low dosage can lead to an insufficient signal amplification (low CNR) in the lung parenchyma, but too high dosage would lead to a non-linear relationship, especially in areas with a high percentage of CA per voxel, such as large vessels. A particular challenge for pulmonary perfusion quantification is the high percentage of CA occurring in the main pulmonary artery where the AIF for the perfusion quantification is measured (cf. section 1.4.2). A non-linear relationship in the AIF can lead to a variable underestimation of the AIF, which in turn can lead to errors in the perfusion quantification. The CA concentration-to-signal

intensity relationship with special focus on DCE-MRI of the lungs was investigated previously. The study showed that even low doses of CA can exceed the range of linearity in the main pulmonary artery (Puderbach et al. 2008). Several methods exist to account for the non-linearity in the main pulmonary artery for quantitative computer-aided perfusion computations (Neeb et al. 2009; Risse et al. 2006), which are described in more detail in section 2.3.1.

1.3.9 DCE-MRI of the lung

DCE-MRI data of the lung is commonly acquired with a **spoiled 3D GRE sequence for time-resolved angiography** (Fink et al. 2005c). For the assessment of pulmonary perfusion, the contrast enhancement of the administered CA bolus in the small vessels (smaller than a voxel) of the lung parenchyma is of particular interest. A dynamic, i.e. temporally resolved, acquisition is used, which measures the same scan region several times successively at short intervals. In the lungs, a sufficient temporal resolution for perfusion assessments is preferably approximately 1.5 s or below to enable a quantitative assessment of the perfusion or to differentiate phases of perfusion (Ley and Ley-Zaporozhan 2011). Usually the complete DCE-MRI dataset is acquired in a single breath-hold. Consequently, only the first passage of the CA through the lung parenchyma can be observed during the first 20-30s without breathing artefacts.

The spoiled 3D GRE sequence was **optimised for the contrast enhancement of the CA** in the lungs. TE had to be chosen extremely short, due to the short T2* in the lung parenchyma (cf. section 1.3.6), preferably less than 1ms. In the DCE-MRI pulse sequence, the flip angle α is chosen to deliver the optimal signal from the CA, which is therefore larger than the flip angle α of the GRE sequence used to generate the MR images for lung segmentation. Consequently, spatial resolution and the SNR of the lung parenchyma and chest wall is

substantially lower compared to the GRE sequence used to generate the MR images for lung segmentation, which is why the DCE-MRI pulse sequence is not appropriate for lung segmentation. Nevertheless, relative to the size of the functional units regulating lung perfusion, the spatial resolution of DCE-MRI data is high. In this work the voxel size was 1.8×1.8 mm and the slice thickness 5.0 mm and the secondary pulmonary lobule as smallest functional unit regulating lung perfusion has a size of 1-2.5 cm in diameter (Heitzman et al. 1969; Webb 2006).

The spatio-temporal resolution of the DCE-MRI pulse sequence was improved by applying **keyhole-imaging** techniques (Fink et al. 2005a; Hennig et al. 1997; Laub and Kroeker 2006; Vaals et al. 1993). The keyhole imaging technique samples only the central k-space (low spatial frequency information) at each time point completely, but the peripheral k-space (high spatial frequency information) is only partially sampled in a stochastic manner at each time point. To fill the missing points of the peripheral k-space, data from previous and later acquired time points are copied into the k-space by the keyhole technique. This is done, because the CA changes only the signal intensity (contrast), i.e. the dynamic information, which can be obtained from the centre of the k-space, but not the actual structure of the tissue imaged (peripheral k-space). The partial sampling of the k-space enables the use of shorter dephasing gradients, resulting in a possible shorter TE.

However, due to the keyhole technique, **respiratory motion** by incorrectly executed breath-holds results in image artefacts at all shared time points, due to the temporal sharing of the high frequency k-space data. Furthermore, the movement of the heart leads to artefacts due to the keyhole concept in the shared phases, especially in the temporal vicinity of the CA passage through the left heart. In general, the keyhole concept introduces large-scale artefacts beyond pure noise to achieve the time resolution necessary for perfusion assessments. In this

case, these artefacts can be determined by the signal outside the lungs, which leads to the strong artifacts relative to the lung signal. Respiratory motion negatively influences DCE-MRI data of the lungs further. A change in lung volume leads to a change in lung density/proton density and, therefore, in the MR signal. In addition, respiratory motion moves tissue structures, such as vessels, between voxels and thus changes the MR signal between time points for individual voxels. For these reasons, patients must hold their breath during the image acquisition to enable the tracking of the complete first CA passage through the lungs. Typical breath-hold times are up to 35 s, which is difficult for many seriously ill CF or COPD patients (Maxien et al. 2013; Ter-Karapetyan et al. 2018).

Overall, DCE-MRI data of the lungs are **adversely affected by pronounced artefacts** and low CNR. Artefacts arise due to the keyhole concept, which is needed to achieve the necessary spatio-temporal resolution for the pulmonary perfusion assessment and the low proton density in the lungs. The low contrast enhancement in the lung parenchyma is mainly caused by the limitation in the dosing of the CA. The dose of the CA is chosen small enough to ensure a linear relationship between CA concentration and MR signal in the lung parenchyma.

1.4 Computer-aided perfusion assessment

Pulmonary perfusion abnormalities in DCE-MRI data are characterised by absent or delayed contrast enhancement. **Computer algorithms** can quantitatively assess pulmonary perfusion by calculating parameters like PBF and PBV or alternatively by calculating the extent of perfusion abnormalities in relation to the total lung volume as a more relative measure. In most cases, pharmacological models are applied to assess pulmonary perfusion quantitatively with computer algorithms (Ohno et al. 2007; Ravesh et al. 2013; Sourbron and Buckley 2011). Thereby, the contrast enhancement in the lung parenchyma during the first pass of an

intravenously injected CA bolus is exploited. Abnormal perfusion leads to local changes in PBF and PBV, which can be depicted voxel-wise as color-coded maps. In addition, also the extent of perfusion abnormalities can be depicted in color-coded maps.

1.4.1   Signal to concentration conversion

As described in section 1.3.8, DCE-MRI measures the temporal change in MR signal intensity caused by the CA, but not the CA concentration directly. To quantify pulmonary perfusion, the **signal intensity time course S(t) measured by DCE-MRI must be converted into a CA concentration time course C(t)**. The most frequently used methods assume a linear relationship between the CA concentration and the measured MR signal intensity for the conversion (Ohno et al. 2004; Østergaard et al. 1996; Ravesh et al. 2013; Sourbron et al. 2006). Thus C(t) can be approximated by the relative signal change over time $S_{rel}(t)$.

$$C(t) \propto S_{rel}(t)$$

4

1.4.2   Indicator dilution theory and lung perfusion

The most frequently used DCE-MRI perfusion quantification method in the lungs makes use of the **theory of the indicator dilution**, which is based on the principles of tracer kinetics for non-diffusible tracers (Fink et al. 2005c; Meier and Zierler 1954; Ohno et al. 2004). The model consists of a closed flow system with one single inflow, one single outflow, one single tissue compartment and no extravasation of the CA. The theory assumes a constant volume of the CA and a constant flow rate when the CA enters and exits the system (Meier and Zierler 1954). As depicted in Figure 3, the CA enters the tissue from an arterial inflow at a concentration $C_a(t)$ and leaves the tissue through the venous outflow at a concentration C(t). The tissue impulse response function IRF describes the observed response of the tissue after the injection of the

CA and is also called transport function. The IRF is a probability density function of the transit times t of the CA through the tissue, which depends on the vessel structure and flow. The model/theory requires an infinitely small bolus of unit volume as input, i.e. Dirac delta function (δ-function). Therefore, the CA is injected as a bolus (the shorter the injection time of the CA, the better the impulse condition of the theory is fulfilled). In the following, $C_a(t)$ is also referred to as arterial input function (AIF) and C(t) as the output concentration function.
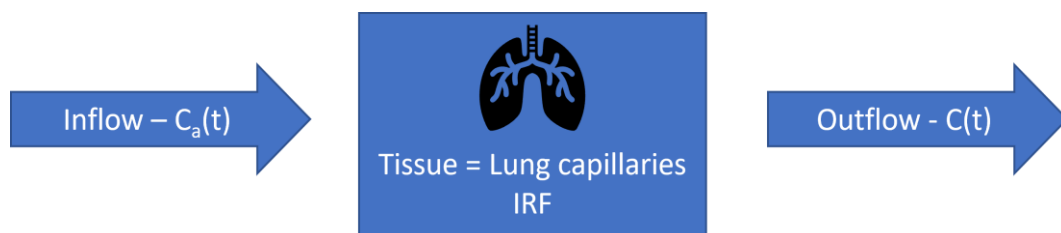
Figure 3: Principle of the indicator dilution theory for pulmonary perfusion quantification. The model is also referred to as a one-compartment-model or in signal processing as a 'linear time-invariant system' or 'black-box system'. The name 'black box system' comes from the fact that no assumptions on the distribution of the CA in the tissue are made.

According to the definitions of the indicator dilution theory for **linear time-invariant systems**, C(t) can be calculated by the convolution of $C_a(t)$ with IRF

$$C(t) = C_a(t) \otimes IRF(t) = \int_0^t C_a(t) \cdot IRF(t - \tau)d\tau \qquad\qquad 5$$

where $\otimes$ denotes mathematical convolution.

For the quantification of pulmonary perfusion parameters, such as PBF and PBV, the IRF must be determined. PBF is defined as the maximum height of IRF and PBV as time-integral of IRF (Ohno et al. 2004; Sourbron et al. 2006). A widely used approach in bolus tracking to solve Eq. 5 for IRF is the model independent (nonparametric) deconvolution of C(t) with $C_a(t)$. However, as the measured bolus tracking data contain noise, the **algebraic deconvolution is**

an ill-posed problem, i.e. even a small amount of noise in the data may result in physiologically meaningless solutions. The noise-sensitivity can be reduced by employing a process called "regularisation" (cf. section 2.3.2). Many studies already investigated regularisation approaches for algebraic deconvolution in bolus-tracking using real and simulated MRI data (Calamante et al. 1999; Ravesh et al. 2013; Sourbron et al. 2004).

In general, perfusion (more precisely hemoperfusion) is the supply of blood to organs or parts of organs. Perfusion in the sense of a quantity is defined as **blood flow BF**. BF is the volume of blood that flows through an organ per unit of time with the unit $\frac{ml}{min}$

$$BF = \frac{\Delta V_{Blood}}{\Delta t}$$

6

where ΔV_{Blood} is the blood volume in vessels that flow through an organ and Δt is the time unit. The blood volume is usually set in relation to the mass of a reference volume or to a reference volume V_{Lung} to calculate the regional blood flow rBF. In MRI it is only possible to measure the relative flow related to a reference volume.

$$rBF = \frac{\Delta V_{Blood}}{V_{Lung} \cdot \Delta t}$$

7

In the following, rBF is named PBF with the unit $\frac{ml}{100ml \cdot min}$, which was established in DCE-MRI experiments to reflect how much blood flows through 100 ml of lung tissue per minute. For a healthy young man with a $\Delta V_{Blood}/\Delta t$ of 6 l/min and a total lung volume of 7 l, PBF for the entire lung is approximately 85 ml/100ml/min (Larsen and Ziegenfuß 2004).

The **regional pulmonary blood volume (rBV)** used in this work is defined as the volume of blood in a reference volume with the unit $\frac{ml}{100ml}$

$$rBV = PBV = \frac{\Delta V_{Blood}}{V_{Lung}} \qquad\qquad 8$$

PBV measures the amount of blood in 100 ml of lung tissue. In the main pulmonary arteries, the blood volume in a region of interest (ROI) should be approximately 100 ml/100ml, i.e. 100 %. Therefore, the blood volume in the main pulmonary arteries can be used to control the PBV calculation.

1.4.3   Perfusion defects in percent

In addition to the quantification of the absolute flow and volume values using PBF and PBV, further analysis strategies have been developed in this work to evaluate the extent of perfusion abnormalities. For this purpose, unsupervised image clustering algorithms were used to quantify the extent of perfusion abnormalities in the lungs relative to the lung volume, which will be abbreviated in the following as **perfusion defects in percent (QDP).** The basic idea is to classify voxels as defective if their value is low compared to the other lung voxels. By putting the extent of defective voxels in relation to the lung volume, the calculation in percent is achieved.

Unsupervised clustering algorithms belong to the group of unsupervised machine learning tasks. They were already applied in clinical studies to Fourier decomposition- (FD), hyperpolarised helium-, and xenon-MR images to quantify ventilation or perfusion defects. In

addition, unsupervised clustering algorithms are often used in image processing for various tasks, such as image segmentation (=distinguishing between object and background).
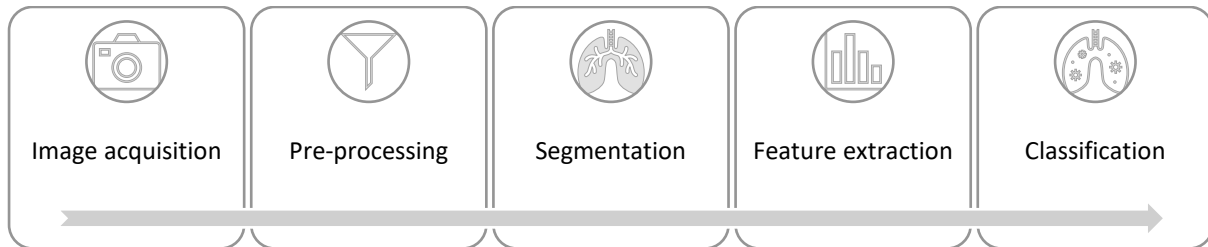
Figure 4: Image processing chain depicting the single steps needed to use clustering algorithms.

In general, 5 main steps are used **in an image processing chain** to enable feature classification with unsupervised clustering algorithms, as shown in Figure 4.

1. Images must be acquired and uploaded to the analysis platform

2. Image pre-processing steps are usually required before clustering algorithms can be used, e.g. the application of a filter to emphasise edges or the compensation of inhomogeneities in the image. DCE-MRI data offer the possibility to use mathematical models, such as the indicator dilution theory, during the pre-processing.

3. Image segmentation may be required to limit the area of the image to an ROI. For example, in this work, an automatic segmentation of the lungs was performed.

4. Feature extraction is the first step where the clustering algorithm itself is used. The clustering algorithm extracts features of interest from the image, e.g. signal intensities, and automatically groups them into clusters. Usually, the number of clusters is pre-specified.

5. The final step is the classification of the identified clusters, which determines the consequence of each cluster, e.g. defect or no defect.

In this work, pixel-based (or voxel-based) unsupervised clustering of signal intensities was evaluated:

- **Otsu´s method:**

  For the separation of voxels into clusters, Otsu´s method identifies thresholds from intensity histograms by minimising the inter-class intensity variance. For two clusters, Otsu´s method searches for one threshold in the histogram (Otsu 1979).

$$\sigma_\omega^2(t) = \omega_0(t) \cdot \sigma_0^2(t) + \omega_1(t) \cdot \sigma_1^2(t) \qquad 9$$

  where t is the threshold of interest, σ_ω^2 is the weighted sum of variances of the two classes, ω_0 and ω_1 are the probabilities of the two clusters, and σ_0^2 and σ_1^2 are the variances of the two clusters.

- **k-means clustering:**

  k-means clustering utilises the within-cluster variances (squared Euclidean distances) to separate voxels into clusters. The aim is to minimise the within-cluster sum of squares, i.e. the variance of each cluster.

$$\arg \min_C \sum_{i=1}^{k} |C_i| \, Var C_i \qquad 10$$

  where C is the cluster and k is the number of clusters.

- **Percentile threshold:**

  A method based on one percentile threshold clusters the voxels in the lungs into two clusters. The percentile threshold is usually empirically determined and must be multiplied with a factor. The percentile must be above the median to reflect normal perfused lung parenchyma and the factor must be less than 1. The factor is needed to enable detection of different percentages of defects. In previous studies, the 75th percentile threshold multiplied by 0.5 or the 80th percentile threshold multiplied by 0.6 was determined as a robust threshold to differentiate between healthy and pathologic tissue (Heimann et al. 2012; Kaireit et al. 2019).

1.4.4   Automatic lung segmentation

Lung segmentation is defined as a process of identifying the lung contours that separate the lungs from the surrounding thoracic tissue, such as the chest wall and the heart. The segmentation of the lungs is a prerequisite for the assessment of pulmonary perfusion by computer algorithms and can be performed automatically or manually by plotting ROIs. The aim of this work was to perform an automatic lung segmentation without manual correction. In comparison with DCE-MRI data, non-dynamical sequences of the lungs can have substantially higher spatial resolution, better contrast between the lungs and the thorax wall, higher SNR in the lung parenchyma, and require shorter breath-holds as described in section 1.3.7. Therefore, in a previous study, the lungs were segmented from non-dynamical image data acquired prior CA application and the segmented lung mask was transferred to the DCE-MRI dataset using image registration (Kohlmann et al. 2015). The shorter breath-hold duration for the non-dynamical image acquisition compared to DCE-MRI reduces errors in the breath-holding manoeuvre.

In this work, **region growing techniques** are used for lung segmentation, including the identification of seed points for each lung. The basic principle of the region growing algorithm is to include all neighbouring voxels with similar intensities starting from a seed point. However, in the lungs, region-growing algorithms tend to include the trachea and to combine both lungs in the area of the lung apices. The trachea is connected to the lungs and filled with air, which prevents the region growing algorithm from identifying a border between the trachea and the lung tissue. Therefore, the trachea must be identified and excluded separately. In the area of the lung apices, the two lungs are only separated by a thin layer of tissue, which means that the signal increase of the tissue layer is relatively low compared to the lung parenchyma due to the small amount of tissue. In case the region growing algorithm cannot detect the border between the two lungs, further image processing steps are needed to accurately separate the two lungs. Watershed transformations, which were developed in image processing to segment continuous regions into distinct objects, are useful to separate the two lungs. The basic principle of watershed transformation is to identify watershed ridges, assuming that the image resembles a topographic relief and is flooded with water from below. When the floods of two different catchments start to mix, a dam is built to prevent the mixing of the floods, i.e. it is separated into two objects. A grey scaled image is transformed into a topographic relief by converting light pixels to high elevations and dark pixels to low elevations (Meyer 1994). However, the watershed transformation tends to lead to an over-segmentation, especially in images with low SNR.

1.5 Objectives

The overall purpose of this work was to develop a robust and clinically meaningful method to quantify pulmonary perfusion using DCE-MRI data in patients with muco-obstructive lung disease. As outlined in the previous sections of the introduction, DCE-MRI in the lungs is challenging and has its limitations, which negatively affect the reproducibility of PBF and PBV, i.e. absolute flow and volume quantification. For this reason, an algorithm was developed to automatically quantify the extent of pulmonary perfusion in percent (QDP) using unsupervised clustering algorithms, i.e. relative quantification. The use of unsupervised clustering algorithms leads to intrinsic normalisation and can reduce variability compared to absolute perfusion quantification. For the development of QDP as a new imaging-based biomarker, several technical validation steps were performed followed by several clinical validation steps.

The **algorithm for the quantification of QDP** was developed and optimised using data from the 'COSYCONET' COPD cohort (study details are given in section 2.1.1) by comparing different unsupervised clustering methods and image pre-processing methods. Thereafter, the reproducibility of QDP was investigated in CF and COPD patients who underwent DCE-MRI at baseline and one month later (reproducibility study: study details are given in section 2.1.2). The development of QDP was primarily based on comparisons with a visual MRI perfusion score, but also with quantitative CT parameters for emphysema and fSAD, and with PFT parameters, since perfusion abnormalities are associated with both airflow limitations and the destruction of lung parenchyma. Furthermore, the performance of QDP was compared to the performance of PBF and PBV.

2 MATERIALS AND METHODS

2.1 Study population

2.1.1 COSYCONET study

The first study in this work was based on data from the imaging sub-study of the national COPD cohort entitled "Impact of Systemic Manifestations/Comorbidities on Clinical State, Prognosis, Utilisation of Health Care Resources in Patients with COPD" (COSYCONET (NCT01245933); substudy "Image-Based Structural and Functional Phenotyping of the COSYCONET Cohort Using MRI and CT" (MR-COPD, NCT02629432)). The key inclusion criteria were male and female subjects aged 40 years and older, diagnosis of COPD according to the GOLD criteria (Singh et al. 2019) or chronic bronchitis. Thus, the study included subjects of GOLD 1–4 categories and subjects with no assignable GOLD category including the former GOLD 0. A detailed description of the in- and exclusion criteria of COSYCONET was published by Jörres et al. (Jörres et al. 2010). Institutional ethics committee approval was obtained (Ethik-Kommission der Medizinischen Fakultät der Universität Heidelberg, S-656/2012) and all subjects gave their written informed consent prior to study conduct.

For this work, a subset of 103 subjects was selected who were examined in the same centre (Thoraxklinik Heidelberg). Only a cross-sectional evaluation of the COSYCONET study data was done. 20 (19.4%) subjects were excluded due to missing MRI acquisitions, substantial respiratory artifacts, or other inadequate MRI data quality, resulting in 83 subjects remaining in the analysis (Table 1).

Table 1: Patient demographics of the COSYCONET study subset

	Total	At risk for COPD	Former GOLD 0	GOLD 1	GOLD 2	GOLD 3	GOLD 4
Demographics							
n	83	5	11	4	29	24	10
Age (y)	65.7 ± 9.0	65.6 ± 6.8	69.5 ± 7.2	62.8 ± 9.5	66.4 ± 9.5	64.7 ± 10.2	62.7 ± 6.6
Sex (female/male)	44 / 39	2 / 3	7 / 4	1 / 3	15 / 14	14 / 10	5 / 5
Pack years	36.9 ± 28.8	32.2 ± 19.2	12.8 ± 13.0	23.0 ± 4.3	34.2 ± 24.2	39.6 ± 33.9	74.4 ± 22.5
BMI (kg/m^2)	26.2 ± 4.6	27.2 ± 6.5	29.5 ± 4.2	27.0 ± 4.9	25.8 ± 4.5	25.6 ±4.7	23.9 ± 3.1

Information on the number of pack-years was only available for 45 patients. Body mass index (BMI) data was only available for 80 patients. Pack years are calculated by multiplying the number of packs smoked (20 cigarettes) per day by the number of years the patient has smoked. Data presented as mean ± standard deviation (SD).

2.1.2 Reproducibility study

Data for the second study of this work were derived from a prospective observational study at the Thoraxklinik Heidelberg, which was approved by the institutional ethics committee (S-126/2015). Informed written consent for examination and data evaluation was obtained from all subjects prior to study start. The study was designed to test the reproducibility of MRI-derived parameters in clinically stable CF and COPD patients. MRI visits were performed at baseline (MRI1) and one month (30.0 ± 2.5days) later (MRI2). PFT was carried out on both MRI visits. Adverse events were recorded at both visits.

The diagnosis of CF was based on clinical symptoms, confirmed by increased sweat Cl⁻ concentrations (≥ 60mmol/l) and *CFTR* mutation analysis. In pancreatic sufficient patients with borderline sweat test results (sweat Cl⁻ between 30 – 60mmol/l) the assessment of CFTR protein function was performed in rectal biopsies according to established diagnostic criteria as previously described (Graeber et al. 2015; Hirtz et al. 2004). The diagnosis of COPD was made according to established criteria by the GOLD consortium (Singh et al. 2019). Patients must not have any hypersensitivity to gadolinium-based CAs. CF patients needed to be aged

$\geq$ 18years with a pre-bronchodilator forced expiratory volume in 1 second percent predicted (FEV1% predicted) $\geq$ 30% at baseline. COPD patients needed to be aged $\geq$ 40years with post-bronchodilator FEV1% predicted $\geq$ 30% and the ratio between the forced expiratory volume in 1 second and forced vital capacity (FEV1/FVC) < 70%.

In total, 35 patients, 15 with CF and 20 with COPD (Table 2), were prospectively recruited within one year and completed both MRI examinations in stable clinical condition. Clinically stable was defined as constant maintenance therapy and freedom from pulmonary exacerbation as described elsewhere (Fuchs et al. 1994; Rosenfeld et al. 2012; Singh et al. 2019). In case an enrolled patient experienced a pulmonary exacerbation and/or a major change in symptoms or therapy after the first MRI, the patient needed to return to baseline medication and symptoms more than seven days prior to second MRI. Stability of PFT parameters and MRI perfusion score of the patients in this study was confirmed by a previous work (Wielpütz et al. 2019).

Table 2: Patient demographics in the reproducibility study. Submitted for publication.

	Cystic fibrosis	COPD	Both groups
Demographics			
n	15	20	35
Age (y)	29.3 ± 9.3	66.5 ± 8.9	50.6 ± 20.7
Sex	2 f / 13 m	5 f / 15 m	7 f / 28 m
History of smoking, n	2	20	22
Pack years	0.7 ± 0.2	52.3 ± 22.2	47.6 ± 26.8
Time since diagnosis (y)	20.9 ± 11.7	8.1 ± 5.5	13.6 ± 10.7
BMI (kg/m^2)	21.8 ± 2.8	25.1 ± 3.7	23.7 ± 3.7
P. aeruginosa status	5 chronic 4 intermittent	-	-
S. aureus status	9	-	-
Aspergillus ssp. status	4 chronic 4 intermittent	-	-

Data presented as mean ± SD. Bacterial colonisation was not assessed in COPD.

2.2   MR image acquisition

In both studies the same 1.5T MR scanner (Magnetom Aera, Siemens Healthineers) and a standardised chest MRI protocol (Table 3) were used for the acquisition as previously described (Bertram J. Jobst et al. 2015; Stahl et al. 2017; Triphan et al. 2018; Wielpütz et al. 2014; Wielpütz et al. 2018).

The sequence used to generate the MR images for lung segmentation was a 3D volume-interpolated breath-hold examination (VIBE) GRE pulse sequence in coronal and transverse orientation (Siemens Healthineers, Erlangen, Germany). The combination of GRE sequences with parallel imaging methods and slice interpolation techniques ensures a full lung volume coverage at the desired spatial resolution within one breath-hold of several seconds (Wild et al. 2012). The sequences were acquired in inspiratory breath-hold with a total acquisition time of ~17s. Compared to the DCE-MRI pulse sequence, the VIBE sequence provides a higher SNR with lower T1-weighting, due to the smaller flip angle α. This facilitates the differentiation of the lung parenchyma from the chest wall for lung segmentation.

DCE-MRI data were acquired with a time-resolved 3D angiography with stochastic trajectories (TWIST) spoiled T1 GRE pulse sequence (Siemens Healthineers, Erlangen, Germany). Key-hole imaging and parallel imaging with view sharing were used to achieve the needed spatio-temporal resolution (Fink et al. 2005c; Laub and Kroeker 2006). The sequence was T1-weighted with a short TR and high flip angle α. For the contrast-enhancement, either a fixed dose of 2ml or less than 0.1mmol/kg body weight of gadolinium-based CA (Gadobutrol (Gd-BT-DO3A), Bayer Vital GmbH, Leverkusen, Germany) was injected intravenously at a rate of 4ml/s with a power injector (Medtron, Saarbrücken, Germany) followed by a saline chaser. The 20 time points of the DCE-MRI pulse sequence were acquired in inspiratory breath-hold,

resulting in a total acquisition time of ~33s with a temporal resolution of ~1.6s. The DCE-MRI acquisition started up to 5s before the CA injection and continued during the passage of the CA through the lungs. MRI was performed in most cases after patients had taken their maintenance medication.

Table 3: Standardised MRI protocol (Schiwek et al. 2021; Triphan et al. 2018)

Sequence	Orientation	Mode	TR (ms)	TE (ms)	α (°)	ST (mm)	Slices	FoV (mm²)	Matrix	Voxel size (mm)
VIBE	tra	3D	3.61	1.69	5°	4.0	88	400x300	320x240	1.3 x 1.3
VIBE	cor	3D	3.35	1.63	5°	4.0	56	400x400	288x288	1.4 x 1.4
TWIST	cor	3D	1.80	0.74	20°	5.0	44	450x366	256x208	1.8 x 1.8

All three sequences were acquired in inspiratory breath-hold. For the TWIST sequence, 20 consecutive acquisitions were made, and a gadolinium-based contrast agent was injected intravenously. tra = transverse orientation cor = coronal orientation, ST = slice thickness, FoV = Field of view.

2.3 Pulmonary perfusion quantification

All quantitative MRI-derived perfusion parameters were calculated using an MRI analysis pipeline developed entirely within the scope of this work and written in MATLAB (R2019a, The MathWorks, Inc., Natick, Massachusetts.). The individual steps are described in the following text. All image processing steps used for the final evaluation of the patient data were performed fully automatically, unless otherwise stated.

2.3.1 Concentration maps

As described in section 1.4.1, C(t) can be approximated by the relative signal change over time/signal enhancement $S_{rel}(t)$. Under the assumption that all time points of the DCE-MRI data show the same anatomical region, the basic idea behind the approximation of the CA

concentration with $S_{rel}(t)$ was the need to remove the baseline signal of tissue and blood before the CA enters the tissue. Thus, a frequently used approach to calculate S_{rel} is the subtraction of the baseline signal S_0 from the measured signal intensity time course $S(t)$ (Pianykh 2012)

$$S_{rel}(t) = S(t) - S_0 \qquad\qquad 11$$

However, as MRI delivers signal intensities in arbitrary units (a.u.) for every voxel over time, a normalisation of the signal change to the baseline signal S_0 delivers more comparable values between measurements (Ohno et al. 2004; Østergaard et al. 1996; Ravesh et al. 2013)

$$S_{rel}(t) = \frac{S(t) - S_0}{S_0} \qquad\qquad 12$$

Due to the physical properties of the lung tissue, the signal and SNR in the lung parenchyma was low before the CA arrives. Dividing by S_0 can thus lead to artefacts and noise amplification, especially in regions with perfusion abnormalities (= low contrast enhancement), as depicted in Figure 5. Consequently, a normalisation to the baseline signal was not considered useful in the specific case of parenchyma perfusion quantification, which is prone to low SNR. Therefore, the first approach (Eq. 11) was used in this work, i.e. $S_{rel}(t) = S(t) - S_0$.
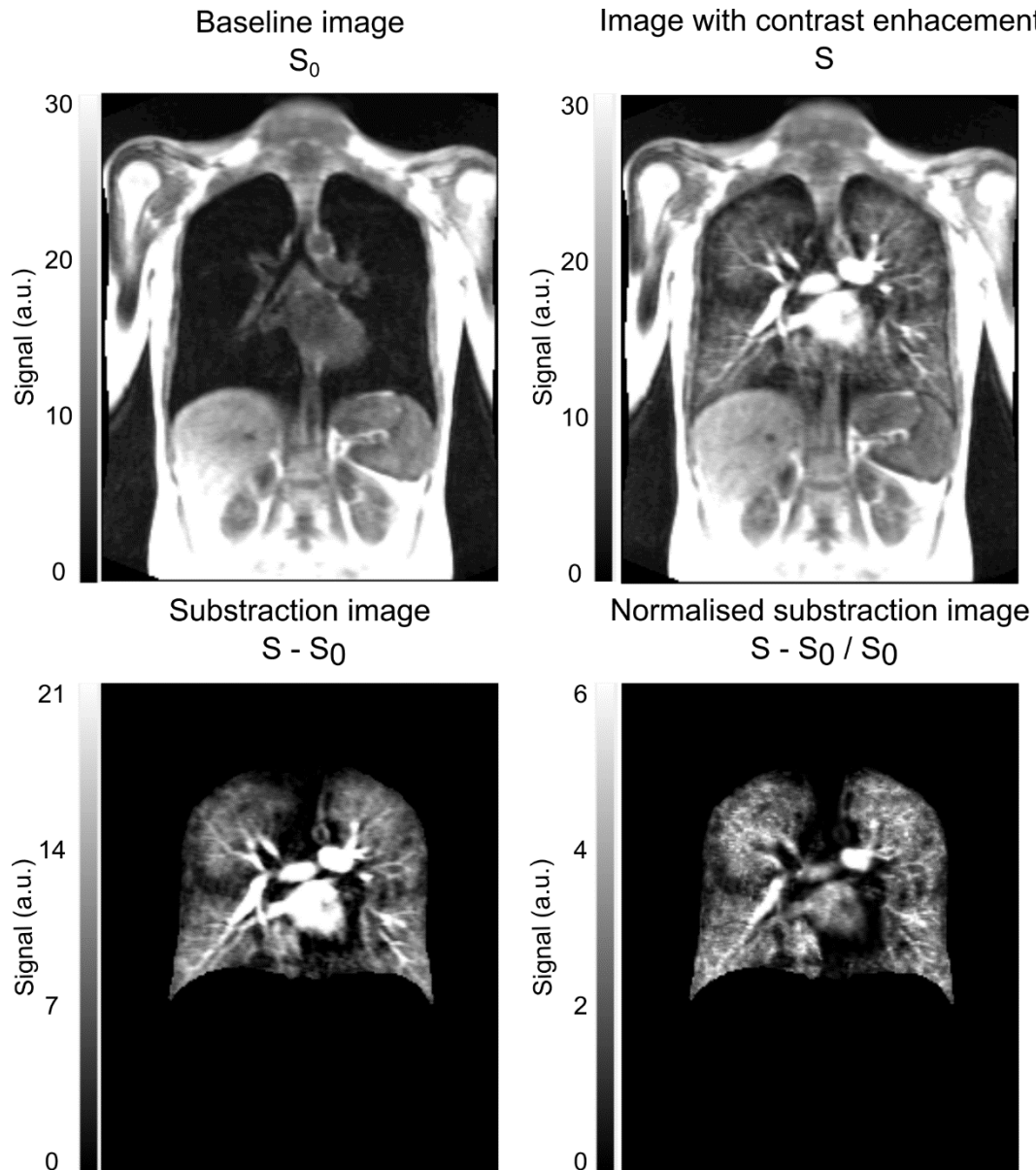
Figure 5: Generation of C(t) maps from $S_{rel}(t)$ maps using two different approaches. Different scaling was applied to the images. The same slice and timepoint from the same DCE-MRI dataset from one patient were chosen to visualise the differences in the contrast enhancements.

S_0 was calculated by averaging the signal of the first two time points, as suggested by Bell et al. (Bell et al. 2015). The baseline signal S_0 was not calculated solely from the first time point of the DCE-MRI pulse sequence, as it has a lower image quality compared to the subsequent time points due to the key-hole technique. S_0 must be acquired before the CA arrives in the main pulmonary artery where the AIF was measured. In case of mistiming of the CA- bolus

application, i.e. in case the CA was applied too early, only the first time point was used to calculate S_0. The mistiming of the CA was monitored by the gradient of the signal change in the main pulmonary artery in every time point (how the main pulmonary artery was found, and the ROI was created is described in section 2.4.3). If the gradient in the second time step exceeded 15% of the maximum gradient, only the first time point was used for the S_0 calculation. Concentration maps (C(t) maps) were approximated by calculating $S_{rel}(t)$ in every voxel.

Lack of linearity between CA concentration and MR signal intensity occurs with the used CA protocols only in areas with a high proportion of CA per voxel, such as in the large pulmonary arteries, as described in section 1.3.8. Thus, a non-linear relationship can be problematic in the main pulmonary artery, in which the AIF for the perfusion quantification was determined (Puderbach et al. 2008). Moreover, the non-linearity problem should not affect the pulmonary vascular bed, since CA was highly dispersed over the lung volume, as opposed to the central arteries. Two approaches were introduced to correct for non-linearities in the CA-concentration to signal intensity relation in the AIF. On the one hand, the so-called "dual-bolus approach" was introduced using a CA pre-bolus with a lower CA concentration to remain in the linear range, followed by a CA bolus with higher concentration. The concentration-time course for the AIF was constructed from the data acquired during the "pre-bolus" image acquisition (Risse et al. 2006). On the other hand, a method was introduced by Neeb et al. correcting the signal intensity of the AIF with a calibration curve, which requires detailed information of the used pulse sequence parameters (Neeb et al. 2009).

In this work, only single bolus data and no detailed information of relaxation times were available (Ingrisch et al. 2010; Risse et al. 2006). The correction proposed by Neeb et al. using

a calibration curve has the benefit that no detailed knowledge about the relaxation times (T1 and T2*) are needed, but when applying Neeb´s calibration method, Bell et al. did not find a significant difference for the PBF quantification for a spoiled GRE sequence and Gd-DTPA (Bell et al. 2015; Neeb et al. 2009). It was speculated, that the use of DCE-MRI pulse sequences with a higher flip angle and short TR/TE, like in the present work, extent the area in which the signal and the CA concentration have a linear relationship (Bell et al. 2015). The work by Puderbach et al. clearly depicted a linear relationship in the range between ~0-4mM CA concentration with an MR signal S/S_0 in the range of ~0-40 (Puderbach et al. 2008). The study used a spoiled GRE sequence with a flip angle similar to the DCE-MRI pulse sequence used in this work. Furthermore, the relaxivity of the Gd-DTPA (longitudinal relaxivity in human blood plasma (37°C) at 1.5T: r1=3.9 ± 0.2l/mmol/s) used by Puderbach et al. is similar to the relaxivity of Gd-BT-DO3A (longitudinal relaxivity in human blood plasma (37°C) at 1.5T: r1=4.7 ± 0.2l/mmol/s), which was used in this work (Pintaske et al. 2006). The measured MR signals in the main pulmonary artery (AIF ROIs) in this work, or more specifically the maximum signal divided through the baseline signal S_{max}/S_0, did never exceed the value of approximately 20, i.e. was distinctly lower than the linearity limit found by Puderbach et al. Based on the findings from literature and measured data, no correction was performed in this work as it was concluded that a linear relationship between MR signal and CA concentration can be approximated.

2.3.2 Impulse response function and regularisation

The fundamental function for the quantification of pulmonary perfusion is the IRF, which were calculated by deconvolving the AIF with each voxel of the time-resolved C(t) maps (Sourbron et al. 2006).

$$IRF(t) = C(t) * C_a(t)$$

where $*$ denotes mathematical deconvolution.

AIF was measured as $C_a(t)$ in the main pulmonary artery and $C(t)$ was directly measured in the lung (tissue compartment) and not at the venous outflow, which enables a regional perfusion assessment for every image voxel. Figure 6 shows the assessment of $C_a(t)$ and $C(t)$ in the tissue and the mathematical relationship to the IRF.
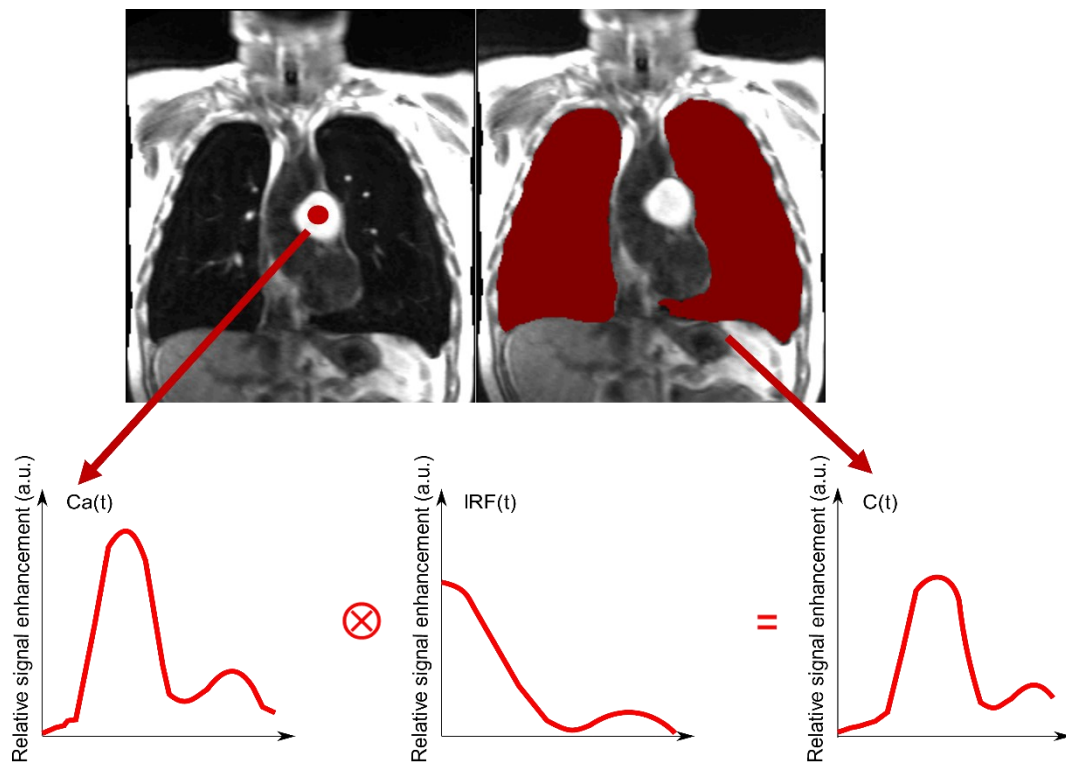
Figure 6: Measurement of the AIF in the main pulmonary artery and measurement of C(t) in the lung parenchyma (respective ROIs are marked in red). The convolution of the resulting $C_a(t)$ (AIF) with IRF(t) to compute C(t) is depicted in the lower part of the figure.

As the algebraic deconvolution is an ill-posed problem, the calculation of IRF requires regularisation. Common solutions include regularisation methods for singular value decomposition (SVD). Before SVD can be applied, the deconvolution equation were first

converted into a discrete form, which is possible because $C(t)$ and $C_a(t)$ can only be measured

at n discrete time points, due to the discrete sampling of the values in time-resolved MRI.

Discretisation:

$$C(t) = \int_0^t C_a(t) \cdot IRF(t - \tau)d\tau \approx \cdot \Delta t \sum_{i=0}^{j} C_a(t_i) \cdot IRF(t_j - t_i) \qquad 14$$

Or:

$$C(t) \approx \Delta t \sum_{i=0}^{j} IRF(\text{t}) \cdot C_a(t_j - t_i) \qquad 15$$

Or:

$$\begin{pmatrix} C(t_1) \\ C(t_2) \\ \dots \\ C(t_n) \end{pmatrix} \approx \Delta t \begin{pmatrix} C_a(t_1) & 0 & \cdots & 0 \\ C_a(t_2) & C_a(t_1) & \cdots & 0 \\ \dots & \dots & \cdots & \dots \\ C_a(t_n) & C_a(t_{n-1}) & \cdots & C_a(t_1) \end{pmatrix} \begin{pmatrix} IRF(t_1) \\ IRF(t_2) \\ \dots \\ IRF(t_n) \end{pmatrix} \qquad 16$$

where Δt=time between the temporal centres of two subsequent images acquired with

DCE-MRI.

The equation can be written as matrix equation, where the elements of $C(t_i)$ were represented

by b, the m×n matrix of $Ca(t_i)$ represented by A and the elements of $IRF(t_i)$ represented by x

with i= 1,2, ...,n:

$$b = A\,x \qquad 17$$

The matrix equation can also be considered as a linear least-squares problem where the minimal

residual is sought.

$$\min_{x} ||A\,x - b||_2 \qquad\qquad 18$$

SVD was used for characterising least-squares problems and to enable the inversion of the ill-conditioned matrix A:

$$A = V\ \Sigma\ U^T \qquad\qquad 19$$

$$\Sigma\ =\ diag(\sigma_1, \sigma_2, \ldots, \sigma_n) \qquad\qquad 20$$

where U and V are orthogonal matrices with the left and right singular vectors of A, U^T is the transposed matrix of U, Σ is a diagonal matrix, σ are the elements of the diagonal matrix Σ and the diagonal elements σ of Σ are the singular values of A.

If rank(A)=k , where k<n to ignore components of the right-hand side, Σ can be inverted to Σ^{-1} and the inverse of A (A^{-1}) can be computed to determine the minimum-norm solution to the least-quare problem (Hansen 1987).

$$\Sigma^{-1}\ =\ diag(\frac{1}{\sigma_1}, \frac{1}{\sigma_{2_1}}, \ldots, \frac{1}{\sigma_k}, 0, \ldots, 0) \qquad\qquad 21$$

$$X = V\,\Sigma^{-1}U^T\,b \qquad\qquad 22$$

Without regularisation, the least-squares problem would produce meaningless results in the presence of noise causing IRF to oscillate. Noise is characterised by small values relative to the signal and is therefore only contained in the smallest singular values. Furthermore, the signal behaviour of CA is systematic, which means that it follows a function that is described by a few strong singular values. As a result, the smallest singular values are only determined by the noise without containing information about the CA signal. Regularisation approaches

set negative singular values and the smallest singular values to 0. The regularisation parameter λ determines the weight of the regularisation with which the regularised inverted matrix A_λ^{-1} can then be formed.

$$\Sigma_\lambda^{-1} = diag(\frac{\sigma_1}{\lambda^2 + \sigma_1{}^2}, \dots, \frac{\sigma_n}{\lambda^2 + \sigma_n{}^2}) \qquad 23$$

$$A_\lambda^{-1} = V\,\Sigma_\lambda^{-1}\,U^T \qquad 24$$

$$X_\lambda = V\,\Sigma_\lambda^{-1}U^T\,B \qquad 25$$

where Σ_λ^{-1} is the regularised and inverted diagonal matrix Σ and X_λ is the regularised solution. With this, the solution depends to a large extent on the values of λ and the solution can be under- or overregularised leading to incorrect values in the IRF (Ravesh et al. 2013; Sourbron et al. 2006).

Various regularisation methods exist for the SVD process to reduce the noise sensitivity. The most common regularisation techniques in bolus tracking MRI are the truncated SVD (tSVD) and SVD with standard form Tikhonov regularisation (SFTR) (Hansen 1987; Ravesh et al. 2013; Sourbron et al. 2004). tSVD with a fix threshold and SFTR SVD combined with L-curve criterion (LCC) was used for the evaluation on the influence of different noise levels to the regularisation approaches (simulated data). For the calculation of IRF from the DCE-MRI data in every voxel (IRF maps) tSVD with a fixed threshold of 20% was used as regularisation method (real study data). tSVD combined with LCC was not evaluated in this work as the combination leads to problems in the regularisation, which can be resolved by combining LCC with SFTR (Hansen 1987; Sourbron et al. 2004).

The regularisation was performed as follows:

1. **tSVD with fix threshold**

   tSVD with a fix threshold cuts off the smallest values of σ, corresponding to a sharp filter. The signal below this threshold was considered as noise (Hansen 1987; Østergaard et al. 1996). A threshold of 15-20% of the maximum values was determined as sufficient in bolus tracking MRI (Østergaard et al. 1996)

2. **SFTR SVD with LCC**

   The basic principle behind SFTR is adding the 2-norm of the solution X as a quadratic constrain multiplied with the regularisation parameter λ to the least square equation:

$$\frac{min}{x}||A\,x - b||_2^2 + \lambda^2||x||_2^2 \qquad\qquad 26$$

   LCC utilise variable thresholds for λ. LCC determines the optimal λ with a compromise between $||A\,x_\lambda - b||_2$ and the solution norm $||x_\lambda||_2$ (Hansen 1998; Sourbron et al. 2004).

2.3.3   Simulation: influence of noise on regularisation

First, the regularisation method used for the deconvolution of the DCE-MRI data and thus for the IRF calculation was selected by simulating the influence of noise on different regularisation approaches. All data were simulated with a sampling rate of 1.5s and a sampling interval of 36s, i.e. t=[0:1.5:36]. The simulations of $C_a(t)$ and $C(t)$ were both based on a gamma-variate function, since this curve delivers a good approximation of the bolus injection scheme (Calamante et al. 2000; Starmer and Clark 1970).

$$C_a(t) = k\,(t-t_0)^\alpha \cdot e^{-\frac{t-t_0}{\beta}} \tag{27}$$

where k is a scaling factor depending on proton density, tissue type, pulse sequence, and contrast agent used, t is the time frame, t_0 is the time till bolus arrival, α is the curve ascending time and β is the curve descending time.

Based on the data published by Calamante et al., k was set to 50, α was set to 3.0s and β was set to 1.5s (Calamante et al. 2000). $C_a(t)$ was converted to a Toeplitz matrix before it was decomposed to V Σ U^T by SVD. For tSVD a threshold of 20% was chosen and the regularised inverse of A was formed as described in section 2.3.2 (Eq. 24). For the inversion and regularisation of $C_a(t)$ by SFTR SVD with LCC, the MATLAB toolbox developed by Christian Hansen was used, which determines the optimal regularisation parameter λ for Eq. 23 (Hansen 2016).

C(t) was simulated by multiplying $C_a(t)$ with the simulated IRF (Eq. 14). IRF was simulated by multiplying PBF with an exponential function defined by the mean transit time (MTT) (Calamante et al. 2000). Since PBF was defined in the simulation, an under- or overestimation of PBF by the different regularisation approaches can be evaluated directly.

$$\text{IRF}(t, MTT) = PBF \cdot e^{\frac{-t}{MTT}} \tag{28}$$

$$C(t) = C_a(t) \cdot PBF \cdot e^{-\frac{t}{MTT}} \tag{29}$$

A PBF of 90ml/min/100ml and a MTT of 3s was chosen for the simulations. As described in section 1.3.9, DCE-MRI data of the lungs are affected by low CNR. Therefore, a CNR range from 2 to 20 with an increment of 2 was simulated for C(t) at maximum with 1000 runs to add randomly generated samples of noise. The noisy C(t) (C(t)[noisy]) was simulated by adding

Rayleigh distributed complex noise n(t) to C(t), which results in a Rice distributed signal at low CNRs (Gudbjartsson and Patz 1995). Complex Rayleigh distributed noise n(t) was generated out of normally distributed numbers.

$$n(t) = \frac{1}{\sqrt{2}} \left(V_n \cdot \sigma_n + i \cdot V_n \cdot \sigma_n \right) = n(t)_{real} + n(t)_{imag} \qquad 30$$

where V_n are normally distributed random variables, i is the imaginary unit, σ_n is the standard deviation of the noise, $n(t)_{real}$ is the real part of Rayleigh distributed noise, and $n(t)_{imag}$ is the imaginary part of Rayleigh distributed noise.

The generated noise was added to C(t), with C(t) containing only real parts.

$$C(t)^{noisy} = \left| \sqrt{(C(t) + n(t)_{real})^2 + (n(t)_{imag})^2} \right| \qquad 31$$

CNR of C(t) was defined as follows:

$$CNR = \frac{\max(C(t))}{\sigma_n} \qquad 32$$

Noisy IRF (IRF^{noisy}) and noisy PBF (PBF^{noisy}) were calculated by:

$$IRF(t)^{noisy} = C(t)^{noisy} \cdot C_a(t)_\lambda^{-1} \qquad 33$$

$$PBF^{noisy} = \max(IRF(t)^{noisy}) \qquad 34$$

where $C_a(t)_\lambda^{-1}$ is the inverted and regularised $C_a(t)$.

The relationship between IRF and PBF is described in section 2.3.4.

2.3.4 Pulmonary blood flow and volume

For the quantification of PBF and PBV, the residue function R(t) must be determined from the IRF (Ostergaard et al. 1996; Østergaard et al. 1996). IRF was defined as the product of PBF and R(t) (Østergaard 2005). With this relationship, Eq. 5 can be written as:

$$C(t) = PBF \cdot C_a(t) \otimes R(t) = PBF \int_0^t C_a(t) \cdot R(t - \tau) \, d\tau \qquad 35$$

R(t) describes the fraction of the CA present in the tissue at time t after the CA has reached the tissue of interest. By the definitions of the indicator dilution theory for intravascular CA, i.e. non-diffusible CA, this results in the following relationship with the IRF:

$$R(t) = 1 - \int_0^t IRF(\tau) \, d\tau \qquad 36$$

where the integral term represents the fraction of the CA that has left the tissue. Further, $[R(t = 0) = 1]$ and $[R(\infty) = 0]$ was defined, which means that all CA is present at time $t = 0$ and R(t) is a positive decreasing function of time with all CA must leave the system (Zierler 1962). With these definitions, PBF can be defined as the initial height of the IRF (Ohno et al. 2004; Sourbron et al. 2006). However, in practice the AIF cannot be measured straight in front of the tissue of interest for pulmonary perfusion quantification with DCE-MRI due to the spatial resolution of the DCE-MRI data in the lungs. Therefore, the AIF ($C_a(t)$) was measured in the main pulmonary artery (pulmonary trunk), which is the spatially nearest point to the lung at which the AIF can be determined for the whole lung. This results in a delay and dispersion of the C(t) compared to $C_a(t)$, which in turn leads to a dispersion of R(t). Therefore, the maximum of R(t) should be used as PBF, as the initial height would result in an underestimation

of PBF (Calamante et al. 1999; Østergaard et al. 1996). The regional amount of intravascular CA, i.e. PBV, was defined as:

$$PBV = \frac{\int_0^\infty C(t)\, dt}{\int_0^\infty C_a(t)\, dt}$$

37

Alternatively, the areas under the two CA concentration curves can be replaced with the area under the IRF curve:

$$PBV = \int_0^\infty IRF(t)\, dt = \int_0^\infty PBF \cdot R(t)\, dt$$

38

$C_a(t)$ and $C(t)$ are both measured in ml and Δt in s. Since PBF is expressed in $\frac{ml}{100ml \cdot min}$ and PBV in $\frac{ml}{100ml}$, by convention, PBF was multiplied by 6000 and PBV was multiplied by 100. PBF and PBV were calculated from IRF maps and summarised for the whole lung or individual lobes by arithmetically averaging the PBF/PBV values of the voxels.

2.3.5   Perfusion defects in percent

QDP was calculated in percent representing the extent of perfusion abnormalities relative to the lung volume, with a theoretical range between 0% and 100%. QDP was quantified from IRF maps at the time point of maximum contrast enhancement (IRF_max maps) to take advantage of the mathematical models of indicator dilution theory. The mean of all values in the lungs from the IRF maps was calculated separately for each time point and the time point with the maximum mean value was determined as the time point of maximum contrast enhancement. The first time point of the IRF_max maps was excluded due to the large number of artifacts

present. The IRF_{max} maps were median filtered (square 5x5 neighbourhood within each slice) to compensate for noise and remove isolated voxels while preserving edges. The strong median filter further increases the contrast between poorly perfused and well perfused areas, which facilitates the automatic detection of perfusion defects and decrease the influence of partial volume effects. All voxels outside of the lungs were set to zero.

In the COSYCONET study, QDP was developed and thus calculated using different approaches. All QDP quantification methods used in the COSYCONET study were optimised based on the data. The best results were observed for Otsu´s method, k-means clustering and 80th percentile-threshold. In the reproducibility study, only QDP based on Otsu´s method was further evaluated, as it showed the best results in the COSYCONET study. All perfusion quantification approaches were performed using the entire 3D IRF_{max} maps and not individual slices.

1. **Otsu´s method**

   Otsu's method was employed to determine two thresholds from an intensity histogram, which contains the signal values of all voxels within the segmented lung of the IRF_{max} maps and zeros in the same amount as the lung size (Otsu 1979). Two thresholds were used to separate the lungs in three clusters, which should represent poorly perfused lung voxels, well perfused lung voxels, and blood vessels. The identified poorly perfused lung voxels were used to calculate QDP. Otsu´s method is sensitive to variations in the ratio between object and background (Kittler and Illingworth 1985; Lee et al. 1990). Therefore, the background size was adjusted to the size of the object, i.e. the lung mask.

2. k-means clustering

k-means clustering was applied to the entire IRF_{max} maps, including the zeroed background. k-means clustering was performed to separate the voxel intensities into three clusters, which should represent poorly perfused lung voxels, well perfused lung voxels, and blood vessels. The identified poorly perfused lung voxels were used to calculate QDP.

3. 80th percentile threshold

The 80th percentile of the IRF_{max} maps' intensities within the lung mask was multiplied with a factor of 0.5 to separate the lung voxels into two clusters. The threshold should represent the boundary between well and poorly perfused lung voxels (Heimann et al. 2012). The voxels classified as poorly perfused contributed to QDP.

An overview about the calculation of QDP with the three different methods is outlined in Figure 7. The resulting QDP maps were again median filtered (square 7x7 neighbourhood within each slice) to compensate for calculation errors before QDP was calculated from the maps.
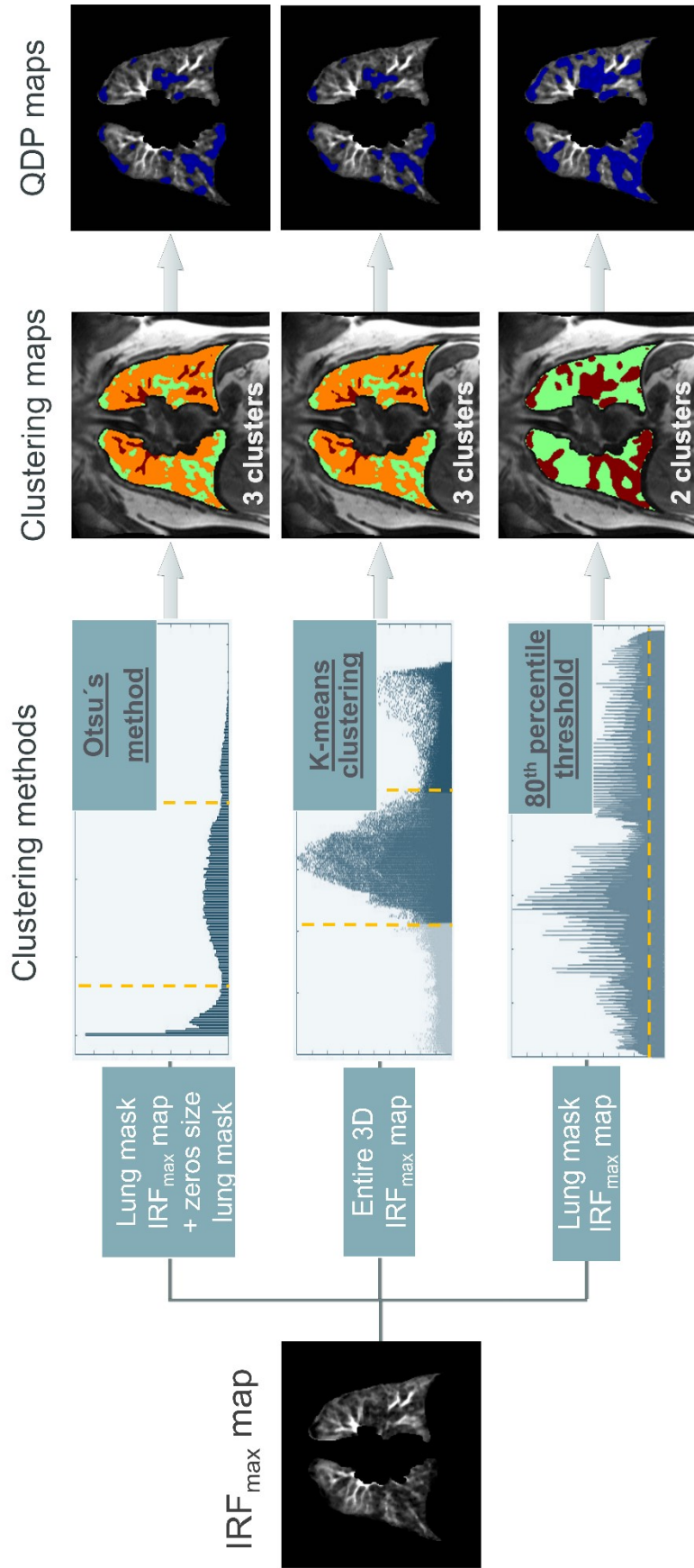
Figure 7: Flowchart describing the different approaches to calculate QDP maps (Schiwek et al. 2021) '*Reproduced with permission from Springer Nature*'.

The patient's supine position in the MRI scanner introduces a physiological perfusion gradient from anterior to posterior created by gravity (Hueper et al. 2013). As a result, the signal intensity increases from anterior to posterior, which can lead to an overestimation of perfusion defects anteriorly and to an underestimation posteriorly when clustering algorithms are used. The effect of gravity can be compensated by adapting the threshold P identified by the clustering algorithm per slice. Heimann et al. proposed to adapt the threshold P for each slice by adding the slope of intensity increase c (linear regression) multiplied with the slice number s (centre slice s=0) (Heimann et al. 2012).

$$T(s) = (P + s \cdot c)/2 \qquad\qquad 39$$

where T(s) is the adapted threshold for each slice.

In the COSYCONET study, no correction of the perfusion gradient from anterior to posterior was implemented to enable better comparability of the methods. In the reproducibility study, a correction of the perfusion gradient from anterior to posterior was implemented, by adapting the threshold determined by Otsu´s method for the whole 3D image per slice position, as previous published by Heimann et al. (Heimann et al. 2012). The correction coefficient c was calculated by using a first-degree polynomial fit to the course of the mean lung signal intensities of the slices.

For the comparison per lobe between QDP and the MRI perfusion score, QDP was converted into discrete values at lobe level to allow for a direct comparison against the MRI perfusion score (Bauman et al. 2013; Eichinger et al. 2012) (Table 4).

Table 4: Conversion of QDP into discrete values for the comparison with the visual MRI perfusion score per lobe (Schiwek et al. 2021) '*Reproduced with permission from Springer Nature*'.

Discrete value	MRI perfusion score	QDP
0	Normal	<7.5 %
1	<50 %	≥7.5 % to <50 %
2	≥50 %	≥50 %

The discrete values 0, 1 or 2 were assigned per lobe to achieve comparability of the visual MRI perfusion score with QDP. The threshold of <7.5% was defined for no perfusion defects in QDP to compensate errors caused by noise and image artifacts, as described previously (Bauman et al. 2013).

2.4   Automatic segmentation

The lungs were automatically segmented from the VIBE images, approximately divided into lung lobes, and registered to DCE-MRI TWIST images, as published previously (Kohlmann et al. 2015). Furthermore, the ROI for the AIF measurement was automatically identified and respiratory artifacts in the region of the diaphragm, which are caused when the patient starts to breath shallowly during the DCE-MRI acquisition, were removed via cross-correlation analysis. All resulting segmentations and registrations were reviewed individually. In the following, several image and curve processing techniques are used several times:

1. An image processing technique called "labelling" was used to identify, and number connected components (groups of voxels). 2D and 3D connectivities can be defined. For example, a connectivity of 4 in 2D means that voxels are connected if their edges or corners touch, i.e. two voxels in one slice are part of the same group if they are connected along the horizontal, vertical, or diagonal direction (Haralick and Shapiro 1992).

2. A technique to smoothen data was used to remove noise from data curves before the data were analysed to find peaks and minima or maxima. A smoothing method using weighted linear least squares local regression and a 2nd degree polynomial model with

a span of 8 was used. The span in this context was defined as the number of data points used to calculate the smoothed value.

3. An image processing technique to fill holes in segmentation masks based on morphological reconstruction was used, where a hole was defined as pixels/voxels that cannot be reached by filling in the background from the edge.

4. Morphological image processing techniques to erode or dilate boundaries of segmentation masks were used on binary images using structuring element, such as a disc for processes in 2D. Elements are eroded or dilated at their boundaries if the structuring element fits completely at this point (Haralick and Shapiro 1992).

2.4.1 Lung segmentation

The lungs were segmented from the VIBE images by region growing algorithm including seed point identification. The segmentation of the lungs was mainly carried out on VIBE images in coronal orientation, except for the segmentation of the trachea, which was carried out on VIBE images in transverse orientation. The segmentation was completely self-programmed based on the published principles of Kohlmann et al. Several modifications were made to the approach. For example, a watershed transformation was used to ensure a clear separation of right and left lung, the histogram thresholds were adapted, and the trachea was only excluded until the bifurcation (Kohlmann et al. 2015).

1. **Seed point identification in each lung:**

   The seed points are the starting points for every region growing algorithm. The seed points were identified in the left and right lung at the central slice. First the entire chest was segmented by excluding all voxels with an intensity below the first peak (threshold) of the smoothed intensity histogram of the whole 3D image. As this also excluded

voxels within the lungs, holes within the resulting chest mask were filled. A second histogram, which only included the intensities of the voxels from the chest in the centre slice, was used to determine the threshold for a coarse lung segmentation in 2D in the central slice. Only voxels with an intensity below the first peak (threshold) of the smoothed intensity histogram were classified as lung tissue in the central slice. Watershed transformation was used in case both lungs were connected on the central slice. The Euclidean distance to the edges of the shape was calculated separately for both lungs and the positions of the maximum distance were determined as positions for the seed points in order to place the seed points in the centre of the lungs (Figure 8).
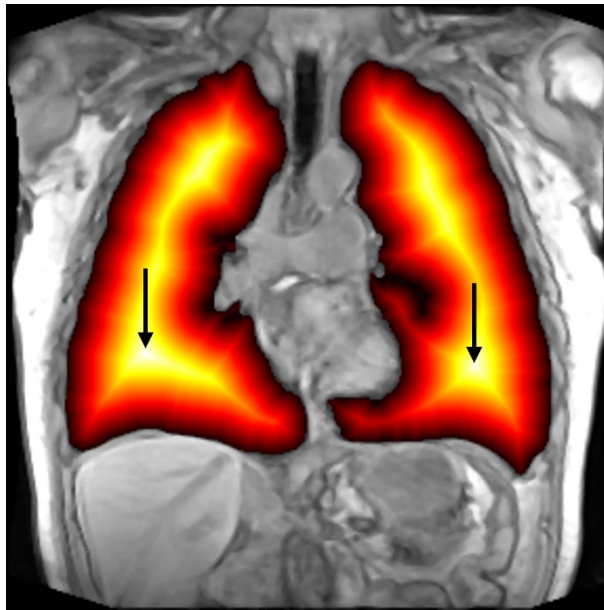
Figure 8: Representative Euclidean distance map for the right and left lung with the VIBE image superimposed. Seed points are marked by black arrows. The colour scale of the Euclidean mask ranges from red to light yellow, with red denoting a small distance from the edges and light-yellow denoting a far distance from the edges of the lungs.

2. Exclusion of the trachea:

The trachea was segmented until the bifurcation into the two primary bronchi from VIBE images in transverse orientation. First, the entire chest was segmented using histogram analysis on the median image, analogous to chest segmentation for the seed point identification (described in the paragraph above). Second, all connected structures were labelled separately for each slice (connectivity of 2 in 2D) (Figure 9). The start slice for the trachea label identification was determined to be the first slice in which the lungs appear, since the trachea is clearly visible and separated from other structures in this slice. The size of the chest mask increases rapidly when the lung begins to appear in the slices. The start slice could thus be identified by using a polynomial curve fit (1 degree) of the sum of all voxels within a slice, to determine the slice with the greatest slope in the curve fit. The labels in the start slice were compared with the labels in the subsequent slices. The trachea was identified by comparing the labels in the following slices with the labels in the start slice. The trachea does not change substantially in size across slices, but its position changes slightly from slice to slice. Therefore, labels that belong to the trachea were identified if the labels in the following slices overlap, the size of the labels were not smaller than 30 nor bigger than 300 voxels points, and the size of the label did not change by more than 40%. The segmented trachea was transformed to the coordinate system of the coronal VIBE images after the segmentation by linear transformation.
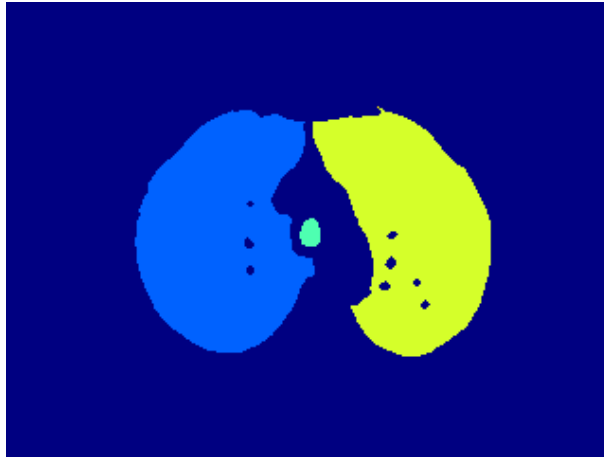
Figure 9: Labelled connected structures in one slice of a VIBE image in transverse orientation. Each label is presented in a different colour, with the trachea in light green.

3. Region growing and separation of the lungs:

Starting with the seed points, the 3D region growing algorithm included all neighbouring voxels of the inverted median filtered 3D image by a flood-fill operation (connectivity of 6 in 3D). The flood-fill operation is a voxel-based method, recognising all dark areas (here: lung parenchyma), which are surrounded by lighter areas (here: thorax wall) (Soille 1999). The signal was higher in the chest wall due to the higher amount of tissue (higher proton density) compared to the lung parenchyma. In case the right and left lung were connected a watershed transformation was used to separate both lungs. As watershed transformation tends to over-segment images, shallow minima representing irregularities in the image and noise were removed and the number of segmented objects of interest were defined as two: one for the right lung and one for the left lung. Regional minima are defined as connected components of pixels/voxels. All minima with a depth less than H, where H was defined as the maximum of the Euclidian distance to the edges of the shape, were suppressed using a transformation with a connectivity of 26 in 3D. From the resulting segmented lung mask (Figure 10), the previously segmented trachea mask was then excluded, followed by a 3D

morphological erosion applied to the segmented lung mask to avoid partial volume effects at the lung borders (Heimann et al. 2012).

Figure 10: Representative segmented lung (red) depicted on the central slice.

An approximate division of each lung into the **lobes** was performed, as depicted in Figure 11. First, the lungs were divided into twelve regions of equal volume (six per lung) (Kohlmann et al. 2015). Second, the six regions of equal size per lung were combined to approximate the three lobes per lung as follows: upper lobe=both upper regions, middle lobe or lingula=ventral middle region, and lower lobe=dorsal middle region and both lower regions.
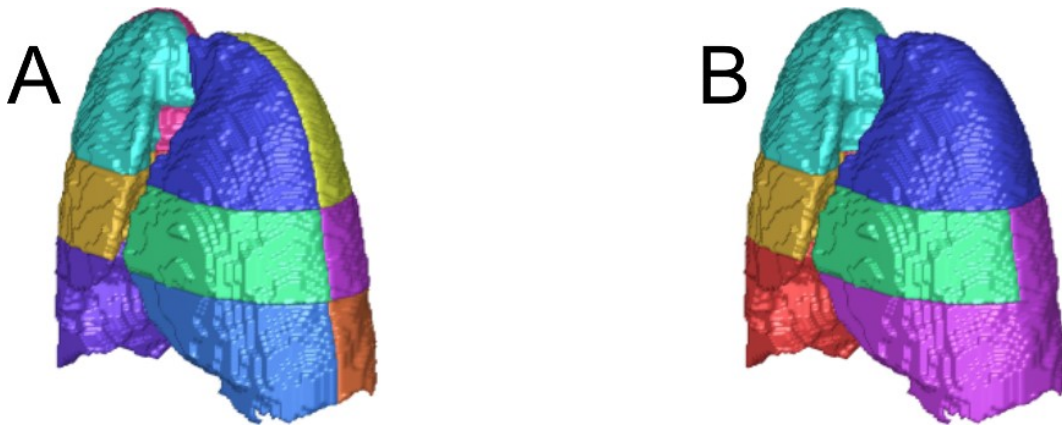
Figure 11: Color-coded 3D visualisation of the automatic lung partitioning process. A) 12 lung regions of equal size and B) 6 approximated lobes (Schiwek et al. 2021) '*Reproduced with permission from Springer Nature*'.

2.4.2   Lung registration

After the segmentation of the lungs from the morphological data the segmented lung mask were transferred to the DCE-MRI data by image registration. As the morphological and the DCE-MRI data are acquired in succession and during different breath holds the patient position and the inspiratory level may have changed, which creates the need for deformable (non-rigid) image registration. Non-rigid demon registration algorithms, based on diffusion models, were used in this work. The registration was performed on the entire 3D data, but the time-resolution of the DCE-MRI data was removed by calculating the mean of all time points. The registration was considered multimodal, as the morphological data and the DCE-MRI data has substantial differences in the T1-weighting and with this in the image contrast, (Kohlmann et al. 2015).

The MATLAB toolbox "multimodality non-rigid demon algorithm image registration" provided by Dirk-Jan Kroon was used for the registration and modality transformation. The demon registration was introduced by Thirion and extended by Cachier et al. and Wang et al. (Cachier et al. 1999; Thirion 1998; Wang et al. 2005). The concept behind the demon registration can be explained by an analogy to a thermodynamic concept (analogy to Maxwell's

demons). The object boundaries in one image (static image J) can be seen as semi-permeable membrane, which allows the other image (moving image I) diffuse through these interfaces. The local "demons" apply invisible "forces" to every voxel to push the voxels of I until they match with the static image J. For grey-scale image-based registration, the optical flow equation can be used to estimate the demon forces

$$\vec{u} = \frac{(m - s) \cdot \vec{\nabla} s}{\left|\vec{\nabla} s\right|^2 + (m - s)^2} \qquad 40$$

where $\vec{u}$ is the estimated displacement, m is the intensity of the moving image, s is the intensity of the static image, and $\vec{\nabla} s$ is the gradient of the static image (a measure of the relationship between neighbouring voxels). The equation was solved iteratively by a Broyden–Fletcher–Goldfarb–Shanno optimiser in the toolbox used (Kroon 2010; Kroon and Slump 2009; Vercauteren et al. 2009). The method was extended by adding further demons' forces. The additional constraint assumes that the diffusion is bi-directional, so that the demon produces also a force allowing J to diffuse into I (Wang et al. 2005). With this, the algorithm requires fewer iterations until it converges. To further speed up the iterative solution of the equation, Cachier et al. introduced a normalisation factor α, which modifies the step size depending on the extent of deformation and the convergence state of the iterative process (Cachier et al. 1999).

The modality transformation of image I into I_T aligned the different tissue contrasts between the morphological image (moving image I) and the DCE-MRI image (static image J) by using a mutual histogram H (I, J) to determine the grey value for each voxel in image J that most frequently overlaps with the voxel grey value in image I (Kroon and Slump 2009)

$$I_T(x) = argmax_j(H(|I(x)N|, |jN|))$$

where x is the voxel location.

During the transformation and registration, a scale space approach can speed up the process and avoid local minima by, first, limiting the spatial resolution and then gradually increasing the spatial resolution of the image (Kohlmann et al. 2015; Kroon and Slump 2009).

2.4.3 Main pulmonary artery segmentation

The AIF, needed for the perfusion quantification based on the indicator dilution theory, was determined in the main pulmonary artery (pulmonary trunk) shortly before the bifurcation into right and left pulmonary artery. The AIF was determined from C(t) maps to measure the concentration time course $C_a(t)$ and the ROI for the AIF was automatically determined to limit human interaction.

The ROI for the AIF measurement was identified by several image processing steps. These steps were developed based on the publication by Kohlmann et al., but several steps were changed or further developed (Kohlmann et al. 2011):

1. Target area was restricted to the heart:

   Since the lungs were already segmented and the heart is located between the two lungs, a vertical cylinder centred between the lungs was defined.

2. Labelling of connected components:

   A maximum intensity projection (MIP) in 3D of the target area was generated by selecting the maximum intensity of each voxel over time. The heart and pulmonary arteries, i.e. the voxels of interest, have a high intensity in the MIP due to the passage

of the CA through these structures. Therefore, all voxels with a signal intensity within the 95th percentile of the MIP were included into further analysis. All remaining voxels are labelled in 3D to identify the two biggest remaining labels, which can be assumed to be the labels of the right heart together with the pulmonary artery and the label of the left heart.

3. Identification of the right heart and main pulmonary artery:

   All small labels were removed and the centroid of the signal intensity curve over time was calculated for every voxel, resulting in a 3D centroid map. The label of the right heart and the pulmonary artery was discerned by using Otsu's method on the 3D centroid map. Since the CA flows first through the right heart and pulmonary arteries, before it passes through the lungs and then through the left heart, the centroid values in the right and left heart are substantial different.

4. Slice and main pulmonary artery identification:

   To identify the appropriate position for the ROI in the main pulmonary artery, the remaining voxels of the right heart and pulmonary artery were labelled on each image slice separately to identify connected structures on individual slices. The correct label was identified using the following assumptions:

   a. The label is not connected to the edge of the image.

   b. The label is circular with a circularity above 0.6.

   c. The labels on the adjacent slices in the same position has also a circularity above 0.6 to ensure that the algorithm stops when the main pulmonary artery split into the right and left pulmonary artery.

The label two slices before the bifurcation was determined as AIF ROI. The identified label was scaled down with an erode algorithm to remove possible influence of vessel walls. If the AIF ROI detection failed, the pipeline allowed ROIs to be drawn manually.

2.4.4 Respiratory motion correction

In this work, only artifacts from shallow respiratory motion were automatically compensated. Normal to heavy breathing during the CA passage through the lungs led to exclusion of the entire data set. Minor respiratory motion artifacts, usually occurring near the diaphragm, are caused when patients cannot hold their breath for the whole acquisition and resume to breath shallowly. The concentration time courses and concentration values in voxels affected by respiratory motion was altered, as depicted in Figure 12, leading to false values in the perfusion quantification.
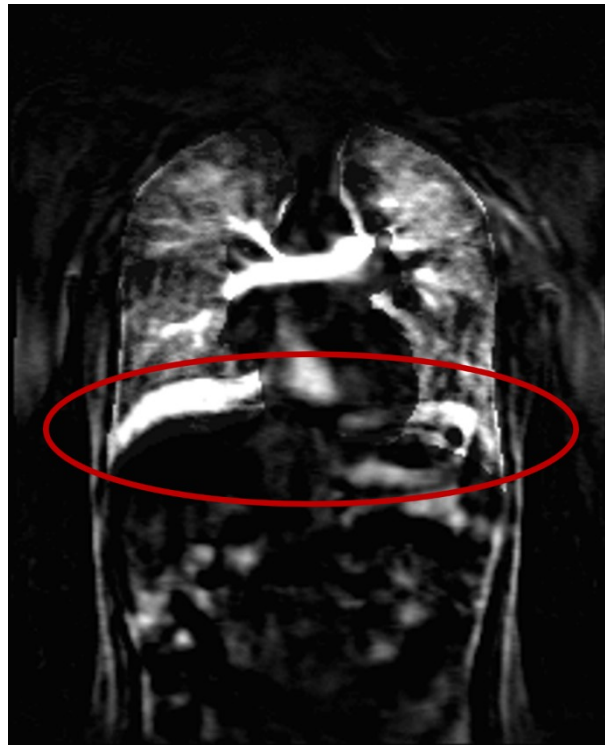
Figure 12: High values in the C(t) map in the area of the diaphragm (red circle) caused by respiratory motion.

In affected voxels, the concentration time course has a different shape compared to the AIF, and/or the signal maximum occurs with a large delay (long lag-time) compared to the signal maximum of the AIF. Therefore, the identification of voxels affected by shallow respiratory

motion was performed using normalised cross-correlation (NCC) analysis, as cross-correlation is a measure of similarity of two curves. NCC was calculated by:

$$NCC = \frac{1}{N} \cdot \frac{\sum_{i=0}^{N}(x_i - \bar{x})\,(y_i - \bar{y})}{\sqrt{[\sum_{i=0}^{N}(x_i - \bar{x})^2]\,[\sum_{i=0}^{N}(y_i - \bar{y})^2]}} \qquad 42$$

where N is the number of time points, x is the discrete AIF (reference function), y is the discrete signal of every voxel within the segmented lungs (the signals of interest) and with $-1 \leq NCC \leq 1$ (+1 for perfect positive correlation, -1 for perfect negative correlation and 0 for no correlation).

The method is based on the same principles as used for suppressing the pulmonary vasculature from DCE-MRI data, but with other conditions (Risse et al. 2009). NCC was calculated for the whole time period to evaluate curve similarity and time-shift together, as well as for each time point to evaluate curve similarity and time-shift separately. Voxels with low NCC coefficients and/or a late correlation maximum, were considered as corrupted by respiratory motion and thus excluded. In addition, since respiratory motion causes calculation errors leading to extremely high PBV values, voxels with high PBV values above 200ml/100ml in the lungs were excluded. PBV values over 100ml/100ml are physiologically not possible as they would represent a volume containing more than 100% blood. However, taking into account the given data quality of the DCE-MRI data, the PBV threshold was set to 200ml/100ml to introduce a tolerance and prevent misclassification. After the exclusion of voxels, holes within the lung segmentation mask were closed automatically using morphological reconstruction (Soille 1999). As a result, only voxels affected by respiratory motion at the border of the segmentation mask were removed, which includes the diaphragm area as depicted in Figure 12.

2.5   Visual MRI assessment

All MRI examinations were assessed by experienced board-certified readers (one reader per study) using a previously validated chest MRI score (Eichinger et al. 2012; Bertram J. Jobst et al. 2015; Stahl et al. 2017; Wielpütz et al. 2018). From this morpho-functional scoring system, the MRI perfusion score was used, which scored the extent of perfusion abnormalities for each lobe as 0 (no abnormality), 1 (<50% of the lobe involved), or 2 (≥50% of the lobe involved). The scores per lobe can be summed up for the whole lung, resulting in a maximum range between zero and twelve. The scoring of perfusion abnormalities was performed using post-processed DCE-MRI datasets. For this purpose, the baseline timepoint without contrast was subtracted from the timepoint with maximal contrast enhancement in the lung parenchyma, resulting in a single 3D image dataset displaying the maximum parenchymal contrast enhancement. In the reproducibility study, the images from both visits were compared side-by-side to identify changes.

2.6   Quantitative CT

In the COSYCONET study, all subjects underwent standardised phantom-controlled (Catphan600) same-day non-enhanced low-dose CT (Somatom 64, Siemens Healthineers, Forchheim, Germany) with two paired scans in inspiratory and expiratory breath-hold at 120kV and 35mAs. CT data were reconstructed at 1.0mm slice thickness with 0.5mm interval using a soft filtered back-projection convolution kernel (B30f). CT data were post-processed, segmented and analysed using the in-house software YACTA (version 2.8.7) (Konietzke et al. 2020) for parametric response mapping (PRM) (Galbán et al. 2012). In detail, PRM classified the lung in normal PRM_{Normal}, emphysematous PRM_{Emph}, or functional small airways disease PRM_{fSAD} (Galbán et al. 2012). PRM was calculated in percent relative to the lung volume. $PRM_{Abnormal}$ was computed to describe the proportion of non-normal lung tissue as:

$$PRM_{Abnormal} = PRM_{Emph} + PRM_{fSAD} \qquad\qquad 43$$

2.7　Pulmonary function testing

In both studies, PFT (MasterScreen Body, E. Jaeger, Hoechberg, Germany) was performed according to the American Thoracic Society and European Respiratory Society recommendations (Graham et al. 2019). In the COSYCONET study, FEV1/FVC (Tiffeneau-Pinelli index), which is also used to diagnose COPD, and FEV1% predicted were used as PFT parameters. In the reproducibility study, FEV1% predicted was used from PFT as patients with COPD and CF were included in this study. In accordance to the guidelines, PFT was conducted with the subject in a seated position and the best of three efforts were used (with a maximum of eight attempts), which was defined as the highest FEV1 and the highest FVC each obtained on any of the three blows. In both studies, the post-bronchodilator PFT values are given for COPD patients. For CF patients, only pre-bronchodilator PFT values are available as per standard of care.

2.8　Statistical analyses

Statistical analyses were performed using R (R 3.3.2 Foundation for Statistical Computing). Data are presented as mean ± SD. Bland-Altman analysis (including Limits of Agreement (LoA)), linear regression, Spearman correlation, Cohen's kappa, percentage agreement, Wilcoxon signed-rank test, Pearson and Filon's z, minimal important difference (MID) based on standard error of measurement from repeated measures analysis of variance (rANOVA), and scatterplots were used. A p-value<0.05 was considered statistically significant. The correlation coefficients were rated as suggested by Karlik for radiological features: 0.0-0.2 as very weak, 0.2-0.4 as weak, 0.4-0.7 as moderate, 0.7-0.9 as strong, and 0.9-1.0 as very strong (Karlik 2003).The Kruskal-Wallis test was used for comparison between CF and COPD groups.

Wilcoxon signed-rank test were used for intra-group comparisons. Due to different ranges of values the LoA were related to the observed median and correlation analyses were performed. Correlation coefficients were compared statistically with the R-package "cocur" (Diedenhofen and Musch 2015) and the p-values from Pearson and Filon's z were used (Pearson and Filon 1898). The correlation coefficient comparison was performed using a one-tailed test (higher or lower comparison). The absolute values of the correlation coefficients were used to not take the influence of different algebraic signs of the correlations into consideration.

3 RESULTS

3.1 Simulation: influence of noise on regularisation

The influence of noise on regularisation approaches were simulated by analysing the resulting

PBF values (start parameters were: PBF=90ml/min/100ml, MTT=3s, and CNR between 2 and

20). On the one hand, PBF was stronger underestimated by tSVD with fixed threshold at higher

CNR (e.g. 20) compared to SFTR SVD with LCC as shown in Figure 13. On the other hand,

the variability of PBF at higher CNR was smaller for tSVD with fixed threshold compared to

SFTR SVD with LLC. Furthermore, PBF values were skewed towards lower values with lower

CNRs for SFTR SVD with LCC. For tSVD with fixed threshold, the variability in the frequency

of observed PBF values increased at lower CNR.
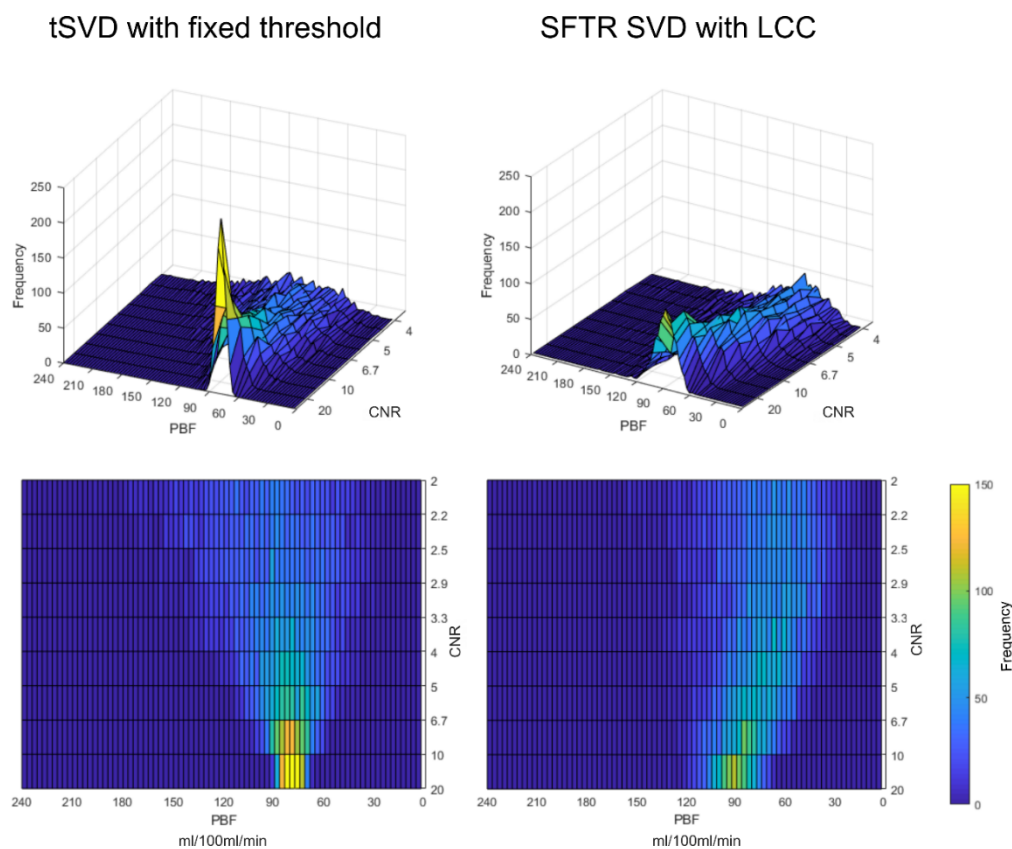
Figure 13: Surface plot visualising the influence of noise on PBF depending for tSVD with a fix threshold of 20% and SFTR SVD with LCC. Frequency is colour coded ascending from blue to yellow.

3.2 COSYCONET study

Figure 14 depicts representative DCE-MRI and CT images of a 51-year-old female patient from the COSYCONET study with COPD GOLD2 with FEV1%=53.26%, FEV1/FVC=0.53, and an MRI perfusion score of 10 with corresponding color-coded QDP, PBF, PBV and PRM maps.
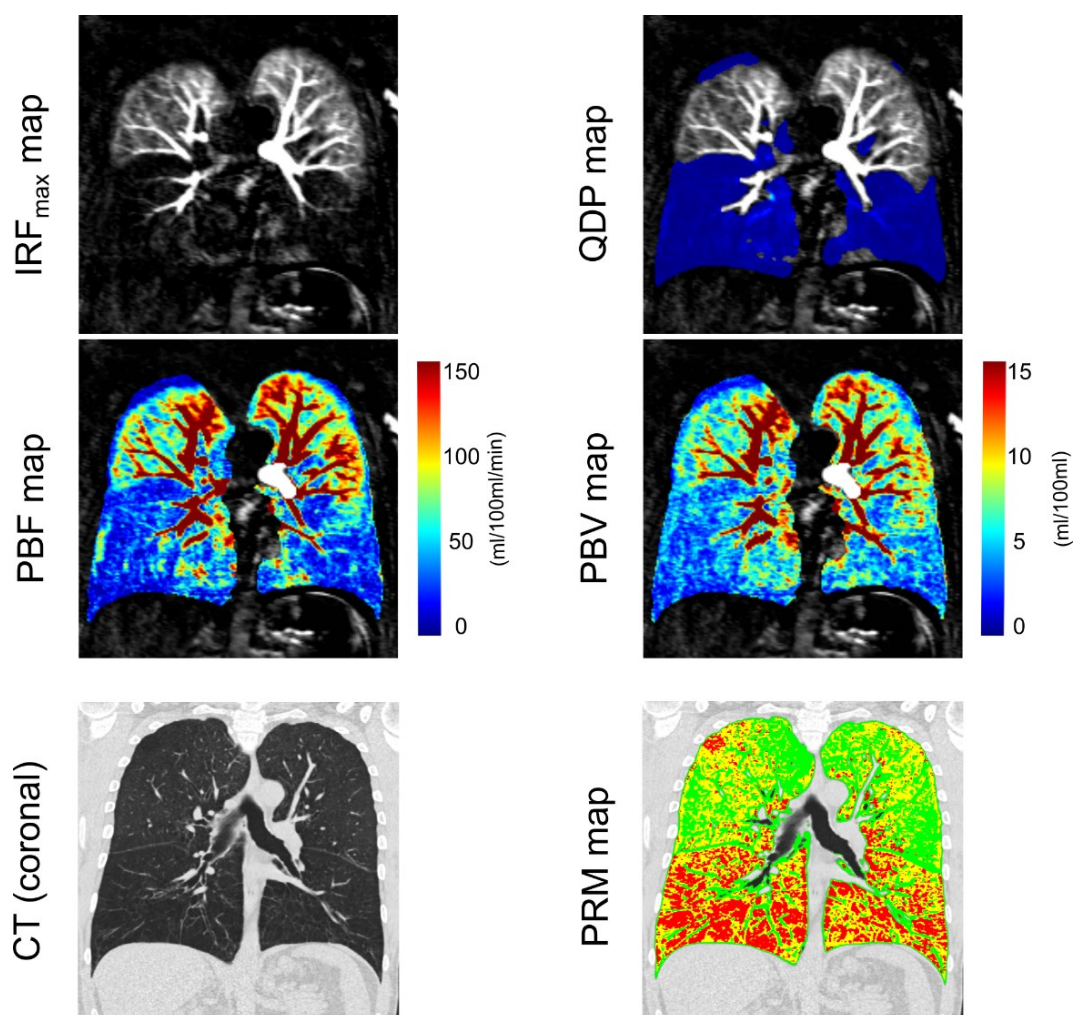
Figure 14: Coronal IRF$_{max}$ map, corresponding QDP map (defects highlighted in blue), PBF map and PBV map from a representative COPD patient from the COSYCONET study. Coronal CT images and PRM maps of the same COPD patient is given in the bottom row. PRM classification of normal lung tissue in green (28.23%), fSAD in yellow (34.96%), and emphysema in (36.13%) (Schiwek et al. 2021) '*Reproduced with permission from Springer Nature*'.

In the COSYCONET data set, the DCE-MRI series were refined manually in 41 out of 83 (50.6%) subjects by removing time points with minor respiratory artifacts before or after the CA bolus passage through the lungs in this study. Lung segmentation masks were generated automatically in all 83 (100%) cases. CT PRM data were available for 76 patients. Mean QDP for the whole lung was 54.6±17.8% for Otsu´s method, 52.7±17.7% for k-means clustering, and 51.7±9.3% for the 80th percentile method. The corresponding mean PBF was 50.6±24.8ml/100ml/min and the mean PBV was 3.8±1.7ml/100ml (Table 5).

Table 5: Quantitative imaging results of the COSYCONET study (Schiwek et al. 2021) '*Reproduced with permission from Springer Nature*'.

	Total	At risk for COPD	Former GOLD 0	GOLD 1	GOLD 2	GOLD 3	GOLD 4
Visual score							
MRI perfusion score	9.1 ± 2.9	8.4 ± 2.3	7.3 ± 3.0	7.2 ± 2.5	9.2 ± 3.1	9.5 ± 2.7	11.2 ± 1.7
QDP							
Otsu´s method	54.6 ± 17.8	42.0 ± 15.0	39.0 ± 10.3	32.4 ± 23.5	57.3 ± 16.2	60.4 ± 14.4	65.5 ± 16.8
K-means clustering	52.7 ± 17.7	40.0 ± 14.7	36.7 ± 11.4	30.7 ± 21.7	55.2 ± 15.6	58.5 ± 14.2	64.6 ± 17.2
80th percentile	51.7 ± 9.3	44.9 ± 9.1	43.7 ± 7.4	38.9 ± 17.2	52.7 ± 7.6	55.3 ± 7.1	57.7 ± 5.3
PBF/PBV							
PBF (ml/100ml/min)	50.6 ± 24.8	63.9 ± 27.1	65.9 ± 26.1	66.9 ± 23.4	44.5 ± 21.3	48.5 ± 27.0	42.8 ± 18.9
PBV (ml/100ml)	3.8 ± 1.7	4.6 ± 1.7	5.2 ± 1.7	5.5 ± 3.2	3.5 ± 1.2	3.5 ± 1.7	3.0 ± 1.3
CT PRM							
PRM_{Normal} (%)	51.4 ± 21.4	80.1 ± 9.6	77.1 ± 21.4	63.2 ± 12.5	51.2 ± 17.0	40.2 ± 11.0	27.0 ± 7.3
PRM_{Emph} (%)	13.7 ± 11.7	5.0 ± 4.6	5.1 ± 8.4	5.9 ± 6.4	12.2 ± 10.3	16.4 ± 10.1	31.0 ± 7.8
PRM_{fSAD} (%)	34.4 ± 13.7	14.6 ± 5.6	17.3 ± 13.5	30.1 ± 6.2	35.8 ± 10.8	42.9 ± 9.1	41.6 ± 6.5
$PRM_{Abnormal}$ (%)	48.6 ± 21.4	19.9 ± 9.6	22.9 ± 21.4	36.8 ± 12.5	48.8 ± 17.0	59.8 ± 11.0	73.0 ± 7.3

Data presented as mean ± SD

3.2.1   Association with MRI perfusion score

QDP calculated with both Otsu´s method or k-means clustering correlated strongly with the semi-quantitative MRI perfusion score for the whole lung (r=0.72 and r=0.71, p<0.001, respectively). QDP calculated with 80th percentile threshold as well as PBF and PBV correlated moderately with the MRI perfusion score for the whole lung (r=0.67, r=-0.49 and r=-0.54, p<0.001, respectively) (Figure 15, Table 6). QDP correlated significantly higher (Pearson and Filon's z) with the MRI perfusion score than PBF and PBV.

QDP calculated based on Otsu's method showed a range of values between 5.09 and 95.89%, based on k-means clustering between 4.91 and 95.23%, and based on the 80th percentile method between 15.17 and 68.82%, the latter being a compression of the observed value range compared to the other QDP quantification methods (Figure 15). Thus, the value range of QDP for the whole lung using Otsu's method and k-means clustering covered approximately 90% of the maximum theoretical range from 0-100%, but a smaller value range was observed for the 80th-percentile method with a range of approximately 53%. PBF showed a range of values between 7.30 and 147.03ml/min/100ml and PBV between 1.37 and 9.96ml/100ml.
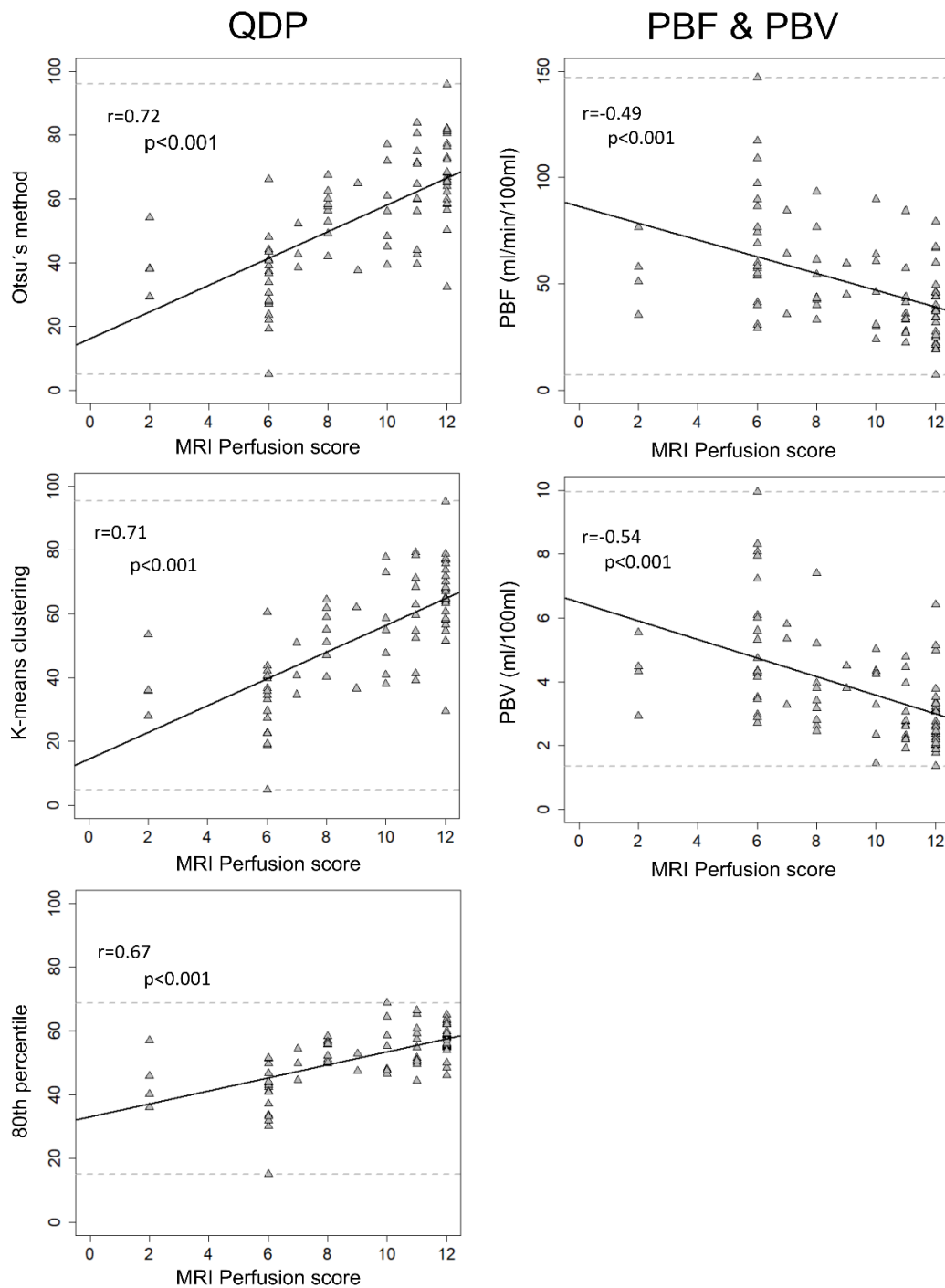
Figure 15: Scatterplots visualising the relationship between QDP, PBF, PBV and MRI perfusion score in the COSYCONET study. Linear regression lines are shown as bold lines, minimum and maximum observed values as dashed lines. Correlation coefficients and corresponding p-values are given in each panel (Schiwek et al. 2021) *'Reproduced with permission from Springer Nature'.*

Table 6: Comparison of quantitative DCE-MRI perfusion parameters with the MRI perfusion score in the COSYCONET study (Schiwek et al. 2021) '*Reproduced with permission from Springer Nature*'.

	QDP			PBF	PBV
	Otsu´s method	K-means clustering	80th percentile	(ml/100ml/min)	(ml/100ml)
MRI perfusion score whole lung					
r	0.72***	0.71***	0.67***	-0.49***	-0.54***
|95% CI|	0.54, 0.78	0.55, 0.78	0.48, 0.75	0.27, 0.61	0.31, 0.64
Mean diff	-2.31 ± 2.13	-2.50 ± 2.13	-0.13 ± 2.25	-5.02 ± 4.22	-4.52 ± 4.28
MRI perfusion score lobe-based					
Cohen´s kappa (κ)	0.48	0.47	0.39	-	-
%Agreement	73.29	72.69	68.67	-	-
Wilcoxon signed-rank test	0.06	0.27	0.38	-	-

95% CI=95% of confidence intervals, Mean diff=mean difference ± SD, %Agreement=percent agreement. *p<0.05, **p<0.01, and ***p<0.001

For the mean difference analysis in the whole lung, the quantitative values (QDP, PBF, PBV) were normalised to a maximum of 12. The mean difference between QDP and the MRI perfusion score (mean difference range from -0.13±2.25 to -2.50±2.13) was lower for all QDP quantification methods compared to the mean difference between MRI perfusion score and PBF or PBV (mean difference=-5.02±4.22 and -4.52±4.28, respectively) (Table 6).

For comparison by lobe, QDP were converted into discrete values of 0, 1, 2 at lobe level (Table 4). PBF and PBV could not be transferred to discrete values per lobe. The lobe-based comparison between QDP (all calculation approaches) and the MRI perfusion score, revealed moderate agreements with Cohen's κ ranging between 0.39 for the 80th percentile threshold and 0.48 for Otsu´s method. Cohen's κ is usually used to measure inter- and intra-reader reliability for categorical items (McHugh 2012). Therefore, the continuous variable QDP had to be converted into discrete values to enable the lobe-based comparison between score and QDP.

The Wilcoxon signed rank test was employed to test if the difference between QDP and the MRI perfusion score had an asymmetrical distribution, e.g. if one method under- or overestimate the perfusion defects systematically. All lobe values were considered and p-values smaller than 0.05 in the Wilcoxon signed rank test were considered to indicate a non-symmetrical distribution of the differences. No asymmetrical distribution between QDP (for all quantification approaches) and the MRI perfusion score was found (Table 6).

3.2.2 Association with quantitative CT

The comparison of the QCT parameters with the quantitative and semi-quantitative MRI perfusion parameters was possible only in the COSYCONET study. QDP (all approaches) correlated strongly with PRM_{Emph} (r=0.75 to 0.70, p<0.001) and moderately with $PRM_{Abnormal}$ (r=0.65 to 0.61, p<0.001), but only weakly with PRM_{fSAD} alone (r=0.34 to 0.37, p<0.01). In contrast, PBF and PBV were moderately correlated with $PRM_{Abnormal}$ (r=-0.52 and r=-0.64, p<0.001, respectively) and PRM_{Emph} (r=-0.51 and r=-0.64, p<0.001, respectively), but weakly with PRM_{fSAD} (r=-0.38 and r=-0.40, p<0.001, respectively). The MRI perfusion score correlated moderately with $PRM_{Abnormal}$ (r=0.51, p<0.001) and PRM_{Emph} (r=0.56, p<0.001), but weakly with PRM_{fSAD} (r=0.29, p<0.01) (Table 7). QDP based on Otsu´s method and k-means clustering correlated significantly higher (Pearson and Filon's z) with PRM_{Emph} and $PRM_{Abnormal}$ than the MRI perfusion score, PBF and PBV.

Table 7: Comparison of DCE-MRI perfusion parameters with CT PRM parameters in the COSYCONET study (Schiwek et al. 2021) '*Reproduced with permission from Springer Nature*'.

	MRI perfusion score	QDP			PBF (ml/100ml/ min)	PBV (ml/100ml)
		Otsu´s method	K-means clustering	80th percentile		
PRM$_{Abnormal}$ (%)						
r	0.50***	0.63***	0.65***	0.61***	-0.51***	-0.63***
|95% CI|	0.30, 0.65	0.48, 0.76	0.49, 0.78	0.42, 0.74	0.32, 0.66	0.48, 0.75
Mean diff	-	6.03 ± 16.94	4.15 ± 16.39	3.23 ± 17.08	-	-
PRM$_{Emph}$ (%)						
r	0.56***	0.74***	0.75***	0.70***	-0.51***	-0.64***
|95% CI|	0.38, 0.69	0.62, 0.83	0.62, 0.84	0.56, 0.80	0.32, 0.66	0.50, 0.77
Mean diff	-	40.4 ± 13.28	38.53 ±12.91	37.61 ± 9.17	-	-
PRM$_{fSAD}$ (%)						
r	0.29**	0.35**	0.37**	0.34**	-0.38***	-0.40***
|95% CI|	0.07, 0.46	0.12, 0.55	0.15, 0.55	0.11, 0.55	0.16, 0.55	0.19, 0.58
Mean diff	-	19.68 ±17.67	17.81 ± 7.28	16.88 ±12.79	-	-
*p<0.05, **p<0.01, and ***p<0.001						

To evaluate whether QDP or PRM revealed a larger extent of abnormalities, Bland-Altman analyses were performed. Overall, more pulmonary perfusion defects were found than emphysema extent (mean difference of PRM$_{Emph}$–QDP: 40.4±13.28 to 37.61±9.17) and more than fSAD alone (mean difference of PRM$_{fSAD}$–QDP: 19.68±17.67 to 16.88±12.79). When considering the two PRM pathologies together, i.e. PRM$_{Abnormal}$, pulmonary perfusion defects were in the same range as non-normal lung tissue (mean difference of PRM$_{Abnormal}$–QDP: -5.42±16.72 to -0.86±19.04) (Figure 16, Table 7).
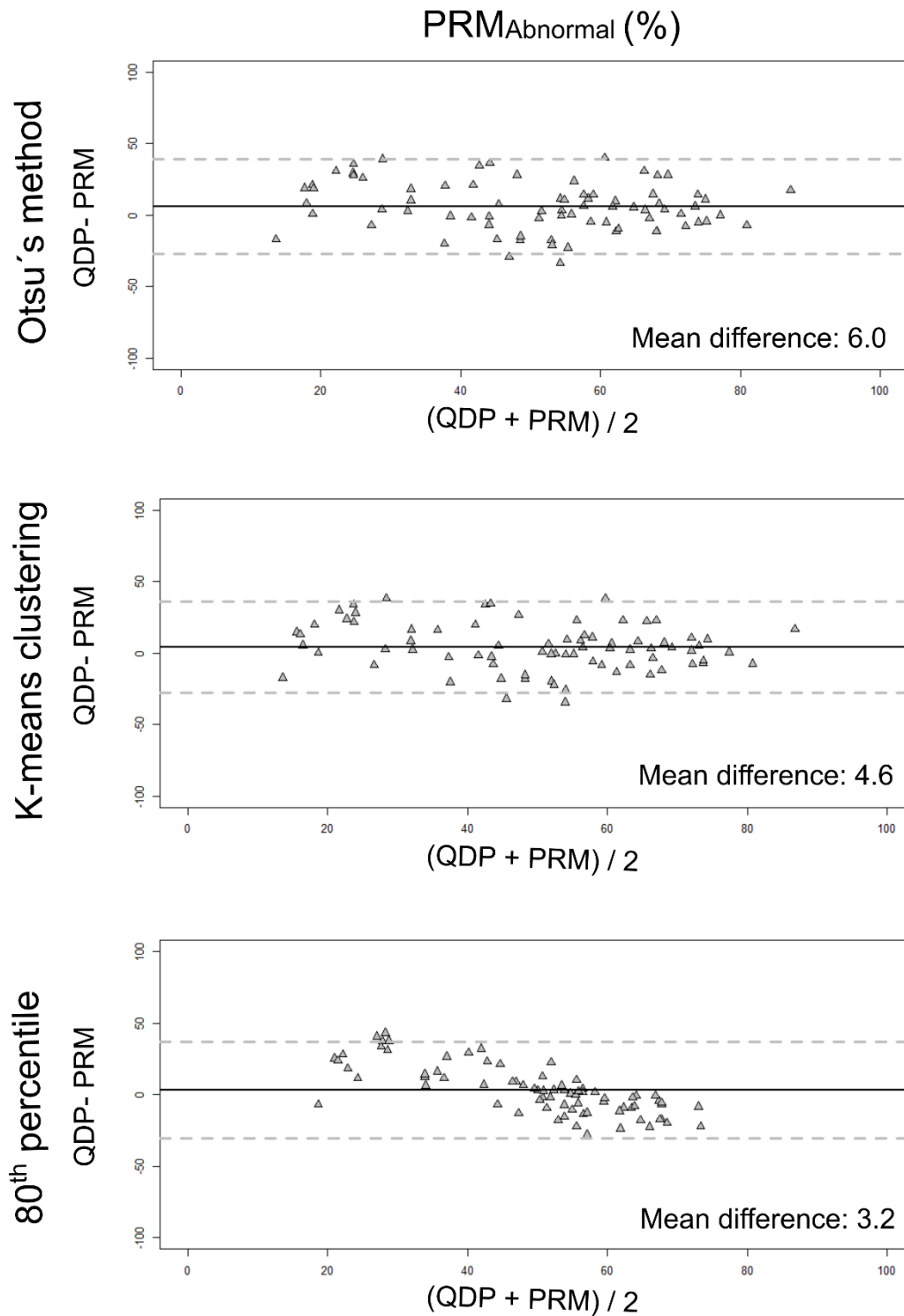
Figure 16: Bland-Altman plot between QDP based on Otsu´s method, k-means clustering and 80th percentile threshold quantified from DCE-MRI data and CT-derived PRM$_{Abnormal}$. Solid lines represent mean difference and dashed lines represent limits of agreement (+-1.96SD). Mean difference between QDP and PRM$_{Abnormal}$ was close to zero (Schiwek et al. 2021) *'Reproduced with permission from Springer Nature'.*

3.2.3 Association with pulmonary function testing

QDP (all approaches), PBV and the MRI perfusion score correlated moderately with FEV1/FVC (r=0.40 to -0.54, p<0.001). Only a weak correlation of r=0.28 (p<0.01) was observed for PBF and FEV1/FVC (Table 8). No statistically significant differences were observed between the correlation coefficients of QDP and the MRI perfusion score with FEV1/FVC. In contrast, QDP correlated significantly higher with FEV1/FVC than PBF (except for QDP based on 80th percentile) and QDP based on k-means clustering correlated significantly higher with FEV1/FVC than PBV.

Table 8: Comparison of DCE-MRI perfusion parameters with PFT (Schiwek et al. 2021) '*Reproduced with permission from Springer Nature*'.

| | MRI perfusion score | QDP | | | PBF (ml/100ml/min) | PBV (ml/100ml) |
		Otsu´s method	K-means clustering	80th percentile		
FEV1%predicted						
r	-0.39***	-0.43***	-0.44***	-0.49***	0.26*	0.38***
|95% CI|	0.18, 0.56	0.22, 0.59	0.25, 0.61	0.32, 0.64	0.04, 0.45	0.19, 0.54
FEV1/FVC						
r	-0.45***	-0.50***	-0.51***	-0.54***	0.28**	0.40***
|95% CI|	0.26, 0.62	0.31, 0.65	0.32, 0.65	0.37, 0.68	0.07, 0.47	0.20, 0.57
*p<0.05, **p<0.01, and ***p<0.001						

3.3   Reproducibility study

Figure 17 visualises the QDP, PBF and PBV quantification for MRI1 and MRI2 (baseline and follow-up) in a representative CF patient and COPD patient. QDP was 21.57% at MRI1 and 20.61% at MRI2 for the CF patients. QDP was 42.96% at MRI1 and 43.56% at MRI2 for the COPD patient. Perfusion score was 8 at MRI1 and 7 at MRI2 for the CF patient. MRI Perfusion score was 12 at MRI1 and 12 at MRI2 for the COPD patient. FEV1% predicted was 60.90% at MRI1 and 63.00% at MRI2 for the CF patient (pre-bronchodilator). FEV1% predicted was 29.90% at MRI1 and N/A at MRI2 for the COPD patient (post-bronchodilator).
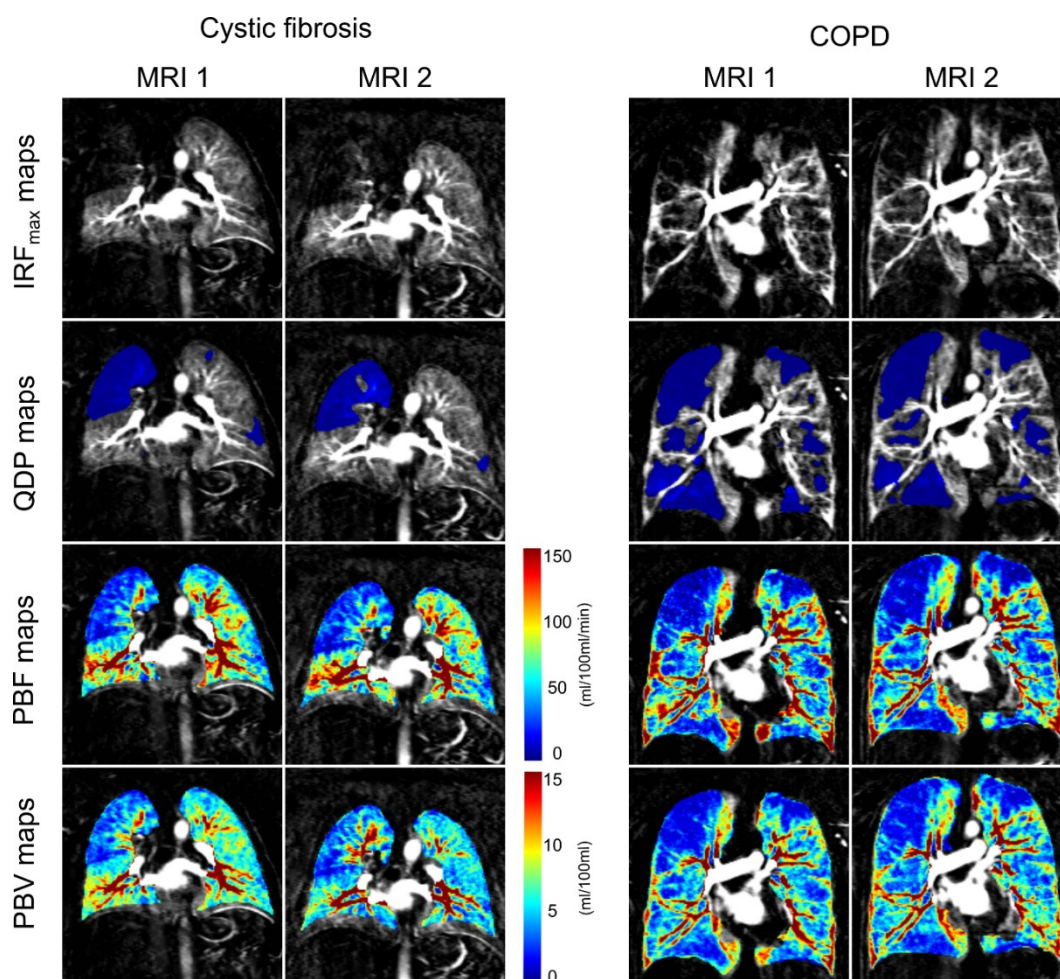
Figure 17: Coronal IRF$_{max}$ maps, corresponding QDP maps (defects highlighted in blue) and PBF maps and PBV maps from a representative CF and COPD patient at MRI1 and MRI2 of the reproducibility study. Submitted for publication.

Four DCE-MRI data (5.7%) from three different patients (three MRI1 and one MRI2) could not be visually scored due to contrast bolus mistiming and low enhancement. The quantitative perfusion analysis was not performed in eleven cases (15.7%), from 8 patients (six MRI1 and five MRI2 visits), due to contrast bolus mistiming, low enhancement, or substantial breathing artefacts. 27 COPD and CF patients were evaluated quantitatively at both visits. Three patients with CF (20.0%) and one with COPD (5.0%) experienced a pulmonary exacerbation between the two visits, resulting in additional treatments, which were completed at least seven days before MRI2 without postponing scheduled scans. One CF patient received oral antibiotics for other reasons than a pulmonary exacerbation.

3.3.1   Reproducibility

The 4-week reproducibility of the quantitative perfusion parameters (QDP, PBF and PBV) was investigated in clinically stable patients with CF and COPD in the reproducibility study. Out of the three quantitative MRI perfusion parameters evaluated, only QDP increased significantly in COPD from MRI1 to MRI2 with a mean difference of 7.4 (LoA=±21.2, p<0.05). In CF, QDP tended to increase from MRI1 to MRI2 with a mean difference of 1.9 (LoA=±14.7, p=0.273). PBF and PBV tended to increase (p=0.216 and p=0.542, respectively) in CF as well but tended to decrease (p=0.104 and p=0.715, respectively) in COPD from MRI1 to MRI2 (Figure 18, Table 9).
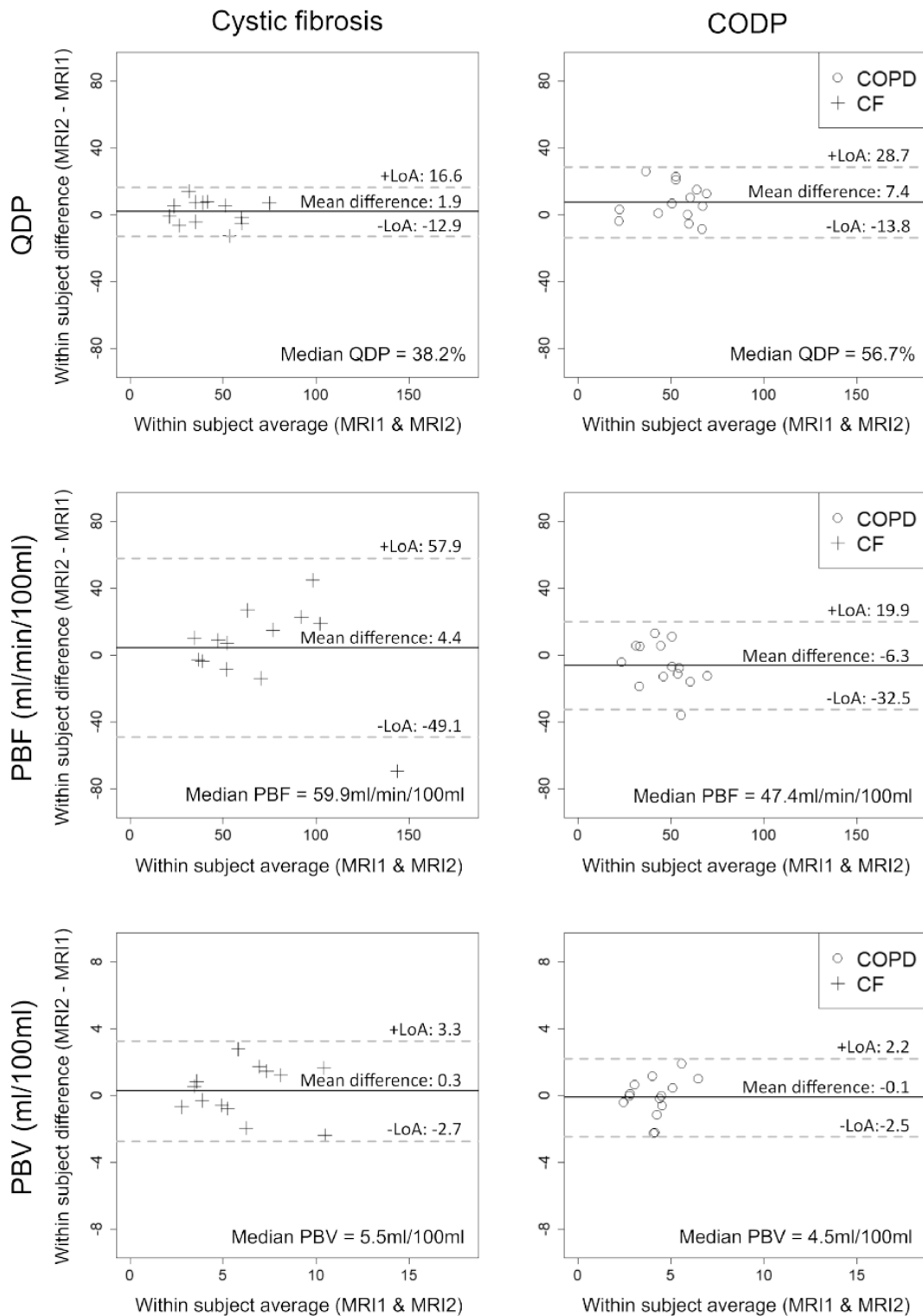
Figure 18: Mid-term reproducibility of quantitative perfusion abnormalities in adults with clinically stable CF and COPD presented as Bland-Altman plots. Mean difference, LoA and median values are given for each panel. Solid lines indicate the mean difference between MRI1 and MRI2, dashed lines the LoA (± 1.96·SD). Submitted for publication.

Table 9: Reproducibility of quantitative pulmonary perfusion parameters in clinically stable cystic fibrosis and COPD patients. Submitted for publication.

	Cystic fibrosis		COPD	
	MRI1	MRI2	MRI1	MRI2
Mean ± SD				
QDP	39.1 ± 18.9	42.8 ± 15.8	48.7 ± 15.9	54.3 ± 17.4*†
PBF (ml/100ml/min)	75.8 ± 47.9	70.9 ± 29.9	50.0 ± 15.9	47.4 ± 23.2
PBV (ml/100ml)	6.28 ± 2.8	6.12 ± 2.6	4.31 ± 1.1	4.44 ± 2.2†
LoA				
QDP	±14.7 (±38% of the median)		±21.2 (±37% of the median)	
PBF (ml/100ml/min)	±53.5 (±89% of the median)		±26.2 (±55% of the median)	
PBV (ml/100ml)	±3.0 (±55% of the median)		±2.3 (±51% of the median)	
MID				
QDP	5.3 (13.9% of the median)		7.7 (13.6% of the median)	
PBF (ml/100ml/min)	19.3 (32.2% of the median)		9.5 (20.0% of the median)	
PBV (ml/100ml)	1.1 (20.0% of the median)		0.8 (17.8% of the median)	

MID were calculated based on standard error of measurement from rANOVA.

*$p<0.05$, **$p<0.01$, and ***$p<0.001$ MRI1 vs. MRI2

† $p<0.05$ COPD versus cystic fibrosis at MRI2

The LoA values were related to the observed median of the parameter to account for the different value ranges of QDP, PBF, and PBV. In CF, the observed LoA related to the median were 38.61% for QDP, 89.38% for PBF and 55.05% for PBV. In COPD, the observed LoA related to the median were 37.48% for QDP, 55.24% for PBF and 51.66% for PBV. MIDs were distinctly smaller related to the median for QDP (CF: 13.9%, COPD: 13.6%) compared to PBF (CF: 32.2%, COPD: 20.0%) and PBV (CF: 20.0%, COPD: 17.8%) (Table 9).

3.3.2   Association with MRI perfusion score

In the reproducibility study, the observed correlation between QDP and MRI perfusion score was moderate in CF patients (r=0.46, p<0.05) and COPD patients (r=0.66, p<0.001). In comparison, PBF and PBV correlated poorly with the MRI perfusion score in CF (r=-0.29, p=0.132 and r=-0.35, p=0.067, respectively) and moderately in COPD (r=-0.57, p<0.001 and r=-0.57, p<0.001, respectively) (Figure 19). In comparison, QDP correlated significantly better (Pearson and Filon´s z) with the MRI perfusion score than PBF and PBV.
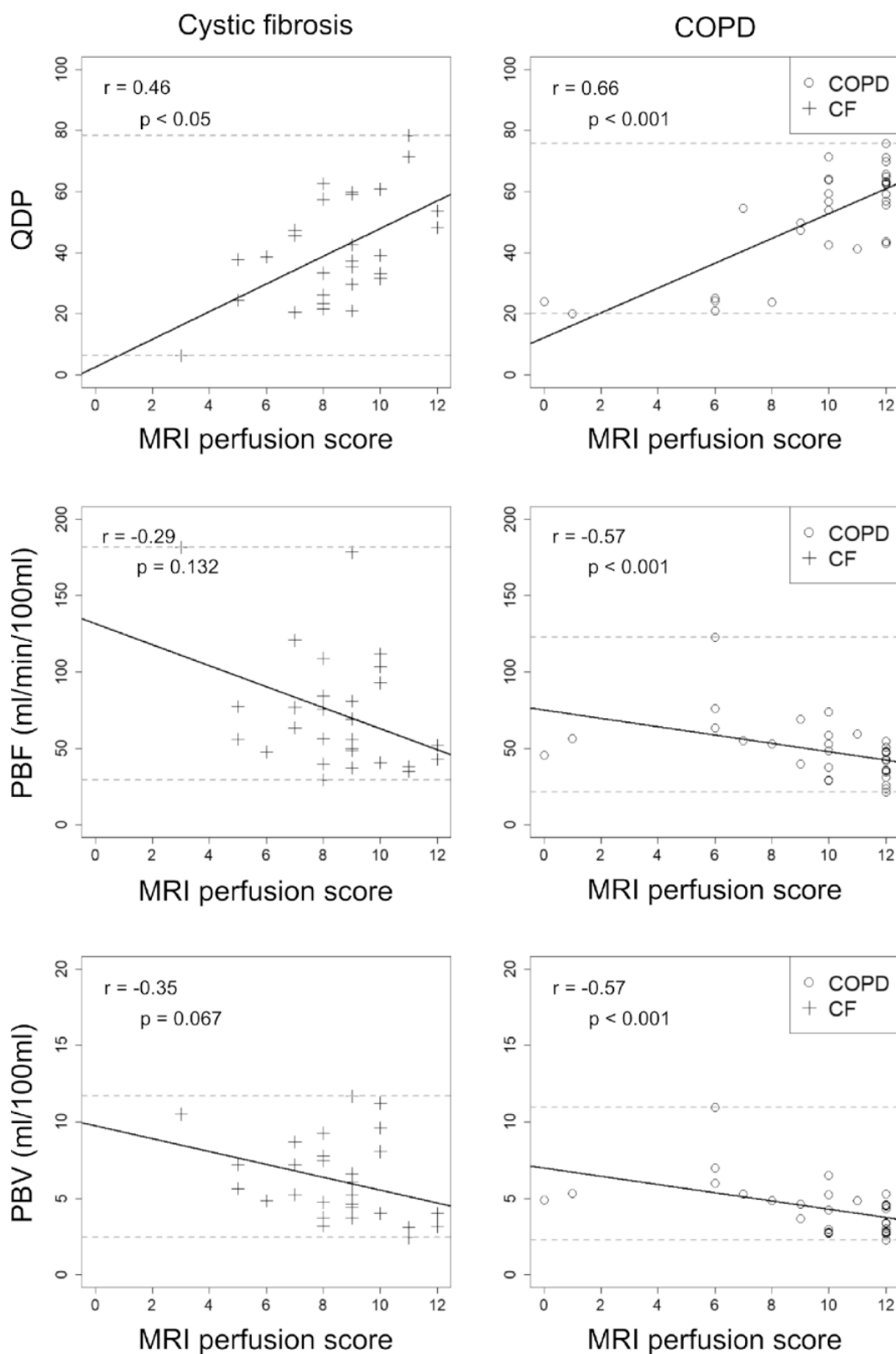
Figure 19: Scatterplots to illustrate the relationship between QDP, PBF, PBV and MRI perfusion score combined for MRI1 and MRI2 but separated for CF and COPD in the reproducibility study. CF patients are represented by crosses and COPD patients by circles. Correlation coefficients and corresponding p-values are given in each panel. Solid lines indicate the linear regression, dashed lines the minimum and maximum observed value for the parameter of the y-axis. Submitted for publication.

3.3.3 Association with pulmonary function testing

Higher correlations between MRI findings and FEV1%predicted were observed for CF compared to COPD when combining MRI1 and MRI2. The highest correlation with FEV1% predicted was found for QDP ($r=-0.47$, $p<0.05$), followed by PBV ($r=0.44$, $p<0.05$) and PBF ($r=0.38$, $p<0.05$) in CF. In COPD patients, QDP ($r=-0.07$, $p=0.75$) as well as PBF ($r=0.10$, $p=0.623$) and PBV ($r=0.09$, $p=0.679$) correlated only weakly with FEV1% predicted (Figure 20). QDP did not correlate significantly better (Pearson and Filon's z) with FEV1%predicted neither compared to PBF nor to PBV.
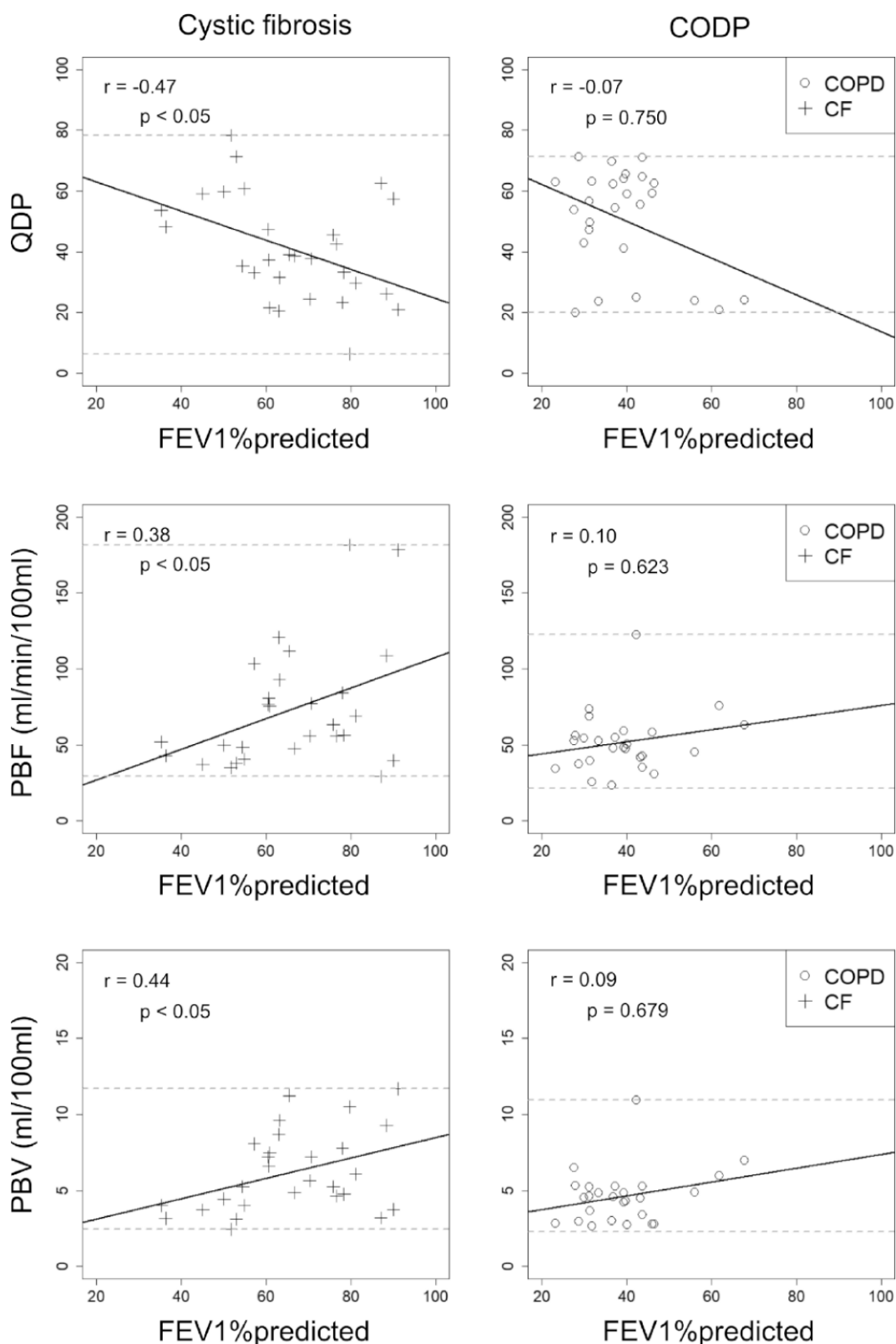
Figure 20: Scatterplots visualising the relationship between QDP, PBF, PBV and FEV1% predicted combined for MRI1 and MRI2 but separated for CF and COPD in the reproducibility study. CF patients are represented by crosses and COPD patients by circles. Correlation coefficients and corresponding p-values are given in each panel. Solid lines indicate the linear regression, dashed lines the minimum and maximum observed value for the parameter of the y-axis. Submitted for publication.

4 DISCUSSION

The development of imaging methods to quantify pulmonary perfusion from DCE-MRI data offers new possibilities for the clinical development of new therapies for muco-obstructive lung diseases by using perfusion-related parameters as response-to-treatment and prognostic biomarker, since perfusion abnormalities may precede structural, often irreversible, changes of the lung parenchyma before being detectable from CT or MRI data. In this work, a novel biomarker was developed to quantify the extent of pulmonary perfusion defects in percent (QDP) from DCE-MRI data. The work focused on the development of a clinically meaningful and reproducible biomarker. For this purpose, unsupervised image clustering algorithms were combined with mathematical models of tracer kinetics (indicator dilution theory).

Using data from the COSYCONET study, QDP was developed and optimised by comparing three different clustering approaches (Otsu's method, k-means clustering and 80th percentile threshold). In this study, the technical and clinical validation was performed against the MRI perfusion score, QCT parameters and PFT parameters. The best results were observed for QDP based on Otsu's method, which was thus further developed and evaluated in a second study (reproducibility study). In the second study, QDP's reproducibility was evaluated, and the technical and clinical validation continued by comparing QDP with the MRI perfusion score and PFT parameters.

4.1 Data quality and the influence of noise

Pulmonary perfusion abnormalities occur in muco-obstructive lung diseases in response to alveolar hypoxia and the HPV mechanism, as well as due to obliterations of the alveolar-capillary bed and pulmonary vessels by emphysematous destruction. DCE-MRI is an established method to assess regional changes in pulmonary perfusion. However, the image

quality of DCE-MRI data in the lungs can distort perfusion quantification and increase the variability of the quantitative parameters. In previous studies with similar DCE-MRI pulse sequences and pulmonary CA application specifications, it was already reported that the DCE-MRI data of the lungs were affected by severe artefacts due to the keyhole acquisition concept, respiratory motion, susceptibility effects, low CNR, non-linearity of the CA-signal relationship, and low temporal resolution (Neeb et al. 2009; Puderbach et al. 2008).

Consequently, this could lead to physiologically undesirable and unreliable values when quantifying pulmonary perfusion. Previous studies have already shown that low CNR and low temporal resolution increase the variability of PBF and PBV quantification (Ingrisch et al. 2010; Ravesh et al. 2013). In this work, the influence of different CNR on the calculation of IRF and thus on the calculation of PBF was simulated with two different regularisation methods. Based on the results of the simulations the method for the calculation of the IRF maps from the actual DCE-MRI data was chosen. The CNR range (2-20) simulated in this work was only approximated from observed/real CNR ranges. A direct assessment of the CNR in the actual DCE-MRI was not considered useful since the image noise is non-uniformly distributed due to the parallel imaging and the keyhole concept. Nevertheless, low CNRs can be assumed because of the low contrast enhancement observed in the lung parenchyma, especially in severe COPD patients.

In the simulations, SFTR with LLC underestimated PBF values less than tSVD at high CNRs, which is in line with data from Ravesh et al. (Ravesh et al. 2013). However, in contrast to tSVD, PBF was skewed towards lower values at lower CNRs when using SFTR with LCC. Furthermore, the simulations showed a higher variability of PBF values calculated with SFTR with LCC at lower CNRs compared to tSVD. Therefore, tSVD with a fixed threshold of 20%

was chosen for the regularisation of the actual DCE-MRI data, since the focus of this work was to develop robust and reproducible methods for use in clinical studies. However, the simulations did not consider other influencing factors, such as temporal resolution or non-linearity of the CA-to-signal-relationship, which could have a further negative impact on the calculation of IRF and PBF.

4.2 Development and optimisation – COSYCONET study

QDP was developed based on data from the COSYCONET study acquired at the Thoraxklinik Heidelberg by a comparative evaluation (selection process) of three different unsupervised clustering approaches, namely Otsu´s method, k-means clustering and 80th percentile threshold, to assess strengths and weaknesses of each approach. For this purpose, QDP was validated against the MRI perfusion score but also against QCT and PFT parameters since perfusion abnormalities are associated with both the destruction of lung parenchyma and airflow limitations.

Overall, QDP based on Otsu's method showed the highest level of agreement with MRI perfusion score, QCT, and PFT parameters. A compressed range of observed values was found for the percentile method compared to the other methods, which is caused by its underlying calculation method, regardless of the used percentile and factor. The compressed value range prevents an accurate determination of the perfusion defects, which was reflected in the results as the comparability with the MRI perfusion score was affected. Overall, a major limitation of QDP is that it has to detect defects, since the number of clusters is predetermined and therefore probably cannot be used in healthy subjects.

The three clustering methods, which were evaluated in the COSYCONET study, were chosen based on literature from lung MRI. In previous DCE-MRI studies, percentile thresholds were used to quantify pulmonary perfusion defects (Heimann et al. 2012; Kaireit et al. 2019). The percentile and factor used in this work were empirically determined in a previous study (Heimann et al. 2012) and hence may not be transferable to data of other MRI acquisitions techniques. Otsu´s methods and k-means clustering were previously used on hyperpolarised gas MRI (Capaldi et al. 2018; Kirby et al. 2010; Kirby et al. 2012). Furthermore, different source images, i.e. C(t) maps, IRF_{max} maps, PBF maps and PBV maps, were evaluated as basis for the QDP quantification (data not shown). QDP quantification using IRF_{max} maps distinguished well-perfused areas from poorly-perfused areas in the lungs more accurately compared to QDP with other source images.

4.3 Performance comparison

4.3.1 Reproducibility

The 4-week reproducibility, which is of paramount importance for the clinical use of QDP, was evaluated in clinically stable CF and COPD patients. In the Bland-Altman analyses, QDP showed a higher reproducibility with smaller LoAs related to the median and a lower susceptibility to outliers compared to PBF and PBV. The observed LoAs related to the median for PBF and PBV in COPD patients were comparable to results from previous studies, which only investigated PBF and PBV. In a short-term reproducibility study with one day between the MRI examination in fourteen healthy subjects and manual lung segmentation, Ley-Zaporozhan et al. found significant differences between the examinations in the intra-observer comparison with LoAs of about 42% of the mean PBF and with LoAs of about 47% of the mean PBV (Ley-Zaporozhan et al. 2011). In another short-term reproducibility study in COPD patients with one day between the MRI examinations, Ter-Karapetyan et al. showed LoAs of

approximately 46% of the observed mean PBF and 53% of the observed mean PBV (Ter-Karapetyan et al. 2018). However, this study speculated that the reproducibility was limited by recirculating contrast agent. In CF, the observed higher LoA for PBF compared to PBV, but also to the LoA in COPD patients, was driven by outliers. Due to the small number of patients, a small number of outliers can lead to a substantial increase in variability. Given the pathophysiologic differences between CF and COPD, a better reproducibility in CF compared to COPD was expected due to the better DCE-MRI data quality. The underlying mucus-related disease processes in CF lead to an increase in proton density ('plus pathology'), whereas emphysema in COPD leads to a decrease in proton density ('minus pathology') (Wielpütz and Kauczor 2012). However, only QDP showed a better reproducibility in CF compared to COPD but neither PBF nor PBV. The increased perfusion in CF compared to COPD could be the reason that the variability of PBF and PBV in CF has increased due to their calculation methods and the used DCE-MRI data of the lungs as described in the following paragraphs.

A better reproducibility in the QDP quantification was achieved by mitigating some challenges of DCE-MRI data of the lungs. QDP uses the advantages of both the mathematical models based on the principles of tracer kinetics for non-diffusible tracers (Meier and Zierler 1954; Zierler 1962) by using IRF maps and unsupervised image clustering algorithms. The utilisation of clustering algorithms enables the assessment of all voxels relative to each other. As a result, only the differences between the values are important rather than their individual absolute values (magnitudes). Thus, an intrinsic normalisation of the values was achieved in the QDP quantification, which makes the quantification more robust against perturbations of the applied tracer kinetics models on a global level, i.e. whole lung. In contrast, PBF and PBV quantification employs the IRF in each lung voxel individually, which makes the calculation more susceptible to interferences affecting the whole lung. The following aspects have a major

negative impact on the PBF and PBV quantification and may be, at least partially, mitigated by the intrinsic normalisation through the unsupervised clustering approach of QDP.

The extraction of exact values from the IRF is not always straightforward, because the contrast concentrations must be quantified accurately, and the AIF must be measured close to the tissue of interest (Calamante et al. 2000; Duhamel et al. 2006; Sourbron et al. 2006). In this work, $C(t)$ maps were calculated by subtracting the non-enhanced signal S_0 from $S(t)$, which did not result in a proper normalisation. However, approximating $C(t)$ by Eq. 14, i.e. by normalising to S_0, resulted in a distinct noise amplification. In addition, although the AIF for the whole lung (global) was measured as close as possible to the lung parenchyma in the main pulmonary artery, a certain lag time between the AIF and $C(t)$ in the lung parenchyma could not be avoided. A local AIF determination, for example for every lobe, was not possible due to the spatial resolution of the DCE-MRI data. Both factors led to an overestimation of $C(t)$ and hence to an overestimation of PBF and PBV.

The low temporal resolution of DCE-MRI data of the lungs leads to undersampling effects resulting in inconsistent underestimations of the AIF maximum between scans and patients (Ingrisch et al. 2010). This becomes apparent in the AIF curves as the maximum peak of the AIF was often cut off, resulting in two peaks. The resulting systematic error in the AIF maximum may lead to interscan variabilities in the IRF after the deconvolution of the AIF with $C(t)$ in each lung voxel. However, since all values of the IRF within the same scan are underestimated by the same factor, the interscan variability of QDP is distinctly less affected than that of PBF and PBV.

Non-linearities in the signal-to-CA-concentration relationship in the AIF as described by Neeb et al. and Puderbach et al. can have a negative impact on the PBF and PBV quantification (Neeb et al. 2009; Puderbach et al. 2008). If the signal enhancement in the AIF is not in the linear range of the relationship between signal change and concentration of CA, the CA concentration in the AIF will be underestimated leading to an overestimation of PBF and PBV. It was not examined in this work whether the signal enhancement was in the linear range of the relationship between signal intensity and CA concentration but approximated based on observed signal enhancement in the pulmonary artery (data not shown) and available literature (Neeb et al. 2009; Pintaske et al. 2006; Puderbach et al. 2008). However, these considerations only have a minor influence on the QDP calculation (intrinsic normalisation) as all values within the same scan are underestimated by the same factor. In contrast, non-linearities will increase the variability of PBF and PBV between scans due to the utilisation of absolute values from the IRF.

Changes in lung density and thereby proton density caused by differences in the inspiratory level between scans can have a substantial influence on the PBF and PBV values as evaluated by Fink et al. and Ingrisch et al. (Fink et al. 2005b; Ingrisch et al. 2014). The inspiratory level has only little effect on QDP because the density in the lungs changes evenly and with this also the values in the IRF. The intrinsic normalisation of the QDP quantification can compensate for evenly distributed changes in the lungs and perfusion defects are neither over- nor underestimated.

An incomplete coverage (or variable coverage) of the passage of the CA through the lungs due to mistiming of the CA application or prolonged CA passage through the lungs can lead to an underestimation of PBF and PBV. In addition, in this work, time points affected by breathing

before or after the first passage of the CA through the lung parenchyma were removed from the quantification process, which can lead to a further underestimation of PBF and PBV. Both processes lead to an underestimation of PBF and PBV, thereby increasing their variability. In contrast, the QDP calculation, which utilises relative values due to the intrinsic normalisation of the clustering algorithms, is substantially less affected by the variable coverage of the CA passage, as the values are underestimated in all voxels by the same factor.

One limitation of the QDP calculation is the strong spatial filtering of the image data, which is needed due to the present data quality, which may improve the reproducibility but could result in a loss of accuracy. However, this can be mitigated in future studies by optimising the acquisition technique or further investigations could prove that the strong filtering within a slice is appropriate in the lungs, because the smallest functional unit regulating lung perfusion is 1-2.5cm in diameter (Heitzman et al. 1969; Webb 2006).

4.3.2   Clinical parameters

When comparing the performance of QDP to the performance of PBF and PBV, it is important to investigate not only the reproducibility but also the clinical meaningfulness by evaluating the relationship of the quantitative perfusion parameters to the MRI perfusion score, QCT, and PFT parameters.

In both studies, the observed correlations with the MRI perfusion score were lower for PBF and PBV than for QDP. However, it has to be mentioned that QDP was primarily developed to reflect the MRI perfusion score, which means that the comparison has only limited validity for the performance comparison between QDP, PBF and PBV. Furthermore, QDP and MRI perfusion score assess the same attribute (defect extent) but PBF and PBV not (blood flow and

volume), which further limit the validity of the performance comparison. In the reproducibility study, only QDP detected a low but significant change between the two visits for COPD. The study by Wielpütz et al., which investigated the same patient population with the complete morpho-functional scoring system, also reported a significant change in the same direction for the MRI global score in COPD. It was speculated that a low but true subclinical increase in disease severity was detected by the MRI global score (Wielpütz et al. 2019), which could also be the case for QDP.

The performance of the quantitative perfusion parameters was compared in relation to QCT parameters in the COSYCONET study and to PFT parameters in the COSYCONET as well as in the reproducibility study. In all correlation analyses, QDP correlated higher with all PRM parameters and PFT parameters than PBF and PBV. These findings suggest that QDP is more adequate than PBF and PBV in identifying disease status, monitoring, and diagnosis. However, QDP and PRM parameters assess the same attribute (extent), but PBF and PBV do not (blood flow and volume), giving QDP an advantage over PBF and PBV in the performance comparison.

Another difference between QDP and PBF/PBV becomes apparent when used as global parameter for the whole lung. The redistribution of blood flow by HPV from poorly ventilated areas to better ventilated areas may lead to a disguise of pathologies when quantifying PBF and PBV for the whole lung. This limits the usefulness of PBF and PBV for monitoring disease progression or determining disease severity, as it may result in an underestimation of pathology for the whole lung. In contrast, the QDP quantification takes only the extent of perfusion defects into account but no redistribution effects, due to the intrinsic normalisation. Furthermore, poorly perfused lung regions can be better delineated from well-perfused lung

regions by the QDP approach when an increase in perfusion by the HPV in well-ventilated areas occur.

4.4 Clinical considerations

In previous studies, the general concept of assessing the extent of functional lung abnormalities in percent appeared to be clinically meaningful. For instance, ventilation defects in percent quantified from hyperpolarised gas MRI have already successfully been used to monitor treatment response in CF (Altes et al. 2017; Rayment et al. 2019). Initial studies regarding pulmonary perfusion defects in percent quantified from DCE-MRI and FD-MRI data also indicated the potential of the method, but further evaluation was missing to date (Bauman et al. 2013; Kaireit et al. 2019).

In healthy lungs, pulmonary perfusion provides complementary or overlapping information to ventilation due to the HPV relationship (Euler and Liljestrand 1946). In the presence of inflammation, HPV can be blocked as described in section 1.2.2. (Barbera et al. 1990; Gust et al. 1998; Hoffman et al. 2006). However, the ability to block the HPV in inflamed lung regions seems to be suspended in emphysema-susceptible patients (Alford et al. 2010). Therefore, it was hypothesised that pulmonary perfusion abnormalities themselves may contribute to or at least precede the development of irreversible emphysema. Therefore, pulmonary perfusion could potentially be used as prognostic marker for emphysema progression.

Furthermore, in literature it was speculated that pulmonary perfusion abnormalities are an at least partially reversible component of muco-obstructive lung diseases and may play a key role in disease onset and progression (Alford et al. 2010; Hueper et al. 2015; Zhou-Suckow et al. 2017). This hypothesis has already been supported in both CF and COPD patients, as partial

reversibility of perfusion abnormalities has been demonstrated using DCE-MRI and the MRI perfusion score or PBF after therapeutic intervention (Vogel-Claussen et al. 2019; Wielpütz et al. 2014). Perfusion abnormalities assessed by DCE-MRI are likely to be composed of effects related to HPV and irreversible degradation of lung tissue, including pulmonary vessels, which means that it is only partially reversible, especially in COPD. Pulmonary perfusion abnormalities could thus serve as response-to-treatment biomarker in clinical studies investigating new treatments for COPD or CF. Reversible abnormalities are, in contrast to irreversible abnormalities, of particular interest for interventional studies in early clinical drug development, which ideally require short follow-up periods up to 3 months with a limited number of patients. Clinical studies assessing irreversible abnormalities such as bronchiectasis or emphysema would require longer study durations since response to treatment can only be determined by demonstrating a slowdown in progression.

The relationship of QDP from DCE-MRI data to fSAD from CT data was also examined in this work. fSAD was chosen for this evaluation, because studies in COPD could already demonstrate that fSAD precedes the development of emphysema using CT data (Boes et al. 2015; Labaki et al. 2019). Furthermore, it was speculated that fSAD is partially reversible as it represents an inflammatory component of the disease (Boes et al. 2015). Consequently, the evaluation of the relationship between perfusion abnormalities and fSAD can strengthen the importance of pulmonary perfusion as prognostic and response-to-treatment biomarker.

Significant correlations were found between QDP and the PRM parameters PRM_{Emph}, PRM_{fSAD}, and $PRM_{Abnormal}$. Furthermore, the extent of perfusions defects from MRI data corresponds to the CT-derived extent of abnormal lung (combined extent of emphysema and fSAD), indicating that QDP is a surrogate for morphological abnormalities detected by PRM.

When considered separately, more perfusion defects were observed compared to emphysema or fSAD alone, supporting this hypothesis. In contrast, only weak associations were observed between PBF using DCE-MRI data and small airways disease from CT data in a previous study (Hueper et al. 2015).

PFT is an important clinical method for assessing patient condition as it is a measure of airflow limitations. PFT is critical for disease monitoring, prognosis, and treatment decisions in muco-obstructive lung diseases. Therefore, the relationship of QDP to PFT parameters was evaluated to assess its clinical meaningfulness. QDP correlated moderately with FEV1% predicted in patients with CF (reproducibility study) and with FEV1% predicted and FEV1/FVC in patients with COPD (COSYCONET study). These findings are consistent with previous studies (Kaireit et al. 2019; Xia et al. 2014) and in agreement with the understanding that a reduction in FEV1% or FEV1/FVC is mainly driven by large airway obstruction, whereas pulmonary perfusion abnormalities probably reflect small airways pathologies (Hueper et al. 2015; Wielpütz et al. 2014). In the reproducibility study, no relevant correlations between QDP and FEV1% predicted were observed in COPD, which is most likely due to a limited range of disease severity in the evaluated patients in this study.

4.5   Lung segmentation

The segmentation of the lungs and trachea on GRE MRI images has rarely been done and required a bespoke solution (Heimann et al. 2012; Kohlmann et al. 2015). Therefore, it was one of the main goals of this work to develop and implement a completely new lung segmentation pipeline based on a region-growing algorithm. Watershed algorithms were introduced, which enabled a reliable separation of the two lungs, which was an important step for correct segmentation. Segmentations were reviewed by an analyst for correctness but not

validated against manually segmented lungs. The manual segmentation of a whole lung in 3D requires the delineation of the lung contours on each slice, which is therefore error-prone and time-consuming, but could be essential to identify minor segmentation errors and to optimise the lung segmentation further. It should be noted that the segmentation was only developed using images of the same scanner and was not tested for multi-centre use. The robustness of the segmentation can be further improved in future work, for example by determining the thresholds from histograms using methods that work more robustly than peak identification.

The registration of the segmented lung mask from morphological images to the DCE-MRI data was carried out with an existing MATLAB toolbox for multimodal non-rigid demon registration. Other multimodal registrations were evaluated, such as intensity base registrations without control points (Register Multimodal MRI Images - MATLAB & Simulink Example - MathWorks Deutschland n.d.), but the robustness was lower and deformation errors occurred more frequently. The image registration was the most computationally demanding part of the analysis pipeline. The high number of parameters for the optimiser increase the accuracy of the registration but makes non-rigid registration computationally expensive.

During lung segmentation, voxels in areas affected by breathing artifacts caused by shallow breathing in the area above the diaphragm were automatically cut out of the segmented lung mask using CCA, as they substantially distort the calculation of the C(t) maps. The thresholds for the CCA were empirically determined and therefore maybe not transferable to data from other DCE-MRI sequences. Unfortunately, this method reduces the size of the segmented lungs and leads to the exclusion of entire lung areas. However, with the exclusion of voxels by CCA it was possible to evaluate data sets that would otherwise have had to be completely excluded. Alternatively, shallow breathing could be compensated by registering every time point of the

DCE-MRI data series to the first (or second) DCE-MRI timepoint, i.e. to deform the DCE-MRI images to the first (or another) time point. However, initial experiments revealed a change in the lung structure and signal intensities. The registration (and with this a deformation) of the greyscale DCE-MRI image itself led to a strong distortion of the values. In contrast, for the registration carried out in this work only the segmented lung mask, a binary image, was registered/deformed, which prevents the values of the DCE-MRI from changing due to the registration. Overall, it would be beneficial if DCE-MRI data in free-breathing could be evaluated quantitively by computer algorithms in future. For example, in children with CF, DCE-MRI cannot be acquired in breath-hold since a long-lasting breath-hold is not possible for young children or infants.

In this work, no automatic suppression of the great pulmonary vessels in the lungs was performed for PBF and PBV, as proposed by Risse et al., nor a manual exclusion by segmentation by a radiologist as proposed by Kaireit et al. (Kaireit et al. 2017; Risse et al. 2009). The exclusion of the large vessels was not performed, as both automatic and manual segmentation could potentially increase the variability of the perfusion parameters. Due to the low temporal resolution of the DCE-MRI data, the automatic and manual exclusion could result in inconsistent exclusion of vessels.

4.6 Study limitations and outlook

One major limitation of this work is the use of the same scanner in both studies. As a result, QDP, but also technical components of the quantitative assessments such as lung segmentation and registration, could not be evaluated for multi-centre suitability. Other perfusion quantification algorithms could be be more precise or more robust in future studies with different scanners and/or other DCE-MRI pulse sequences with better image quality. DCE-

MRI data quality issues in the lungs were primarily caused by the measurement technique to achieve the necessary temporal resolution (keyhole concept), the low proton density, the CA application dose, and pronounced susceptibility artifacts in the lungs. Especially in COPD, the emphysematous changes in lung parenchyma and possible hyperinflation of the lung further reduce the already low proton density in the lungs and aggravate the issues of lung MRI. A major limitation of the reproducibility study is the limited range of disease severity in the COPD population, which was introduced by recruiting patients from the hospital's outpatient clinic, mainly treating patients with severe COPD and emphysema. In this work, only COPD and CF patients have been studied. However, functional imaging of pulmonary perfusion is also of interest for other lung diseases that lead to alveolar hypoxia, such as interstitial pulmonary fibrosis or asthma.

The MRI perfusion score used in this work was chosen as reference for the development of QDP, because it has already been extensively evaluated in clinical studies and was even successfully used as a response-to-treatment biomarker demonstrating the reversibility of perfusion abnormalities after therapeutic intervention in patients with CF (Eichinger et al. 2012; Bertram J. Jobst et al. 2015; Stahl et al. 2017; Wielpütz et al. 2014; Wielpütz et al. 2018). However, it should be noted that the MRI perfusion score assessed visually by a radiologist has intra- and inter-reader variabilities and may not be able to account for subtle changes (coarse scoring of 0,1,2 per lobe) (Eichinger et al. 2012).

The long acquisition time in inspiratory breath-hold is challenging for many seriosly ill patients. For perfusion quantification, only the time points of the first CA-bolus passage through the lungs were required. The acquisition time is determined by physiology and was pre-defined because individual CA circulation times through the lungs are unknown.

The non-linearities between signal enhancement and CA concentration should be further investigated for the TWIST sequence and CA used. Based on literature and the observed signal enhancement in the main pulmonary artery, it was assumed that the used CA concentration did not exceed the linear range of the relationship between the MR signal and the CA concentration in this work. However, only a low contrast-enhancement was observed in the lung parechmya resulting in a low CNR, which potentially increases the varibility of the quantitative perfusion parameters. A higher CA dose resulting in a higher CNR in the lung parecnhyma could therefore potentially reduce the variability of the quantitative perfusion parameters. The resulting non-linearity of the signal-to-CA-concentration relationship in the AIF could be compensated mathematically for the IRF calculation, as proposed by Neeb et al. (Neeb et al. 2009). However, it must be ensured that the signal intensity and CA concentration relationship in the pulmonary parenchyma remains in the linear range.

Although multiple comparisons were evaluated, no correction for multiple-testing was performed as the individual p-values for the comparisons were considered more relevant. Since cross-sectional correlations do not prove causality, the relevance of perfusion abnormalities must be further investigated in large longitudinal studies, ideally with regional comparisons between quantitative CT and quantitative MRI data. In order to determine suitability as a response-to-treatment biomarker, it must be demonstrated in an interventional longitudinal study that QDP can either detect reversibility of perfusion defects or detect slowed progression of perfusion defects. Furthermore, its suitability as a prognostic marker must be proven in a longitudinal study, ideally without an investigational medicinal product, by examining whether regional perfusion defects precede regional, often irreversible, structural changes such as emphysema or bronchiectasis.

Several aspects of the tracer kinetics and pathophysiological changes of the concentration curves were not examined in this work. In particular, the model used did neither account for delay and dispersion of the contrast agent in C(t) nor for the recirculation of CA in $C_a(t)$ and C(t). Regional delayed or dispersed contrast enhancement in the lung parenchyma occur primarily due to pathological changes in the lungs and introduce an underestimation of PBF (Calamante et al. 2000; Risse et al. 2011). The model based on the indicator dilution theory considers only the first pass of the tracer. However, the concentration time courses can include contributions from recirculating CA, which can be recognised as a second, smaller concentration peak or an incomplete return to baseline after the first pass (Calamante 2013). Normally, these contributions are eliminated before any perfusion calculation. This can be achieved either by considering the curve only until the appearance of the recirculation or by removing the recirculation by modelling a gamma-variate function to the measured $C_a(t)$ (Calamante 2013; Davenport 1983; Thompson et al. 1964). No correction for recirculation as proposed by Calamante et al. for neuroimaging was done in this work as a fit of the recirculation in every voxel separately was not possible due to the data quality in the lungs, which is distinctly lower than in the brain (Calamante 2013). Furthermore, due to delay and dispersion a cut off time point for all voxels within the lungs was not considered suitable.

4.7 Conclusion

In conclusion, the present work shows the potential of unsupervised clustering algorithms in combination with the mathematical models of the indicator dilution theory for the detection of perfusion defects from DCE-MRI data in muco-obstructive lung diseases. A method to quantify QDP from DCE-MRI data was developed and evaluated regarding its relationship to visual MRI perfusion scoring, QCT and PFT parameters and regarding its midterm reproducibility.

The main conclusions of this thesis are:

1. QDP is strongly associated with the visual MRI perfusion score, suggesting that QDP has the potential to replace the visual assessment by the radiologist in future, which would omit inter- and intra-reader variabilities. Since QDP is determined using an automated computer algorithm, the calculation is time-efficient and allows for a more detailed assessment of perfusion abnormalities compared to visual MRI perfusion scoring.

2. In comparison, QDP showed a higher performance than PBF or PBV. QDP is more robust (reproducible) than PBF and PBV with smaller LoA and MID. As a result, smaller sample sizes and/or shorter study durations are needed when using QDP compared to PBF and PBV in future clinical studies to detect therapeutic response. QDP showed higher correlations with the MRI perfusion score, QCT and PFT parameters than PBF or PBV.

3. QDP quantified from DCE-MRI data is associated with established markers of disease severity. In detail, QDP correlated significantly with MRI perfusion score, QCT, and PFT parameters. Furthermore, the extent of perfusion defects corresponds to the combined extent of emphysema und fSAD quantified by QCT, indicating that pulmonary perfusion abnormalities themselves may contribute to, or at least precede, the development of irreversible emphysema.

QDP has the potential to be used as robust, sensitive, non-invasive, and radiation-free imaging-based biomarker for clinical studies in patients with muco-obstructive lung disease, especially as prognostic or response-to-treatment biomarker.

5   SUMMARY

Pulmonary perfusion is regionally impaired in muco-obstructive lung diseases such as cystic fibrosis (CF) and chronic obstructive pulmonary disease (COPD) due to the destruction of the alveolar-capillary bed and hypoxic pulmonary vasoconstriction in response to alveolar hypoxia. Dynamic contrast-enhanced magnetic resonance imaging (DCE-MRI) is an established technique for assessing regional perfusion abnormalities by exploiting contrast enhancement in the lung parenchyma during the first pass of an intravenously injected contrast agent bolus. Typically, perfusion abnormalities are assessed in clinical studies by visual scoring or by quantifying pulmonary blood flow (PBF) and pulmonary blood volume (PBV). Automated quantification can help to address inter-reader variability issues with human reader, facilitate detailed perfusion analyses and is time efficient. However, currently used absolute quantification of PBF and PBV is highly variable. For this reason, an algorithm was developed to quantify the extent of pulmonary perfusion in percent (QDP) using unsupervised clustering algorithms, which leads to an intrinsic normalisation and can reduce variability compared to absolute perfusion quantification. The aims of this work were to develop a robust algorithm for quantifying QDP, to investigate the midterm reproducibility of QDP, and to validate QDP using MRI perfusion scoring, quantitative computed tomography (CT) parameters, and pulmonary function testing (PFT) parameters. Furthermore, the performance of QDP was compared to the performance of PBF and PBV.

The development of QDP and its technical and clinical validation were performed using data from two studies, which utilise DCE-MRI. First, the algorithm was developed using data of 83 COPD subjects from the 'COSYCONET' COPD cohort by comparing different unsupervised clustering approaches including Otsu´s method, k-means clustering, and 80th percentile threshold. Second, the reproducibility of QDP was investigated using data from a study of 15 CF and 20 COPD patients who underwent DCE-MRI at baseline and one month later

(reproducibility study). According to the indicator dilution theory, impulse response function maps were calculated from DCE-MRI data, which formed the basis for the quantification of QDP, PBF and PBV.

Overall, QDP based on Otsu´s method showed the highest agreement with the MRI perfusion score, quantitative CT parameters and PFT parameters in the COSYCONET study and was therefore selected for further evaluations. QDP correlated moderately with the MRI perfusion score in CF ($r=0.46$, $p<0.05$) and moderately to strongly in COPD ($r=0.66$ and $r=0.72$, $p<0.001$) in both studies. PBF and PBV correlated poorly with the MRI perfusion score in CF ($r=-0.29$, $p=0.132$ and $r=-0.35$, $p=0.067$, respectively) and moderately in COPD ($r=-0.49$ to -0.57, $p<0.001$). QDP correlated strongly with the CT parameter for emphysema ($r=0.74$, $p<0.001$) and weakly with the CT parameter for functional small airway disease ($r=0.35$, $p<0.001$) in COPD. The extent of perfusion defects from DCE-MRI corresponded to extent of abnormal lung (emphysema+functional small airway disease) from CT, with a mean difference of 6.03 ± 16.94. QDP correlated moderately with PFT parameters in both studies and patient groups, with one exception in the reproducibility study where no correlation was observed in the COPD group. The use of unsupervised clustering approaches increased the reproducibility ($\pm1.96SD$ related to the median) of QDP (CF: $\pm38\%$, COPD: $\pm37\%$) compared to PBF(CF: $\pm89\%$, COPD: $\pm55\%$) and PBV(CF: $\pm55\%$, COPD: $\pm51\%$) and reduced outliers.

These results demonstrate that the quantification of pulmonary perfusion using unsupervised clustering approaches in combination with the mathematical models of the indicator dilution theory improves the reproducibility and the correlations with visual MRI perfusion scoring, quantitative CT parameters and PFT parameters. QDP based on Otsu´s method showed high agreement with the MRI perfusion score, suggesting that in future clinical studies pulmonary perfusion can be assessed objectively by computer algorithms replacing the time-consuming visual scoring. Concordance between the extent of QDP from MRI and the extent of abnormal

lung from CT indicates that pulmonary perfusion abnormalities themselves may contribute to, or at least precede, the development of irreversible emphysema. The findings of both studies show that QDP is clinically meaningful in muco-obstructive lung diseases as it is significantly associated with the MRI perfusion score, quantitative CT parameters, and PFT parameters.

6   ZUSAMMENFASSUNG

Die Perfusion der Lunge ist bei muko-obstruktiven Lungenerkrankungen, wie zystischer Fibrose (CF) und chronisch obstruktive Lungenerkrankung (COPD), aufgrund der Zerstörung der Lungenkapillaren und aufgrund der Reaktion des Euler-Liljestrand-Mechanismus auf alveoläre Hypoxie regional beeinträchtigt. Die dynamisch kontrastmittelverstärkte Magnetresonanztomographie (DCE-MRT) ist ein etabliertes Verfahren zur Beurteilung regionaler Anomalien der pulmonalen Perfusion, indem die Kontrastverstärkung im Lungenparenchym während des ersten Durchgangs eines intravenös injizierten Kontrastmittelbolus beurteilt wird. Üblicherweise werden pulmonalen Perfusionsanomalien in klinischen Studien mittels visueller Befundung durch einen Radiologen oder mittels Computeralgorithmen, die den pulmonalen Blutfluss (PBF) und das pulmonale Blutvolumen (PBV) quantifizieren, beurteilt. Eine automatisierte Quantifizierung kann dazu beitragen, die Intra- und Inter-Reader-Variabilität zu reduzieren, ermöglicht eine detaillierte Analyse der Perfusion und ist zeitsparend. Die derzeit verwendete absolute Quantifizierung von PBF und PBV weist jedoch eine hohe Variabilität auf. Daher wurde ein Algorithmus zur Quantifizierung des Ausmaßes von pulmonalen Perfusionsdefekten in Prozent (QDP) unter Verwendung von unüberwachten Clustering-Algorithmen entwickelt, was zu einer intrinsischen Normalisierung führt und die Variabilität im Vergleich zur absoluten Perfusionsquantifizierung reduzieren kann. Die Ziele dieser Arbeit waren die Entwicklung eines robusten Algorithmus zur Quantifizierung von QDP, die Untersuchung der Reproduzierbarkeit von QDP und die Validierung von QDP unter Verwendung von MRT-Perfusions-Scoring, quantitativen Computertomographie (CT)-Parametern und Lungenfunktionstest (PFT)-Parametern. Darüber hinaus wurde die Leistung von QDP mit der von PBF und PBV verglichen.

Die Entwicklung von QDP sowie die technische und klinische Validierung erfolgte anhand von Daten aus zwei Studien, die DCE-MRT verwenden: Zunächst wurde der Algorithmus anhand

der Daten von 83 COPD-Patienten aus der nationalen COPD-Kohorte "COSYCONET" entwickelt, indem verschiedene unüberwachte Clustering-Ansätzen verglichen wurden, darunter das Verfahren von Otsu, k-means-Clustering und die 80. Perzentil-Schwelle. Als nächstes wurde die Reproduzierbarkeit von QDP in einer Studie mit 15 CF- und 20 COPD-Patienten untersucht, die eine DCE-MRT-Untersuchung zu Studienbeginn und einen Monat später umfasste (Reproduzierbarkeitsstudie). Gemäß der Indikatorverdünnungstheorie wurden Impulsantwortkarten aus den DCE-MRT-Daten berechnet, die die Grundlage für die Quantifizierung von QDP, PBF und PBV bildeten.

Insgesamt zeigte der nach dem Verfahren von Otsu berechnete QDP-Ansatz in der COSYCONET-Studie die höchste Übereinstimmung mit dem MRT-Perfusionsscore, den quantitativen CT-Parametern und den PFT-Parametern und wurde daher für weitere Untersuchungen ausgewählt. QDP korrelierte moderat mit dem MRT-Perfusionsscore bei CF (r=0,46, p<0,05) und moderat bis stark bei COPD (r=0,66 und r=0,72, p<0,001). PBF und PBV korrelierten schwach mit dem MRT-Perfusionsscore bei CF (r=-0,29, p=0,132 bzw. r=-0,35, p=0,067) und moderat bei COPD (r=-0,49 bis -0,57, p<0,001). QDP korrelierte stark mit dem quantitativen CT-Parameter für Emphysem (r=0,74, p<0,001) und schwach mit dem für funktionellen Erkrankung der kleinen Atemwege (r=0,35, p<0,001) bei COPD. Das Ausmaß von QDP auf dem MRT entsprach dem Ausmaß abnormaler Lunge (=Emphysem+funktionelle Erkrankung der kleinen Atemwege) auf dem CT mit einer mittleren Differenz von 6,03±16,94.

QDP korrelierte in beiden Studien und beiden Patientengruppen moderat mit den untersuchten PFT-Parametern, mit einer Ausnahme in der Reproduzierbarkeitsstudie, bei der keine Korrelation in der COPD-Gruppe beobachtet wurde. Die Verwendung von unüberwachten Clustering-Ansätzen erhöhte die Reproduzierbarkeit (±1,96SD bezogen auf den Median) von QDP (CF: ±38%, COPD: ±37%) im Vergleich zu PBF (CF: ±89%, COPD: ±55%) und PBV (CF: ±55%, COPD: ±51%) und reduzierte Ausreißer.

Diese Ergebnisse zeigen, dass die Quantifizierung der pulmonalen Perfusion mit Hilfe von unüberwachten Clustering-Ansätzen in Kombination mit den mathematischen Modellen der Indikatorverdünnungstheorie die Korrelationen mit dem visuellen MRT-Perfusionsscore, quantitativen CT-Parametern und PFT-Parametern sowie die Reproduzierbarkeit verbessert. QDP zeigte einen starken Zusammenhang mit dem MRT-Perfusionsscore, weshalb die pulmonale Perfusion in zukünftigen klinischen Studien objektiv durch Computeralgorithmen analysiert werden könnte und die zeitaufwändige visuelle Befundung ersetzen werden könnte. Die Übereinstimmung zwischen dem Ausmaß von Perfusionsdefekte und dem Ausmaß abnormaler Lunge deutet darauf hin, dass Veränderungen der pulmonalen Durchblutung zur Entwicklung eines irreversiblen Emphysems beitragen oder diesem vorausgehen können. Die Ergebnisse beider Studien zeigen, dass QDP aufgrund seiner signifikanten Assoziationen mit dem MRT-Perfusionsscore, den quantitativen CT-Parametern und den PFT-Parametern bei muko-obstruktiven Lungenerkrankungen klinisch bedeutsam ist.

7 BIBILIOGRAPY

Aarli, B. B., Calverley, P. M. A., Jensen, R. L., Eagan, T. M. L., Bakke, P. S. and Hardie, J. A. (2015). **Variability of within-breath reactance in COPD patients and its association with dyspnoea**. Eur Respir J *45*, 625–634, doi:10.1183/09031936.00051214.

Alberich-Bayarri, A., Sourbron, S., Golay, X., deSouza, N., Smits, M., Lugt, A. van der, Boellard, R. and European_Society_of_Radiology (2020). **ESR Statement on the Validation of Imaging Biomarkers**. Insights Imaging *11*, 76, doi:10.1186/s13244-020-00872-9.

Alford, S. K., Beek, E. J. van, McLennan, G. and Hoffman, E. A. (2010). **Heterogeneity of pulmonary perfusion as a mechanistic image-based phenotype in emphysema susceptible smokers**. Proc Natl Acad Sci U S A *107*, 7485–7490, doi:10.1073/pnas.0913880107.

Altes, T. A., Johnson, M., Fidler, M., Botfield, M., Tustison, N. J., Leiva-Salinas, C., Lange, E. E. de, Froh, D. and Mugler, J. P. (2017). **Use of hyperpolarized helium-3 MRI to assess response to ivacaftor treatment in patients with cystic fibrosis**. J Cyst Fibros *16*, 267–274, doi:10.1016/j.jcf.2016.12.004.

Barbera, J. A., Ramirez, J., Roca, J., Wagner, P. D., Sanchez-Lloret, J. and Rodriguez-Roisin, R. (1990). **Lung Structure and Gas Exchange in Mild Chronic Obstructive Pulmonary Disease**. Am Rev Respir Dis *141*, 895–901, doi:10.1164/ajrccm/141.4_pt_1.895.

Bauman, G., Puderbach, M., Heimann, T., Kopp-Schneider, A., Fritzsching, E., Mall, M. A. and Eichinger, M. (2013). **Validation of Fourier decomposition MRI with dynamic contrast-enhanced MRI using visual and automated scoring of pulmonary perfusion in young cystic fibrosis patients**. Eur J Radiol *82*, 2371–2377, doi:10.1016/j.ejrad.2013.08.018.

Bell, L. C., Wang, K., Rio, A. M. D., Grist, T. M., Fain, S. B. and Nagle, S. K. (2015). **Comparison of Models and Contrast Agents for Improved Signal and Signal Linearity in Dynamic Contrast-Enhanced Pulmonary Magnetic Resonance Imaging**. Invest Radiol *50*, 174–178, doi:10.1097/rli.0000000000000122.

BEST (Biomarkers, EndpointS, and other Tools) Resource - NCBI Bookshelf (2016). 2016, URL: https://www.ncbi.nlm.nih.gov/books/NBK326791/ [Accessed August 2021].

Boes, J. L., Hoff, B. A., Bule, M., Johnson, T. D., Rehemtulla, A., Chamberlain, R., Hoffman, E. A., Kazerooni, E. A., Martinez, F. J., Han, M. K., Ross, B. D. and Galbán, C. J. (2015). **Parametric Response Mapping Monitors Temporal Changes on Lung CT Scans in the Subpopulations and Intermediate Outcome Measures in COPD Study (SPIROMICS)**. Acad Radiol *22*, 186–194, doi:10.1016/j.acra.2014.08.015.

Boucher, R. C. (2019). **Muco-Obstructive Lung Diseases**. New Engl J Med *380*, 1941–1953, doi:10.1056/nejmra1813799.

Brabandt, H. V., Cauberghs, M., Verbeken, E., Moerman, P., Lauweryns, J. M. and Woestijne, K. P. V. de (1983). **Partitioning of pulmonary impedance in excised human and canine lungs**. J Appl Physiol *55*, 1733–1742, doi:10.1152/jappl.1983.55.6.1733.

Brown, R. W., Cheng, Y.-C. N., Haacke, E. M., Thompson, M. R. and Venkatesan, R. (2014). Magnetic Resonance Imaging: Physical Principles and Sequence Design, Second Edition, doi:DOI:10.1002/9781118633953.

Cachier, P., Pennec, X. and Ayache, N. (1999). **Fast Non Rigid Matching by Gradient Descent: Study and Improvements of the "Demons" Algorithm**. Technical Report INRIA, RR-3706.

Calamante, F. (2013). **Arterial input function in perfusion MRI: A comprehensive review**. Prog Nucl Mag Res Sp *74*, 1–32, doi:10.1016/j.pnmrs.2013.04.002.

Calamante, F., Gadian, D. G. and Connelly, A. (2000). **Delay and dispersion effects in dynamic susceptibility contrast MRI: Simulations using singular value decomposition**. Magnet Reson Med *44*, 466–473, doi:10.1002/1522-2594(200009)44:3<466::aid-mrm18>3.0.co;2-m.

Calamante, F., Thomas, D. L., Pell, G. S., Wiersma, J. and Turner, R. (1999). **Measuring Cerebral Blood Flow Using Magnetic Resonance Imaging Techniques**. J Cereb Blood Flow Metabolism *19*, 701–735, doi:10.1097/00004647-199907000-00001.

Capaldi, D. P. I., Eddy, R. L., Svenningsen, S., Guo, F., Baxter, J. S. H., McLeod, A. J., Nair, P., McCormack, D. G., Parraga, G. and Network, F. the C. R. R. (2018). **Free-breathing Pulmonary MR Imaging to Quantify Regional Ventilation**. Radiology *287*, 693–704, doi:10.1148/radiol.2018171993.

CHMP (2012a). Guideline on clinical investigation of medicinal products in the treatment of chronic obstructive pulmonary disease (COPD).

CHMP (2012b). Report of the workshop on endpoints for cystic fibrosis clinical trials.

CMPH (2009). Guideline on the clinical development of medicinal products for the treatment of cystic fibrosis.

Couch, M. J., Thomen, R., Kanhere, N., Hu, R., Ratjen, F., Woods, J. and Santyr, G. (2019). **A two-center analysis of hyperpolarized 129Xe lung MRI in stable pediatric cystic fibrosis: Potential as a biomarker for multi-site trials**. J Cyst Fibros *18*, 728–733, doi:10.1016/j.jcf.2019.03.005.

Cystic Fibrosis Foundation (2019). Understanding Changes in Life Expectancy, 2019, URL: https://www.cff.org/Research/Researcher-Resources/Patient-Registry/Understanding-Changes-in-Life-Expectancy/ [Accessed July 2021].

Cystic Fibrosis Foundation Patient Registry (2019)., URL: https://www.cff.org/Research/Researcher-Resources/Patient-Registry/2019-Patient-Registry-Annual-Data-Report.pdf.

Davenport, R. (1983). **The derivation of the gamma-variate relationship for tracer dilution curves.** J Nucl Medicine Official Publ Soc Nucl Medicine *24*, 945–948.

Diedenhofen, B. and Musch, J. (2015). **cocor: A Comprehensive Solution for the Statistical Comparison of Correlations**. Plos One *10*, e0121945, doi:10.1371/journal.pone.0121945.

Dransfield, M. T., Wilhelm, A. M., Flanagan, B., Courville, C., Tidwell, S. L., Raju, S. V., Gaggar, A., Steele, C., Tang, L. P., Liu, B. and Rowe, S. M. (2013). **Acquired Cystic Fibrosis Transmembrane Conductance Regulator Dysfunction in the Lower Airways in COPD**. Chest *144*, 498–506, doi:10.1378/chest.13-0274.

Duhamel, G., Schlaug, G. and Alsop, D. C. (2006). **Measurement of arterial input functions for dynamic susceptibility contrast magnetic resonance imaging using echoplanar images: Comparison of physical simulations with in vivo results**. Magnet Reson Med *55*, 514–523, doi:10.1002/mrm.20802.

Eichinger, M., Optazaite, D. E., Kopp-Schneider, A., Hintze, C., Biederer, J., Niemann, A., Mall, M. A., Wielputz, M. O., Kauczor, H. U. and Puderbach, M. (2012). **Morphologic and functional scoring of cystic fibrosis lung disease using MRI**. Eur J Radiol *81*, 1321–1329, doi:10.1016/j.ejrad.2011.02.045.

Euler, U. S. v. and Liljestrand, G. (1946). **Observations on the Pulmonary Arterial Blood Pressure in the Cat**. Acta Physiol Scand *12*, 301–320, doi:10.1111/j.1748-1716.1946.tb00389.x.

Fink, C., Ley, S., Kroeker, R., Requardt, M., Kauczor, H.-U. and Bock, M. (2005a). **Time-resolved contrast-enhanced three-dimensional magnetic resonance angiography of the chest: combination of parallel imaging with view sharing (TREAT).** Invest Radiol *40*, 40–48.

Fink, C., Ley, S., Risse, F., Eichinger, M., Zaporozhan, J., Buhmann, R., Puderbach, M., Plathow, C. and Kauczor, H.-U. (2005b). **Effect of Inspiratory and Expiratory Breathhold on Pulmonary Perfusion: assessment by pulmonary perfusion magnetic resonance imaging**. Invest Radiol *40*, 72–79, doi:10.1097/01.rli.0000149252.42679.78.

Fink, C., Puderbach, M., Ley, S., Zaporozhan, J., Plathow, C. and Kauczor, H.-U. (2005c). **Time-resolved echo-shared parallel MRA of the lung: observer preference study of image quality in comparison with non-echo-shared sequences**. Eur Radiol *15*, 2070–2074, doi:10.1007/s00330-005-2831-9.

Fuchs, H. J., Borowitz, D. S., Christiansen, D. H., Morris, E. M., Nash, M. L., Ramsey, B. W., Rosenstein, B. J., Smith, A. L. and Wohl, M. E. (1994). **Effect of Aerosolized Recombinant Human DNase on Exacerbations of Respiratory Symptoms and on Pulmonary Function in Patients with Cystic Fibrosis**. New Engl J Medicine *331*, 637–642, doi:10.1056/nejm199409083311003.

Galbán, C. J., Han, M. K., Boes, J. L., Chughtai, K. A., Meyer, C. R., Johnson, T. D., Galbán, S., Rehemtulla, A., Kazerooni, E. A., Martinez, F. J. and Ross, B. D. (2012). **Computed tomography–based biomarker provides unique signature for diagnosis of COPD phenotypes and disease progression**. Nat Med *18*, 1711–1715, doi:10.1038/nm.2971.

Graeber, S. Y., Hug, M. J., Sommerburg, O., Hirtz, S., Hentschel, J., Heinzmann, A., Dopfer, C., Schulz, A., Mainz, J. G., Tümmler, B. and Mall, M. A. (2015). **Intestinal Current Measurements Detect Activation of Mutant CFTR in Patients with Cystic Fibrosis with the G551D Mutation Treated with Ivacaftor**. Am J Resp Crit Care *192*, 1252–1255, doi:10.1164/rccm.201507-1271le.

Graham, B. L., Steenbruggen, I., Miller, M. R., Barjaktarevic, I. Z., Cooper, B. G., Hall, G. L., Hallstrand, T. S., Kaminsky, D. A., McCarthy, K., McCormack, M. C., Oropez, C. E., Rosenfeld, M., Stanojevic, S., Swanney, M. P. and Thompson, B. R. (2019). **Standardization of Spirometry 2019 Update. An Official American Thoracic Society and European Respiratory Society Technical Statement**. Am J Resp Crit Care *200*, e70–e88, doi:10.1164/rccm.201908-1590st.

Griswold, M. A., Jakob, P. M., Heidemann, R. M., Nittka, M., Jellus, V., Wang, J., Kiefer, B. and Haase, A. (2002). **Generalized autocalibrating partially parallel acquisitions (GRAPPA)**. Magnet Reson Med *47*, 1202–1210, doi:10.1002/mrm.10171.

Gudbjartsson, H. and Patz, S. (1995). **The rician distribution of noisy mri data**. Magnet Reson Med *34*, 910–914, doi:10.1002/mrm.1910340618.

Gust, R., Kozlowski, J., Stephenson, A. H. and Schuster, D. P. (1998). **Synergistic Hemodynamic Effects of Low-dose Endotoxin and Acute Lung Injury**. Am J Resp Crit Care *157*, 1919–1926, doi:10.1164/ajrccm.157.6.9704110.

Haase, A., Frahm, J., Matthaei, D., Hanicke, W. and Merboldt, K.-D. (1986). **FLASH imaging. Rapid NMR imaging using low flip-angle pulses**. J Magnetic Reson 1969 *67*, 258–266, doi:10.1016/0022-2364(86)90433-6.

Han, M. K., Agusti, A., Calverley, P. M., Celli, B. R., Criner, G., Curtis, J. L., Fabbri, L. M., Goldin, J. G., Jones, P. W., MacNee, W., Make, B. J., Rabe, K. F., Rennard, S. I., Sciurba, F. C., Silverman, E. K., Vestbo, J., Washko, G. R., Wouters, E. F. M. and Martinez, F. J. (2010). **Chronic Obstructive Pulmonary Disease Phenotypes**. Am J Resp Crit Care *182*, 598–604, doi:10.1164/rccm.200912-1843cc.

Hansen, P. C. (1987). **The truncatedSVD as a method for regularization**. BIT Numerical Mathematics *27*, 534–553, doi:10.1007/bf01937276.

Hansen, P. C. (1998). **Rank-Deficient and Discrete Ill-Posed Problems**. Society for Industrial and Applied Mathematics 215–247, doi:10.1137/1.9780898719697.bm.

Hansen, P. C. (2016). 2016 regtools - MATLAB Central File Exchange, , URL: https://de.mathworks.com/matlabcentral/fileexchange/52-regtools?focused=743860fe-66ce-3cb4-29c3-5b1d46794b3e&tab=function [Accessed January 2018].

Haralick, R. M. and Shapiro, L. G. (1992). Computer and Robot Vision, 1st Ed., Addison-Wesley Longman Publishing Co., Inc., USA.

Hatabu, H., Alsop, D. C., Listerud, J., Bonnet, M. and Gefter, W. B. (1999a). **T2* and proton density measurement of normal human lung parenchyma using submillisecond echo time gradient echo magnetic resonance imaging**. Eur J Radiol *29*, 245–252, doi:10.1016/s0720-048x(98)00169-7.

Hatabu, H., Tadamura, E., Levin, D. L., Chen, Q., Li, W., Kim, D., Prasad, P. V. and Edelman, R. R. (1999b). **Quantitative assessment of pulmonary perfusion with dynamic contrast-enhanced MRI**. Magnet Reson Med *42*, 1033–1038, doi:10.1002/(sici)1522-2594(199912)42:6<1033::aid-mrm7>3.0.co;2-7.

Heimann, T., Eichinger, M., Bauman, G., Bischoff, A., Puderbach, M. and Meinzer, H.-P. (2012). **Automated scoring of regional lung perfusion in children from contrast enhanced 3D MRI**. Proc Spie 83150U-83150U – 6, doi:10.1117/12.911946.

Heitzman, E. R., Markarian, B., Berger, I. and Dailey, E. (1969). **The Secondary Pulmonary Lobule: A Practical Concept for Interpretation of Chest Radiographs: I. Roentgen Anatomy of the Normal Secondary Pulmonary Lobule**. Radiology *93*, 507–512, doi:10.1148/93.3.507.

Hennig, J., Scheffler, K., Laubenberger, J. and Strecker, R. (1997). **Time-resolved projection angiography after bolus injection of contrast agent**. Magnet Reson Med *37*, 341–345, doi:10.1002/mrm.1910370306.

Hirtz, S., Gonska, T., Seydewitz, H. H., Thomas, J., Greiner, P., Kuehr, J., Brandis, M., Eichler, I., Rocha, H., Lopes, A., Barreto, C., Ramalho, A., Amaral, M. D., Kunzelmann, K. and Mall, M. (2004). **CFTR Cl− channel function in native human colon correlates with the genotype and phenotype in cystic fibrosis**. Gastroenterology *127*, 1085–1095, doi:10.1053/j.gastro.2004.07.006.

Hoffman, E. A., Simon, B. A. and McLennan, G. (2006). **State of the Art. A structural and functional assessment of the lung via multidetector-row computed tomography: phenotyping chronic obstructive pulmonary disease**. Proceedings of the American Thoracic Society *3*, 519–532, doi:10.1513/pats.200603-086ms.

Hogg, J. C., Chu, F., Utokaparch, S., Woods, R., Elliott, W. M., Buzatu, L., Cherniack, R. M., Rogers, R. M., Sciurba, F. C., Coxson, H. O. and Paré, P. D. (2004). **The Nature of Small-Airway Obstruction in Chronic Obstructive Pulmonary Disease**. New Engl J Medicine *350*, 2645–2653, doi:10.1056/nejmoa032158.

Hogg, J. C., Macklem, P. T. and Thurlbeck, W. M. (1968). **Site and Nature of Airway Obstruction in Chronic Obstructive Lung Disease**. New Engl J Medicine *278*, 1355–1360, doi:10.1056/nejm196806202782501.

Hogg, J. C. and Timens, W. (2009). **The Pathology of Chronic Obstructive Pulmonary Disease**. Annu Rev Pathology Mech Dis *4*, 435–459, doi:10.1146/annurev.pathol.4.110807.092145.

Hoo, A.-F., Thia, L. P., Nguyen, T. T. D., Bush, A., Chudleigh, J., Lum, S., Ahmed, D., Lynn, I. B., Carr, S. B., Chavasse, R. J., Costeloe, K. L., Price, J., Shankar, A., Wallis, C., Wyatt, H. A., Wade, A., Stocks, J. and Collaboration, L. C. F. (2012). **Lung function is abnormal in 3-month-old infants with cystic fibrosis diagnosed by newborn screening**. Thorax *67*, 874, doi:10.1136/thoraxjnl-2012-201747.

Hueper, K., Parikh, M. A., Prince, M. R., Schoenfeld, C., Liu, C., Bluemke, D. A., Dashnaw, S. M., Goldstein, T. A., Hoffman, E. A., Lima, J. A., Skrok, J., Zheng, J., Barr, R. G. and Vogel-Claussen, J. (2013). **Quantitative and semiquantitative measures of regional pulmonary microvascular perfusion by magnetic resonance imaging and their relationships to global lung perfusion and lung diffusing capacity: the multiethnic study of atherosclerosis chronic obstructive pulmonary disease study**. Invest Radiol *48*, 223–230, doi:10.1097/rli.0b013e318281057d.

Hueper, K., Vogel-Claussen, J., Parikh, M. A., Austin, J. H., Bluemke, D. A., Carr, J., Choi, J., Goldstein, T. A., Gomes, A. S., Hoffman, E. A., Kawut, S. M., Lima, J., Michos, E. D., Post, W. S., Po, M. J., Prince, M. R., Liu, K., Rabinowitz, D., Skrok, J., Smith, B. M., Watson, K., Yin, Y., Zambeli-Ljepovic, A. M. and Barr, R. G. (2015). **Pulmonary Microvascular Blood Flow in Mild Chronic Obstructive Pulmonary Disease and Emphysema. The MESA COPD Study**. Am J Respir Crit Care Med *192*, 570–580, doi:10.1164/rccm.201411-2120oc.

Ingrisch, M., Dietrich, O., Attenberger, U. I., Nikolaou, K., Sourbron, S., Reiser, M. F. and Fink, C. (2010). **Quantitative Pulmonary Perfusion Magnetic Resonance Imaging**. Invest Radiol *45*, 7–14, doi:10.1097/rli.0b013e3181bc2d0c.

Ingrisch, M., Maxien, D., Schwab, F., Reiser, M. F., Nikolaou, K. and Dietrich, O. (2014). **Assessment of Pulmonary Perfusion With Breath-Hold and Free-Breathing Dynamic Contrast-Enhanced Magnetic Resonance Imaging**. Invest Radiol *49*, 382–389, doi:10.1097/rli.0000000000000020.

Ishizawa, K., Kubo, H., Yamada, M., Kobayashi, S., Numasaki, M., Ueda, S., Suzuki, T. and Sasaki, H. (2004). **Bone marrow-derived cells contribute to lung regeneration after elastase-induced pulmonary emphysema**. Febs Lett *556*, 249–252, doi:10.1016/s0014-5793(03)01399-1.

Jakob, P. M., Hillenbrand, C. M., Wang, T., Schultz, G., Hahn, D. and Haase, A. (2001). **Rapid quantitative lung 1H T1 mapping**. J Magn Reson Imaging *14*, 795–799, doi:10.1002/jmri.10024.

Jobst, B. J., Triphan, S. M. F., Sedlaczek, O., Anjorin, A., Kauczor, H. U., Biederer, J., Ley-Zaporozhan, J., Ley, S. and Wielputz, M. O. (2015). **Functional lung MRI in chronic obstructive pulmonary disease: comparison of T1 mapping, oxygen-enhanced T1 mapping and dynamic contrast enhanced perfusion**. PloS one *10*, e0121520, doi:10.1371/journal.pone.0121520.

Jobst, Bertram J., Wielpütz, M. O., Triphan, S. M. F., Anjorin, A., Ley-Zaporozhan, J., Kauczor, H.-U., Biederer, J., Ley, S. and Sedlaczek, O. (2015). **Morpho-Functional 1H-MRI of the Lung in COPD: Short-Term Test-Retest Reliability**. Plos One *10*, e0137282, doi:10.1371/journal.pone.0137282.

Jörres, R., Welte, T., Bals, R., Koch, A., Schnoor, M. and Vogelmeier, C. (2010). **Einfluss systemischer Manifestationen und Komorbiditäten auf den klinischen Zustand und den Verlauf bei COPD**. Dmw - Deutsche Medizinische Wochenschrift *135*, 446–449, doi:10.1055/s-0030-1249185.

Kaireit, T. F., Gutberlet, M., Voskrebenzev, A., Freise, J., Welte, T., Hohlfeld, J. M., Wacker, F. and Vogel-Claussen, J. (2018). **Comparison of quantitative regional ventilation-weighted fourier decomposition MRI with dynamic fluorinated gas washout MRI and lung function testing in COPD patients**. J Magn Reson Imaging *47*, 1534–1541, doi:10.1002/jmri.25902.

Kaireit, T. F., Sorrentino, S. A., Renne, J., Schoenfeld, C., Voskrebenzev, A., Gutberlet, M., Schulz, A., Jakob, P. M., Hansen, G., Wacker, F., Welte, T., Tummler, B. and Vogel-Claussen, J. (2017). **Functional lung MRI for regional monitoring of patients with cystic fibrosis**. PloS one *12*, e0187483, doi:10.1371/journal.pone.0187483.

Kaireit, T. F., Voskrebenzev, A., Gutberlet, M., Freise, J., Jobst, B., Kauczor, H., Welte, T., Wacker, F. and Vogel-Claussen, J. (2019). **Comparison of quantitative regional perfusion-weighted phase resolved functional lung (PREFUL) MRI with dynamic gadolinium-enhanced regional pulmonary perfusion MRI in COPD patients**. J Magn Reson Imaging *49*, 1122–1132, doi:10.1002/jmri.26342.

Karlik, S. J. (2003). **Exploring and Summarizing Radiologic Data**. Am J Roentgenol *180*, 47–54, doi:10.2214/ajr.180.1.1800047.

Kirby, M., Heydarian, M., Svenningsen, S., Wheatley, A., McCormack, D. G., Etemad-Rezai, R. and Parraga, G. (2012). **Hyperpolarized 3He Magnetic Resonance Functional Imaging Semiautomated Segmentation**. Acad Radiol *19*, 141–152, doi:10.1016/j.acra.2011.10.007.

Kirby, M., Wheatley, A., McCormack, D. G. and Parraga, G. (2010). **Development and application of methods to quantify spatial and temporal hyperpolarized 3He MRI ventilation dynamics: preliminary results in chronic obstructive pulmonary disease**. P Soc Photo-opt Ins 762605-762605–762609, doi:10.1117/12.843821.

Kittler, J. and Illingworth, J. (1985). **On threshold selection using clustering criteria**. Ieee Transactions Syst Man Cybern *SMC-15*, 652–655, doi:10.1109/tsmc.1985.6313443.

Knowles, M., Gatzy, J. and Boucher, R. (1981). **Increased Bioelectric Potential Difference across Respiratory Epithelia in Cystic Fibrosis**. New Engl J Medicine *305*, 1489–1495, doi:10.1056/nejm198112173052502.

Kohlmann, P., Laue, H., Krass, S. and Peitgen, H.-O. (2011). 2011 Fully-Automatic Determination of the Arterial Input Function for Dynamic Contrast-Enhanced Pulmonary MR Imaging, , URL: http://www.bmva.org/miua/2011/miua-11-43.pdf [Accessed September 2020].

Kohlmann, P., Strehlow, J., Jobst, B., Krass, S., Kuhnigk, J.-M., Anjorin, A., Sedlaczek, O., Ley, S., Kauczor, H.-U. and Wielpütz, M. O. (2015). **Automatic lung segmentation method for MRI-based lung perfusion studies of patients with chronic obstructive pulmonary disease**. Int J Comput Ass Rad *10*, 403–417, doi:10.1007/s11548-014-1090-0.

Konietzke, P., Wielpütz, M. O., Wagner, W. L., Wuennemann, F., Kauczor, H.-U., Heussel, C. P., Eichinger, M., Eberhardt, R., Gompelmann, D. and Weinheimer, O. (2020). **Quantitative CT detects progression in COPD patients with severe emphysema in a 3-month interval**. Eur Radiol *30*, 2502–2512, doi:10.1007/s00330-019-06577-y.

Kroon, D.-J. (2010). 2010 Multimodality non-rigid demon algorithm image registration, , URL: https://de.mathworks.com/matlabcentral/fileexchange/21451-multimodality-non-rigid-demon-algorithm-image-registration [Accessed 2018].

Kroon, D.-J. and Slump, C. H. (2009). **MRI modalitiy transformation in demon registration**. 2009 Ieee Int Symposium Biomed Imaging Nano Macro 963–966, doi:10.1109/isbi.2009.5193214.

Labaki, W. W., Gu, T., Murray, S., Hatt, C. R., Galbán, C. J., Ross, B. D., Martinez, C. H., Curtis, J. L., Hoffman, E. A., Pompe, E., Lynch, D. A., Kazerooni, E. A., Martinez, F. J. and Han, M. K. (2019). **Voxel-Wise Longitudinal Parametric Response Mapping Analysis of Chest Computed Tomography in Smokers**. Acad Radiol *26*, 306–312, doi:10.1016/j.acra.2019.02.003.

Larsen, R. and Ziegenfuß, T. (2004). **Beatmung, Grundlagen und Praxis**. Springer-Verlag 19–58, doi:10.1007/978-3-662-06009-4_2.

Laub, G. and Kroeker, R. (2006). 2006 syngo TWIST for Dynamic Time-Resolved MR Angiography, , URL: https://cdn0.scrvt.com/39b415fb07de4d9656c7b516d8e2d907/1800000000014147/bef267b130b0/syngo_TWIST_Laub_1800000000014147.pdf [Accessed September 2021].

Lee, S. U., Chung, S. Y. and Park, R. H. (1990). **A comparative performance study of several global thresholding techniques for segmentation**. Comput Vis Graph Image Process *52*, 171–190, doi:10.1016/0734-189x(90)90053-x.

Ley, S. and Ley-Zaporozhan, J. (2011). **Pulmonary perfusion imaging using MRI: clinical application**. Insights Imaging *3*, 61–71, doi:10.1007/s13244-011-0140-1.

Ley-Zaporozhan, J., Ley, S., Eberhardt, R., Weinheimer, O., Fink, C., Puderbach, M., Eichinger, M., Herth, F. and Kauczor, H. U. (2007). **Assessment of the relationship between lung parenchymal destruction and impaired pulmonary perfusion on a lobar level in patients with emphysema**. Eur J Radiol *63*, 76–83, doi:10.1016/j.ejrad.2007.01.020.

Ley-Zaporozhan, J., Molinari, F., Risse, F., Puderbach, M., Schenk, J. P., Kopp-Schneider, A., Kauczor, H. U. and Ley, S. (2011). **Repeatability and reproducibility of quantitative whole-lung perfusion magnetic resonance imaging**. J Thoracic Imaging *26*, 230–239, doi:10.1097/rti.0b013e3181e48c36.

Lozano, R., Naghavi, M., Foreman, K., Lim, S., Shibuya, K., Aboyans, V., Abraham, J., Adair, T., Aggarwal, R., Ahn, S. Y., AlMazroa, M. A., Alvarado, M., Anderson, H. R., Anderson, L. M.,

Andrews, K. G., Atkinson, C., Baddour, L. M., Barker-Collo, S., Bartels, D. H., Bell, M. L., Benjamin, E. J., Bennett, D., Bhalla, K., Bikbov, B., Abdulhak, A. B., Birbeck, G., Blyth, F., Bolliger, I., Boufous, S., Bucello, C., Burch, M., Burney, P., Carapetis, J., Chen, H., Chou, D., Chugh, S. S., Coffeng, L. E., Colan, S. D., Colquhoun, S., Colson, K. E., Condon, J., Connor, M. D., Cooper, L. T., Corriere, M., Cortinovis, M., Vaccaro, K. C. de, Couser, W., Cowie, B. C., Criqui, M. H., Cross, M., Dabhadkar, K. C., Dahodwala, N., Leo, D. D., Degenhardt, L., Delossantos, A., Denenberg, J., Jarlais, D. C. D., Dharmaratne, S. D., Dorsey, E. R., Driscoll, T., Duber, H., Ebel, B., Erwin, P. J., Espindola, P., Ezzati, M., Feigin, V., Flaxman, A. D., Forouzanfar, M. H., Fowkes, F. G. R., Franklin, R., Fransen, M., Freeman, M. K., Gabriel, S. E., Gakidou, E., Gaspari, F., Gillum, R. F., Gonzalez-Medina, D., Halasa, Y. A., Haring, D., Harrison, J. E., Havmoeller, R., Hay, R. J., Hoen, B., Hotez, P. J., Hoy, D., Jacobsen, K. H., James, S. L., Jasrasaria, R., Jayaraman, S., Johns, N., Karthikeyan, G., Kassebaum, N., Keren, A., Khoo, J.-P., Knowlton, L. M., Kobusingye, O., Koranteng, A., Krishnamurthi, R., Lipnick, M., Lipshultz, S. E., Ohno, S. L., Mabweijano, J., MacIntyre, M. F., Mallinger, L., March, L., Marks, G. B., Marks, R., Matsumori, A., Matzopoulos, R., Mayosi, B. M., McAnulty, J. H., McDermott, M. M., McGrath, J., Memish, Z. A., Mensah, G. A., Merriman, T. R., Michaud, C., Miller, M., Miller, T. R., Mock, C., Mocumbi, A. O., Mokdad, A. A., Moran, A., Mulholland, K., Nair, M. N., Naldi, L., Narayan, K. M. V., Nasseri, K., Norman, P., O'Donnell, M., Omer, S. B., Ortblad, K., Osborne, R., Ozgediz, D., Pahari, B., Pandian, J. D., Rivero, A. P., Padilla, R. P., Perez-Ruiz, F., Perico, N., Phillips, D., Pierce, K., Pope, C. A., Porrini, E., Pourmalek, F., Raju, M., Ranganathan, D., Rehm, J. T., Rein, D. B., Remuzzi, G., Rivara, F. P., Roberts, T., León, F. R. D., Rosenfeld, L. C., Rushton, L., Sacco, R. L., Salomon, J. A., Sampson, U., Sanman, E., Schwebel, D. C., Segui-Gomez, M., Shepard, D. S., Singh, D., Singleton, J., Sliwa, K., Smith, E., Steer, A., Taylor, J. A., Thomas, B., Tleyjeh, I. M., Towbin, J. A., Truelsen, T., Undurraga, E. A., Venketasubramanian, N., Vijayakumar, L., Vos, T., Wagner, G. R., Wang, M., Wang, W., Watt, K., Weinstock, M. A., Weintraub, R., Wilkinson, J. D., Woolf, A. D., Wulf, S., Yeh, P.-H., Yip, P., Zabetian, A., Zheng, Z.-J., Lopez, A. D. and Murray, C. J. (2013). **Global and regional mortality from 235 causes of death for 20 age groups in 1990 and 2010: a systematic analysis for the Global Burden of Disease Study 2010**. Lancet *380*, 2095–2128, doi:10.1016/s0140-6736(12)61728-0.

Macklem, P. T. and Mead, J. (1967). **Resistance of central and peripheral airways measured by a retrograde catheter**. J Appl Physiol *22*, 395–401, doi:10.1152/jappl.1967.22.3.395.

Mall, M. A. (2016). **Unplugging Mucus in Cystic Fibrosis and Chronic Obstructive Pulmonary Disease**. Annals of the American Thoracic Society *13 Suppl 2*, S177-85, doi:10.1513/annalsats.201509-641kv.

Mathew, L., Kirby, M., Etemad-Rezai, R., Wheatley, A., McCormack, D. G. and Parraga, G. (2011). **Hyperpolarized 3He magnetic resonance imaging: Preliminary evaluation of phenotyping potential in chronic obstructive pulmonary disease**. Eur J Radiol *79*, 140–146, doi:10.1016/j.ejrad.2009.10.028.

Maxien, D., Ingrisch, M., Meinel, F., Reiser, M., Dietrich, O. and Nikolaou, K. (2013). **Quantification of Pulmonary Perfusion with Free-Breathing Dynamic Contrast-Enhanced MRI? A Pilot Study in Healthy Volunteers**. Fortschritte Auf Dem Gebiet Der R Ntgenstrahlen Und Der Bildgebenden Verfahren *185*, 1175–1181, doi:10.1055/s-0033-1350128.

McDonough, J. E., Yuan, R., Suzuki, M., Seyednejad, N., Elliott, W. M., Sanchez, P. G., Wright, A. C., Gefter, W. B., Litzky, L., Coxson, H. O., Paré, P. D., Sin, D. D., Pierce, R. A., Woods, J. C., McWilliams, A. M., Mayo, J. R., Lam, S. C., Cooper, J. D. and Hogg, J. C. (2011). **Small-Airway Obstruction and Emphysema in Chronic Obstructive Pulmonary Disease**. New Engl J Medicine *365*, 1567–1575, doi:10.1056/nejmoa1106955.

McHugh, M. L. (2012). **Interrater reliability: the kappa statistic**. Biochem Medica *22*, 276–282, doi:10.11613/bm.2012.031.

Meier, P. and Zierler, K. L. (1954). **On the Theory of the Indicator-Dilution Method for Measurement of Blood Flow and Volume**. J Appl Physiol *6*, 731–744, doi:10.1152/jappl.1954.6.12.731.

Mets, O. M., Roothaan, S. M., Bronsveld, I., Luijk, B., Graaf, E. A. van de, Vink, A. and Jong, P. A. de (2015). **Emphysema Is Common in Lungs of Cystic Fibrosis Lung Transplantation Patients: A Histopathological and Computed Tomography Study**. Plos One *10*, e0128062, doi:10.1371/journal.pone.0128062.

Meyer, F. (1994). **Topographic distance and watershed lines**. Signal Process *38*, 113–125, doi:10.1016/0165-1684(94)90060-4.

Neeb, D., Kunz, R. P., Ley, S., Szábo, G., Strauss, L. G., Kauczor, H., Kreitner, K. and Schreiber, L. M. (2009). **Quantification of pulmonary blood flow (PBF): Validation of perfusion MRI and nonlinear contrast agent (CA) dose correction with H 215O positron emission tomography (PET)**. Magnet Reson Med *62*, 476–487, doi:10.1002/mrm.22025.

Ohno, Y., Hatabu, H., Murase, K., Higashino, T., Kawamitsu, H., Watanabe, H., Takenaka, D., Fujii, M. and Sugimura, K. (2004). **Quantitative assessment of regional pulmonary perfusion in the entire lung using three-dimensional ultrafast dynamic contrast-enhanced magnetic resonance imaging: Preliminary experience in 40 subjects**. J Magn Reson Imaging *20*, 353–365, doi:10.1002/jmri.20137.

Ohno, Y., Murase, K., Higashino, T., Nogami, M., Koyama, H., Takenaka, D., Kawamitu, H., Matsumoto, S., Hatabu, H. and Sugimura, K. (2007). **Assessment of bolus injection protocol with appropriate concentration for quantitative assessment of pulmonary perfusion by dynamic contrast-enhanced MR imaging**. Journal of magnetic resonance imaging : JMRI *25*, 55–65, doi:10.1002/jmri.20790.

Østergaard, L. (2005). **Principles of cerebral perfusion imaging by bolus tracking**. J Magn Reson Imaging *22*, 710–717, doi:10.1002/jmri.20460.

Østergaard, L., Sorensen, A. G., Kwong, K. K., Weisskoff, R. M., Gyldensted, C. and Rosen, B. R. (1996). **High resolution measurement of cerebral blood flow using intravascular tracer bolus passages. Part II: Experimental comparison and preliminary results**. Magnet Reson Med *36*, 726–736, doi:10.1002/mrm.1910360511.

Ostergaard, L., Weisskoff, R. M., Chesler, D. A., Gyldensted, C. and Rosen, B. R. (1996). **High resolution measurement of cerebral blood flow using intravascular tracer bolus passages. Part I: Mathematical approach and statistical analysis**. Magnetic resonance in medicine *36*, 715–725, doi:10.1002/mrm.1910360510.

O'Sullivan, B. P. and Freedman, S. D. (2009). **Cystic fibrosis**. Lancet *373*, 1891–1904, doi:10.1016/s0140-6736(09)60327-5.

Otsu, N. (1979). **A Threshold Method from Gray-Level Histograms**. Ieee Transactions Syst Man Cybern , vol 9, no 1 *9*, 62–66, doi:10.1109/tsmc.1979.4310076.

Pearson, K. and Filon, L. N. G. (1898). **Mathematical contributions to the theory of evolution. IV. On the probable errors of frequency constants and on the influence of random selection on variation and correlation**. P R Soc London *62*, 173–176, doi:10.1098/rspl.1897.0091.

Peinado, V. I., Ramírez, J., Roca, J., Rodriguez-Roisin, R. and Barberà, J. A. (2006). **Identification of Vascular Progenitor Cells in Pulmonary Arteries of Patients with Chronic Obstructive Pulmonary Disease**. Am J Resp Cell Mol *34*, 257–263, doi:10.1165/rcmb.2005-0255oc.

Pianykh, O. S. (2012). **Perfusion linearity and its applications in perfusion algorithm analysis**. Comput Med Imag Grap *36*, 204–214, doi:10.1016/j.compmedimag.2011.08.001.

Pintaske, J., Martirosian, P., Graf, H., Erb, G., Lodemann, K.-P., Claussen, C. D. and Schick, F. (2006). **Relaxivity of Gadopentetate Dimeglumine (Magnevist), Gadobutrol (Gadovist), and Gadobenate Dimeglumine (MultiHance) in Human Blood Plasma at 0.2, 1.5, and 3 Tesla**. Invest Radiol *41*, 213–221, doi:10.1097/01.rli.0000197668.44926.f7.

Puderbach, Michael, Eichinger, M., Haeselbarth, J., Ley, S., Kopp-Schneider, A., Tuengerthal, S., Schmaehl, A., Fink, C., Plathow, C., Wiebel, M., Demirakca, S., Müller, F.-M. and Kauczor, H.-U. (2007). **Assessment of Morphological MRI for Pulmonary Changes in Cystic Fibrosis (CF) Patients**. Invest Radiol *42*, 715–724, doi:10.1097/rli.0b013e318074fd81.

Puderbach, M., Hintze, C., Ley, S., Eichinger, M., Kauczor, H.-U. and Biederer, J. (2007). **MR imaging of the chest: A practical approach at 1.5T**. Eur J Radiol *64*, 345–355, doi:10.1016/j.ejrad.2007.08.009.

Puderbach, M., Risse, F., Biederer, J., Ley-Zaporozhan, J., Ley, S., Szabo, G., Semmler, W. and Kauczor, H.-U. (2008). **In vivo Gd-DTPA concentration for MR lung perfusion measurements: Assessment with computed tomography in a porcine model**. Eur Radiol *18*, 2102–2107, doi:10.1007/s00330-008-0974-1.

Ravesh, M. S., Brix, G., Laun, F. B., Kuder, T. A., Puderbach, M., Ley-Zaporozhan, J., Ley, S., Fieselmann, A., Herrmann, M. F., Schranz, W., Semmler, W. and Risse, F. (2013). **Quantification of pulmonary microcirculation by dynamic contrast-enhanced magnetic resonance imaging: comparison of four regularization methods**. Magnetic resonance in medicine *69*, 188–199, doi:10.1002/mrm.24220.

Rayment, J. H., Couch, M. J., McDonald, N., Kanhere, N., Manson, D., Santyr, G. and Ratjen, F. (2019). **Hyperpolarised 129Xe magnetic resonance imaging to monitor treatment response in children with cystic fibrosis**. Eur Respir J *53*, 1802188, doi:10.1183/13993003.02188-2018.

Register Multimodal MRI Images - MATLAB & Simulink Example - MathWorks Deutschland (n.d.)., URL: https://de.mathworks.com/help/images/registering-multimodal-mri-images.html [Accessed February 2022].

Reiser, M. and Semmler, W. (1992). **Magnetresonanztomographie**. Springer, Berlin, Heidelberg 3–96, doi:10.1007/978-3-642-97167-9_2.

Riordan, J., Rommens, J., Kerem, B., Alon, N., Rozmahel, R., Grzelczak, Z., Zielenski, J., Lok, S., Plavsic, N., Chou, J. and al., et (1989). **Identification of the cystic fibrosis gene: cloning and characterization of complementary DNA**. Science *245*, 1066–1073, doi:10.1126/science.2475911.

Risse, F., Eichinger, M., Kauczor, H.-U., Semmler, W. and Puderbach, M. (2011). **Improved visualization of delayed perfusion in lung MRI**. Eur J Radiol *77*, 105–110, doi:10.1016/j.ejrad.2009.07.025.

Risse, F., Kuder, T. A., Kauczor, H.-U., Semmler, W. and Fink, C. (2009). **Suppression of pulmonary vasculature in lung perfusion MRI using correlation analysis**. Eur Radiol *19*, 2569, doi:10.1007/s00330-009-1464-9.

Risse, F., Semmler, W., Kauczor, H. and Fink, C. (2006). **Dual-bolus approach to quantitative measurement of pulmonary perfusion by contrast-enhanced MRI**. J Magn Reson Imaging *24*, 1284–1290, doi:10.1002/jmri.20747.

Rosenfeld, M., Ratjen, F., Brumback, L., Daniel, S., Rowbotham, R., McNamara, S., Johnson, R., Kronmal, R., Davis, S. D. and Group, for the I. S. (2012). **Inhaled Hypertonic Saline in Infants and Children Younger Than 6 Years With Cystic Fibrosis: The ISIS Randomized Controlled Trial**. Jama *307*, 2269–2277, doi:10.1001/jama.2012.5214.

Schiwek, M., Triphan, S. M. F., Biederer, J., Weinheimer, O., Eichinger, M., Vogelmeier, C. F., Jörres, R. A., Kauczor, H.-U., Heußel, C. P., Konietzke, P., Stackelberg, O. von, Risse, F., Jobst, B. J. and Wielpütz, M. O. (2021). **Quantification of pulmonary perfusion abnormalities using DCE-MRI in COPD: comparison with quantitative CT and pulmonary function**. Eur Radiol 1–12, doi:10.1007/s00330-021-08229-6.

Schreiber, W. G., Eberle, B., Laukemper-Ostendorf, S., Markstaller, K., Weiler, N., Scholz, A., Bürger, K., Heussel, C. P., Thelen, M. and Kauczor, H. (2001). **Dynamic 19F-MRI of pulmonary ventilation using sulfur hexafluoride (SF6) gas**. Magnet Reson Med *45*, 605–613, doi:10.1002/mrm.1082.

Sileo, C., Corvol, H., Boelle, P.-Y., Blondiaux, E., Clement, A. and Pointe, H. D. L. (2014). **HRCT and MRI of the lung in children with cystic fibrosis: Comparison of different scoring systems**. J Cyst Fibros *13*, 198–204, doi:10.1016/j.jcf.2013.09.003.

Singh, D., Agusti, A., Anzueto, A., Barnes, P. J., Bourbeau, J., Celli, B. R., Criner, G. J., Frith, P., Halpin, D. M. G., Han, M., Varela, M. V. L., Martinez, F., Oca, M. M. de, Papi, A., Pavord, I. D., Roche, N., Sin, D. D., Stockley, R., Vestbo, J., Wedzicha, J. A. and Vogelmeier, C. (2019). **Global Strategy for the Diagnosis, Management, and Prevention of Chronic Obstructive Lung Disease: the GOLD science committee report 2019**. Eur Respir J *53*, 1900164, doi:10.1183/13993003.00164-2019.

Soille, P. (1999). **Morphological Image Analysis, Principles and Applications**. Berlin: Springer 155–183, doi:10.1007/978-3-662-03939-7_6.

Sourbron, S., Dujardin, M., Makkat, S. and Luypaert, R. (2006). **Pixel-by-pixel deconvolution of bolus-tracking data: optimization and implementation**. Phys Med Biol *52*, 429–447, doi:10.1088/0031-9155/52/2/009.

Sourbron, S., Luypaert, R., Schuerbeek, P. V., Dujardin, M., Stadnik, T. and Osteaux, M. (2004). **Deconvolution of dynamic contrast-enhanced MRI data by linear inversion: Choice of the regularization parameter**. Magnet Reson Med *52*, 209–213, doi:10.1002/mrm.20113.

Sourbron, S. P. and Buckley, D. L. (2011). **Tracer kinetic modelling in MRI: estimating perfusion and capillary permeability**. Phys Med Biol *57*, R1–R33, doi:10.1088/0031-9155/57/2/r1.

Stahl, M., Joachim, C., Blessing, K., Hämmerling, S., Sommerburg, O., Latzin, P. and Mall, M. A. (2014). **Multiple Breath Washout Is Feasible in the Clinical Setting and Detects Abnormal Lung Function in Infants and Young Children with Cystic Fibrosis**. Respiration *87*, 357–363, doi:10.1159/000357075.

Stahl, M., Wielpütz, M. O., Graeber, S. Y., Joachim, C., Sommerburg, O., Kauczor, H.-U., Puderbach, M., Eichinger, M. and Mall, M. A. (2017). **Comparison of Lung Clearance Index and Magnetic Resonance Imaging for Assessment of Lung Disease in Children with Cystic Fibrosis**. Am J Resp Crit Care *195*, 349–359, doi:10.1164/rccm.201604-0893oc.

Starmer, C. F. and Clark, D. O. (1970). **Computer computations of cardiac output using the gamma function.** J Appl Physiol *28*, 219–220, doi:10.1152/jappl.1970.28.2.219.

Subramanian, D. R., Gupta, S., Burggraf, D., Silberberg, S. J. vom, Heimbeck, I., Heiss-Neumann, M. S., Haeussinger, K., Newby, C., Hargadon, B., Raj, V., Singh, D., Kolsum, U., Hofer, T. P., Al-shair, K., Luetzen, N., Prasse, A., Müller-Quernheim, J., Benea, G., Leprotti, S., Boschetto, P., Gorecka, D., Nowinski, A., Oniszh, K., Castell, W. zu, Hagen, M., Barta, I., Döme, B., Strausz, J., Greulich, T., Vogelmeier, C., Koczulla, A. R., Gut, I., Hohlfeld, J., Welte, T., Lavae-Mokhtari, M., Ziegler-Heitbrock, L., Brightling, C. and Parr, D. G. (2016). **Emphysema- and airway-dominant COPD phenotypes defined by standardised quantitative computed tomography**. Eur Respir J *48*, 92–103, doi:10.1183/13993003.01878-2015.

Ter-Karapetyan, A., Triphan, S. M. F., Jobst, B. J., Anjorin, A. F., Ley-Zaporozhan, J., Ley, S., Sedlaczek, O., Biederer, J., Kauczor, H. U., Jakob, P. M. and Wielputz, M. O. (2018). **Towards quantitative perfusion MRI of the lung in COPD: The problem of short-term repeatability**. PloS one *13*, e0208587, doi:10.1371/journal.pone.0208587.

Thirion, J.-P. (1998). **Image matching as a diffusion process: an analogy with Maxwell's demons**. Med Image Anal *2*, 243–260, doi:10.1016/s1361-8415(98)80022-4.

Thomas, M., Decramer, M. and O'Donnell, D. E. (2013). **No room to breathe: the importance of lung hyperinflation in COPD**. Prim Care Resp J *22*, 101–111, doi:10.4104/pcrj.2013.00025.

Thompson, H. K., Starmer, C. F., WHALEN, R. E. and MCINTOSH, H. D. (1964). **Indicator Transit Time Considered as a Gamma Variate**. Circ Res *14*, 502–515, doi:10.1161/01.res.14.6.502.

Tiddens, H. A. W. M., Donaldson, S. H., Rosenfeld, M. and Paré, P. D. (2010). **Cystic fibrosis lung disease starts in the small airways: Can we treat it more effectively?** Pediatr Pulm *45*, 107–117, doi:10.1002/ppul.21154.

Triphan, S. M. F., Biederer, J., Burmester, K., Fellhauer, I., Vogelmeier, C. F., Jörres, R. A., Kauczor, H.-U., Heußel, C. P., Wielpütz, M. O. and Jobst, B. J. (2018). **Design and application of an MR reference phantom for multicentre lung imaging trials**. Plos One *13*, e0199148, doi:10.1371/journal.pone.0199148.

Vaals, J. J. V., Brummer, M. E., Dixon, W. T., Tuithof, H. H., Engels, H., Nelson, R. C., Gerety, B. M., Chezmar, J. L. and Boer, J. A. D. (1993). **"Keyhole" method for accelerating imaging of contrast agent uptake**. J Magn Reson Imaging *3*, 671–675, doi:10.1002/jmri.1880030419.

Vercauteren, T., Pennec, X., Perchant, A. and Ayache, N. (2009). **Diffeomorphic demons: Efficient non-parametric image registration**. Neuroimage *45*, S61–S72, doi:10.1016/j.neuroimage.2008.10.040.

Vlaardingerbroek, M. T. and Boer, J. A. den (2013). **Magnetic Resonance Imaging: Theory and Practice**. Springer Science & Business Media 235–276, doi:10.1007/978-3-662-03258-9_6.

Voelkel, N. F., Gomez-Arroyo, J. and Mizuno, S. (2011). **COPD/Emphysema: The Vascular Story**. Pulm Circ *1*, 320–326, doi:10.4103/2045-8932.87295.

Vogel-Claussen, J., Schönfeld, C.-O., Kaireit, T. F., Voskrebenzev, A., Czerner, C. P., Renne, J., Tillmann, H.-C., Berschneider, K., Hiltl, S., Bauersachs, J., Welte, T. and Hohlfeld, J. M. (2019). **Effect of Indacaterol/Glycopyrronium on Pulmonary Perfusion and Ventilation in Hyperinflated Patients with Chronic Obstructive Pulmonary Disease (CLAIM). A Double-Blind, Randomized, Crossover Trial**. Am J Resp Crit Care *199*, 1086–1096, doi:10.1164/rccm.201805-0995oc.

Vogelmeier, C. F., Criner, G. J., Martinez, F. J., Anzueto, A., Barnes, P. J., Bourbeau, J., Celli, B. R., Chen, R., Decramer, M., Fabbri, L. M., Frith, P., Halpin, D. M. G., Varela, M. V. L., Nishimura, M., Roche, N., Rodriguez-Roisin, R., Sin, D. D., Singh, D., Stockley, R., Vestbo, J., Wedzicha, J. A. and Agusti, A. (2017). **Global Strategy for the Diagnosis, Management, and Prevention of Chronic Obstructive Lung Disease 2017 Report: GOLD Executive Summary**. Eur Respir J *49*, 1700214, doi:10.1183/13993003.00214-2017.

Wang, H., Dong, L., O'Daniel, J., Mohan, R., Garden, A. S., Ang, K. K., Kuban, D. A., Bonnen, M., Chang, J. Y. and Cheung, R. (2005). **Validation of an accelerated "demons" algorithm for deformable image registration in radiation therapy**. Phys Med Biol *50*, 2887–2905, doi:10.1088/0031-9155/50/12/011.

Webb, W. R. (2006). **Thin-Section CT of the Secondary Pulmonary Lobule: Anatomy and the Image—The 2004 Fleischner Lecture1**. Radiology *239*, 322–338, doi:10.1148/radiol.2392041968.

Weibel, E. R. and Gomez, D. M. (1962). **Architecture of the Human Lung**. Science *137*, 577–585, doi:10.1126/science.137.3530.577.

Wielpütz, M. and Kauczor, H. U. (2012). **MRI of the lung: state of the art**. Diagn Interv Radiol *18*, 344–353, doi:10.4261/1305-3825.dir.5365-11.0.

Wielpütz, M. O., Eichinger, M., Wege, S., Eberhardt, R., Mall, M. A., Kauczor, H.-U., Puderbach, M. U., Risse, F., Heußel, C. P. and Heußel, G. (2019). **Midterm Reproducibility of Chest Magnetic Resonance Imaging in Adults with Clinically Stable Cystic Fibrosis and Chronic Obstructive Pulmonary Disease**. Am J Resp Crit Care *200*, 103–107, doi:10.1164/rccm.201812-2356le.

Wielpütz, M. O., Puderbach, M., Kopp-Schneider, A., Stahl, M., Fritzsching, E., Sommerburg, O., Ley, S., Sumkauskaite, M., Biederer, J., Kauczor, H. U., Eichinger, M. and Mall, M. A. (2014). **Magnetic resonance imaging detects changes in structure and perfusion, and response to therapy in early cystic fibrosis lung disease**. Am J Respir Crit Care Med *189*, 956–965, doi:10.1164/rccm.201309-1659oc.

Wielpütz, M. O., Stackelberg, O. von, Stahl, M., Jobst, B. J., Eichinger, M., Puderbach, M. U., Nährlich, L., Barth, S., Schneider, C., Kopp, M. V., Ricklefs, I., Buchholz, M., Tümmler, B., Dopfer, C., Vogel-Claussen, J., Kauczor, H.-U. and Mall, M. A. (2018). **Multicentre standardisation of chest MRI as radiation-free outcome measure of lung disease in young children with cystic fibrosis**. J Cyst Fibros *17*, 518–527, doi:10.1016/j.jcf.2018.05.003.

Wielpütz, M. O., Weinheimer, O., Eichinger, M., Wiebel, M., Biederer, J., Kauczor, H.-U., Heußel, C. P., Mall, M. A. and Puderbach, M. (2013). **Pulmonary Emphysema in Cystic Fibrosis Detected**

by Densitometry on Chest Multidetector Computed Tomography. Plos One *8*, e73142, doi:10.1371/journal.pone.0073142.

Wild, J. M., Marshall, H., Bock, M., Schad, L. R., Jakob, P. M., Puderbach, M., Molinari, F., Beek, E. J. R. V. and Biederer, J. (2012). **MRI of the lung (1/3): methods**. Insights Imaging *3*, 345–353, doi:10.1007/s13244-012-0176-x.

Woodhouse, N., Wild, J. M., Paley, M. N. J., Fichele, S., Said, Z., Swift, A. J. and Beek, E. J. R. van (2005). **Combined helium-3/proton magnetic resonance imaging measurement of ventilated lung volumes in smokers compared to never-smokers**. J Magn Reson Imaging *21*, 365–369, doi:10.1002/jmri.20290.

Wrobel, J. P., McLean, C. A., Thompson, B. R., Stuart-Andrews, C. R., Paul, E., Snell, G. I. and Williams, T. J. (2013). **Pulmonary Arterial Remodeling in Chronic Obstructive Pulmonary Disease is Lobe Dependent**. Pulm Circ *3*, 665–674, doi:10.1086/674339.

Xia, Y., Guan, Y., Fan, L., Liu, S. Y., Yu, H., Zhao, L. M. and Li, B. (2014). **Dynamic contrast enhanced magnetic resonance perfusion imaging in high-risk smokers and smoking-related COPD: correlations with pulmonary function tests and quantitative computed tomography**. Copd *11*, 510–520, doi:10.3109/15412555.2014.948990.

Zhou-Suckow, Z., Duerr, J., Hagner, M., Agrawal, R. and Mall, M. A. (2017). **Airway mucus, inflammation and remodeling: emerging links in the pathogenesis of chronic lung diseases**. Cell Tissue Res *367*, 537–550, doi:10.1007/s00441-016-2562-z.

Zierler, K. L. (1962). **Theoretical Basis of Indicator-Dilution Methods For Measuring Flow and Volume**. Circ Res *10*, 393–407, doi:10.1161/01.res.10.3.393.

8   OWN PUBLICATIONS / CONTRIBUTIONS

8.1   Published results of this work

Schiwek, M., Triphan, S. M. F., Biederer, J., Weinheimer, O., Eichinger, M., Vogelmeier, C. F., Jörres, R. A., Kauczor, H.-U., Heußel, C. P., Konietzke, P., Stackelberg, O. von, Risse, F., Jobst, B. J., and Wielpütz, M. O. (2021). **Quantification of pulmonary perfusion abnormalities using DCE-MRI in COPD: comparison with quantitative CT and pulmonary function.** Eur Radiol 1–12, doi:10.1007/s00330-021-08229-6.

This publication contains the results of section 3.2 and their discussion in section 4 of this

doctoral thesis. Software development, image data analysis, statistical analysis and manuscript

preparation were primarily performed by the author of this thesis.

Konietzke, M., Triphan, S. M. F., Eichinger, M., Bossert, B., Heller, H., Wege, S., Eberhardt, R.., Puderbach, M.., Kauczor, H.-U., Heußel, G., Heußel, C. P., Risse, F., and Wielpütz, M. O. (2022). **Unsupervised clustering algorithms improve the reproducibility of DCE-MRI pulmonary perfusion quantification in muco-obstructive lung diseases.** Submitted for publication.

This publication contains the results of section 3.3 and their discussion in section 4 of this

doctoral thesis. Software development, image data analysis, statistical analysis and manuscript

preparation were primarily performed by the author of this thesis.

8.2 Other own peer-reviewed journal contributions

Deterding, R., Griese, M., Deutsch, G., Warburton, D., DeBoer, E. M., Cunningham, S., Clement, A., Schwerk, N., Flaherty, K. R., Brown, K. K., Voss, F., Schmid, U., Schlenker-Herceg, R., Verri, D., Dumistracel, M., **Schiwek, M.**, Stowasser, S., Tetzlaff, K., Clerisme-Beaty, E., and Young, L. R. (2021). **Study design of a randomised, placebo-controlled trial of nintedanib in children and adolescents with fibrosing interstitial lung disease.** Erj Open Res 7, 00805–02020, doi:10.1183/23120541.00805-2020.

8.3 First and co-authorship conference contributions

Schiwek, M., Risse, F., Triphan, S. M. F., Eichinger, M., Wege, S., Stahl, M., Sommerburg, O., Mall, M. A., Kauczor, H.-U., Puderbach, M., Eberhardt, R.., Heußel, C. P., Heußel, G., and Wielpütz, M. O. (2018). **The Impact of Inspiration Levels on the Repeatability of Quantitative Pulmonary Perfusion DCE-MRI in Patients with Chronic Obstructive Pulmonary Disease and Cystic Fibrosis.** Proc. Intl. Soc. Mag. Reson. Med. 26, 2458.

Renne, J., Biller, H., Gutberlet, M., Czerner, C., **Schiwek, M**., Hohl, K., Risse, F., Sarno, M., Gupta, A., Hohlfeld, J. and Vogel-Claussen, J. (2018). **Regional detection of edema following segmental LPS challenge using functional MR imaging.** Imaging OA3798, doi:10.1183/13993003.congress-2018.oa3798.

Schiwek, M., Triphan, S. M. F., Eichinger, M., Wege, S., Stahl, M., Sommerburg, O., Mall, M. A., Kauczor, H.-U., Puderbach, M., Eberhardt, R.., Heußel, C. P., Heußel, G., Risse, F., and Wielpütz, M. O. (2019**). Repeatability of Quantitative 4D Lung Perfusion MRI in Patients with Cystic Fibrosis and Chronic Obstructive Pulmonary Disease.** 8th DZL Annual Meeting.

Triphan, S. M. F., **Schiwek, M**., Eichinger, M., Wege, S., Stahl, M., Sommerburg, O., Mall, M. A., Kauczor, H.-U., Puderbach, M., Eberhardt, R.., Heußel, C. P., Heußel, G., Risse, F., and Wielpütz, M. O. (2019). **Comparison of Quantitative Lung Perfusion and T1 Mapping in Cystic Fibrosis and Chronic Obstructive Pulmonary Disease.** 8th DZL Annual Meeting.

Triphan, S. M. F., **Schiwek, M**., Eichinger, M., Wege, S., Stahl, M., Sommerburg, O., Mall, M. A., Kauczor, H.-U., Puderbach, M., Eberhardt, R.., Heußel, C. P., Heußel, G., Risse, F., and Wielpütz, M. O. (2019). **Short-term Repeatability of Lung T1 Mapping at Ultrashort TE in Chronic Obstructive Pulmonary Disease and Cystic Fibrosis.** 8th DZL Annual Meeting.

Schiwek, M., Triphan, S. M. F., Eichinger, M., Stahl, M., Kauczor, H.-U., Heußel, G., Heußel, C. P., Risse, F., and Wielpütz, M. O. (2020). **Automatic detection of lung perfusion defects on contrast-enhanced 4D MRI in cystic fibrosis (CF) and chronic obstructive pulmonary disease (COPD): repeatability and comparison with visual scoring.** ECR 2020. European Society of Radiology (ESR) EPOS poster #7013.

DANKSAGUNG

Zu guter Letzt möchte ich mich von ganzem Herzen bei meiner Familie bedanken. Zuerst bei meinen Eltern, **Birgitt und Clément Schiwek,** sowie meinem Bruder, **Maximilian Schiwek,** auf deren uneingeschränkte Unterstützung ich stehts zählen konnte. Außerdem bei meinem Ehemann, **Dr. Philip Konietzke**, den ich im Rahmen dieser Arbeit kennengelernt habe, dafür, dass er mich sogar am Wochenende für die Doktorarbeit motivieren konnte und für seine einfallsreichen Ideen und Korrekturen.

EIDESSTATTLICHE VERSICHERUNG

1. Bei der eingereichten Dissertation zu dem Thema „*Quantification of perfusion abnormalities using dynamic contrast-enhanced magnetic resonance imaging in muco-obstructive lung diseases*" handelt es sich um meine eigenständig erbrachte Leistung.

2. Ich habe nur die angegebenen Quellen und Hilfsmittel benutzt und mich keiner unzulässigen Hilfe Dritter bedient. Insbesondere habe ich wörtlich oder sinngemäß aus anderen Werken übernommene Inhalte als solche kenntlich gemacht.

3. Die Arbeit oder Teile davon habe ich bislang nicht an einer Hochschule des In- oder Auslands als Bestandteil einer Prüfungs- oder Qualifikationsleistung vorgelegt.

4. Die Richtigkeit der vorstehenden Erklärungen bestätige ich.

5. Die Bedeutung der eidesstattlichen Versicherung und die strafrechtlichen Folgen einer unrichtigen oder unvollständigen eidesstattlichen Versicherung sind mir bekannt. Ich versichere an Eides statt, dass ich nach bestem Wissen die reine Wahrheit erklärt und nichts verschwiegen habe.

Heidelberg, 2022

_____
Marilisa Konietzke